FILM COOLING JET LIFT–OFF UNDER A STREAMWISE PRESSURE GRADIENT AT DIFFERENT BLOWING RATIOS

Marc Gomez-Olive Fernandez

Supervised by Dr Michael Atkins, Prof Tongbeum Kim, and Dr Sjouke Schekman

Master of Science in Engineering by research only:

A dissertation submitted to the Faculty of Engineering and the Built Environment, University of the Witwatersrand, Johannesburg, in fulfilment of the requirements for the degree of Master of Science in Engineering.

Johannesburg, 2025

CANDIDATE'S DECLARATION

I declare that this dissertation is my own unaided work. It is being submitted to the Degree of Master of Science in Engineering to the University of the Witwatersrand, Johannesburg. It has not been submitted before for any degree or examination to any other University.

……………………………………………….
(Signature of Candidate)

30th day of March year 2025

ABSTRACT

This study introduces the concept of a *critical blowing ratio*, defining the point at which a film cooling jet detaches from an endwall under a streamwise pressure gradient. Four pressure gradients, extracted over a turbine blade were tested: favourable (FPG), mild favourable (MFPG), zero (ZPG), and mild adverse (MAPG) with acceleration parameters of $K = 2.61\times10^{-6}$, $K = 1.53\times10^{-6}$, $K = 0.00\times10^{-6}$, and $K = (-)0.31\times10^{-6}$. Engine representative conditions were employed with a Re_D~14000, hole diameter of 20.0 mm at an injection angle of 30°. The blowing ratio (M) ranged from 0.5 to 2.0 in increments of 0.1. Velocity measurements and visualisation techniques extracted using Particle Image Velocimetry (PIV), Planar Laser Visualisation (PLV), and end-wall oil-dye mixture techniques showed that the coolant jet, at a particular blowing ratio, was either *attached*, *semi-detached* or fully *detached* regardless of the pressure gradient imposed. The critical blowing ratio, in a FPG, was ~1.8 times greater than in a MAPG, indicating better attachment of the coolant jets in FPGs.

DEDICATION

In appreciation of my mom, dad, siblings, and my entire family and friends for their continual support in my life.

ACKNOWLEDGEMENTS

I would like to acknowledge the assistance of several individuals that have aided me in this project: the NWE technicians (Shaun, Vernondran, Andrew, Klaas, and Zwavho), for their aid in the construction of the experimental setup, fellow master’s students (Aliah, Abhay, Claude, Michael, Jordan, Kayla, and Uma) that have provided valuable information and aided me along the way, and to my supervisors that have helped me continuously.

TABLE OF CONTENTS

LIST OF FIGURES

LIST OF TABLES

NOMENCLATURE

T	Temperature (°C)
u_m	Velocity of mainstream flow (m/s)
v_c	Velocity of coolant jet (m/s)
T_f	Temperature of film jet over blade surface (°C)
V_t	Tangential velocity component (m/s)
ϵ	Vortex sheet thickness
FCE or η	Film cooling effectiveness
M	Blowing ratio
ρ	Density (kg/m^3)
Subscripts c and m	Subscripts denoting coolant flow (*c*) or mainstream flow (*m*)
FPG	Favourable pressure gradient
MFPG	Mild favourable pressure gradient
ZPG	Zero pressure gradient
MAPG	Mild adverse pressure gradient
h	Height of the test section exit based on the contoured endwall used for the varying pressure gradients (mm)
H	Height of test section inlet (mm)
L	Length of test section (mm)
D	Diameter of cylindrical hole (mm)
θ	Angle of hole relative to the test section endwall (deg)
Re_D	Reynolds number based on cylindrical hole diameter
K	Acceleration parameter
μ	Kinematic viscosity
ν	Dynamic viscosity
M_0	Magnification factor
u_r	Radial velocity (m/s)
P	Pressure (Pa)
Q	Flow rate (m^3/s)
A	Area (m^2)
C_d	Discharge coefficient
δ	Boundary layer height (mm)
z_1	Spacing between kidney vortex cores
z_3	Spacing at Wake Region 3 at x/D = 3
y_1	Height of kidney vortex cores above the endwall surface

1. Background

1.1. Introduction

Contemporary gas turbine engines are designed to operate at high turbine inlet temperatures (TITs) (~1700°C [1]) that typically exceed the melting point (~1200°C [1]) of turbine blade materials. As a result, turbine blades are exposed to temperatures above permissible material temperatures, which is detrimental to the lifespan of the blades. Increasing TITs, however, improves the work output of the gas turbines and hence their overall efficiency [2]. Therefore, to reduce blade temperatures within the allowable limits whilst operating at high TITs, cooler air (~700°C [1], [3]) is bled off from preceding compressors to the turbine blades. Firstly, the cooler air as coolant is bled to the internal cooling channels designed in the blade, thus, lowering the blade temperature. Secondly, a designed portion of the coolant is released through discrete holes to the external surfaces creating a thin layer (or "film") of the coolant around the blade. This technique is known as film cooling and aims to act as a barrier between the hot combustion gas stream and the blade surfaces to reduce heat transfer to the blade.

Film cooling holes are purposely distributed on gas turbine blade surfaces since the extent of heat transfer greatly varies with local positions on the blade surfaces e.g., azimuthally in a mid-span plane at the leading-edge due to stagnation, mid-chord over the suction surface due to transitioning flow and at the trailing edge due to turbulent flow [4], [5], [6]. The coolant ejection through these film cooling holes acts as a jet in crossflow. The cool air flows over the blade surface exposing the blade surface to cooler temperatures, thus, decreases the heat transfer to the blade [1].

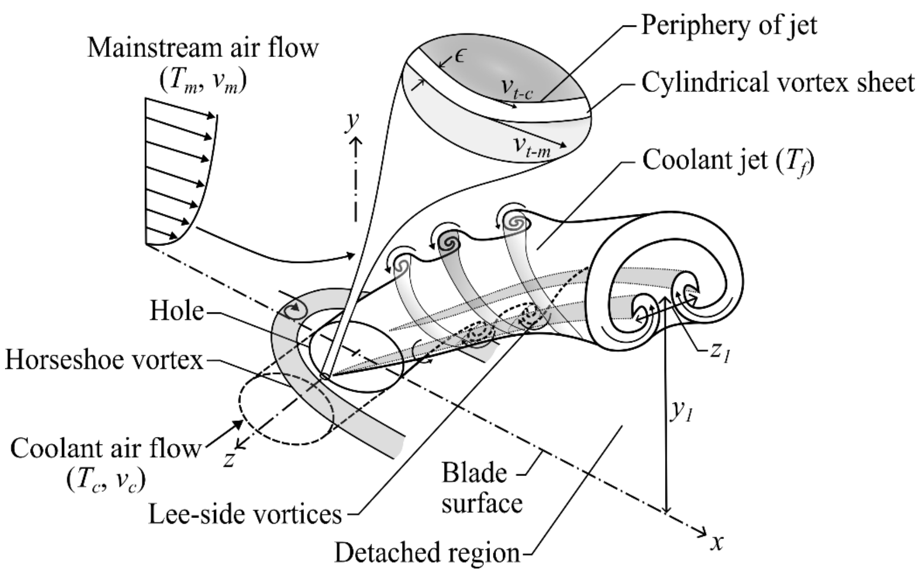

(a)

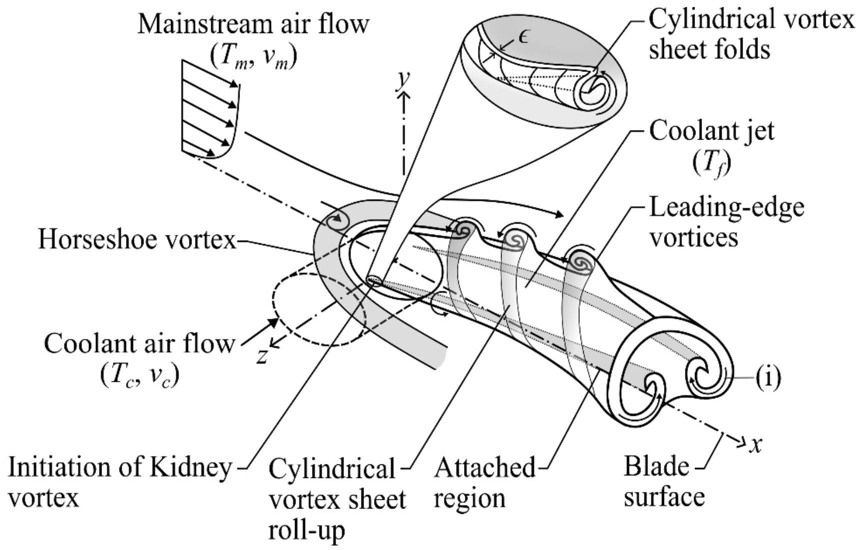

(b)

Figure 1.1: Film cooling jet in crossflow, adapted from [4], [7], [8], [9], [10], [11]. (a) Detached coolant jet from the blade surface and (b) Attached coolant jet from the blade surface

Figure 1.1 illustrates a typical complex three-dimensional development of a jet interaction with mainstream as crossflow. As a result of the interaction between the two streams, a distinct secondary flow structure around the juncture of the film cooling jet and endwall surface, the so-called "horseshoe vortex" forms. Another distinct flow structure that forms within the jet, is a "Kidney vortex," a pair of counter-rotating vortices that constitutes the jet core whose axis is bent and eventually becomes aligned parallel to the hot gas stream while convecting downstream[1], [4], [12].

The horseshoe vortex forms upstream of the leading edge of the jet (stagnation point) where the boundary layer of the mainstream flow encounters the jet as shown in Figure 1.1(a and b). The obstruction (that is the coolant jet) in the direction of the mainstream flow induces an adverse pressure gradient that results in reverse flow and separation of the boundary layer flow from the endwall [13]. This consequently induces a complex three-dimensional vortex system, known as a horseshoe vortex, that propagates around the jet periphery in the direction of the mainstream flow [7], [9].

The Kidney vortex is formed at the interface between the mainstream and coolant jet where a thin shear layer, with thickness ϵ, forms due to the rapid increase in the tangential velocity (that of the jet to the mainstream flow shown in Figure 1.1(a)) across the thickness of the shear layer, where $\epsilon \to 0$ [11]. This creates a high velocity gradient or discontinuity in the tangential velocity that induces vorticity within the shear layer resulting in the formation of a cylindrical vortex sheet as illustrated in Figure 1.1(a) [8], [9], [11]. The flow within this cylindrical vortex sheet is unstable according to the Kelvin-Helmholtz shear instability theory [11]. With temporal evolution, this instability in the shear layer amplifies due to the vorticity present in the fluid resulting in the swirling or roll-up of the cylindrical vortex sheet into loops shown in Figure 1.1(b) [8], [14]. Three distinct folding processes result from this phenomenon, namely: (i) leading-edge, (ii) lee-side and (iii) Kidney vortices. Leading-edge and lee-side vortices occur due to the free roll-up of the cylindrical vortex sheet (Figure 1.1(a and b)) [8]. On the circumference at $y \sim 0$, where the periphery of the jet interacts with the mainstream flow, the cylindrical vortex sheet folds up on its edges in the direction of the mainstream flow to initiate the formation of a counter-rotating vortex pair, denoted as "(i)" in Figure 1.1(b) [8]. The presence of the counter-rotating vortices in the jet induces an inward rotation within the jet core that drives the outer boundary jet flow towards the centre, resulting in a net upwards force on the jet [10]. The consequent detachment of the jet is shown in Figure 1.1(a) by "y_1", creating a region of low-velocity flow downstream of the film cooling hole, which is coupled with the circulation of the vortices and causes entrainment of the mainstream flow towards the centre of the jet [7], [15].

These Kidney vortices are established as the dominant vortices that reduce the film cooling effectiveness (FCE) [7], [12], [16], [17] ($\eta = T_m\text{-}T_f / T_m\text{-}T_c$) [3]. This parameter (FCE) measures how well the driving temperature of the coolant core, known as the film temperature (T_f), retains the initial coolant temperature (T_c) along the blade surfaces. A decrease in the film cooling effectiveness occurs as the counter-rotation of the Kidney vortices entrain hot mainstream air (T_m) resulting in the dilution of the film temperature with the hot gas stream, thereby detrimentally increasing blade surface temperatures [7], [18]. Further, the counter-rotation notably induces lift-off (detachment) of the coolant jet from the blade surface (Figure 1.1(a)), which increases the temperature near the blade surface and adversely influences the film cooling effectiveness [7], [18], [19]. On the other hand, attached coolant jets (Figure 1.1(b)) expose the blade surface to lower temperatures which reduces the heat transfer to the blade, thereby improving film cooling effectiveness [1].

The Kidney vortices are characterized by (i) the strength (rotation of vortices causing entrainment of mainstream air), (ii) lateral separation (a core-to-core distance between two counter-rotating vortices, z_1 [20]), and (iii) lift-off (detachment from the blade surface, y_1). These characteristics are affected by numerous factors such as a streamwise pressure gradient, blowing ratios, and hole geometries including hole angle, shape, and size. Among these, the streamwise pressure gradient is known as a primary cause affecting the film cooling effectiveness due to varying boundary layer flow over a turbine blade at the film cooling ejection points.

Various pressure gradient scenarios co-exist over a turbine blade: (i) a favourable pressure gradient (PG) (near the leading edge as the flow is accelerating and the pressure decreases away from the stagnation point), (ii) a zero PG (by the mid-chord as the flow transitions from a laminar accelerating flow to a turbulent decelerating flow as the pressure increases towards the trailing edge), and (iii) an adverse PG (near the trailing edge as the flow decelerates rapidly due to the increase in pressure) as illustrated in Figure 1.2 [4], [5], [6], [21].

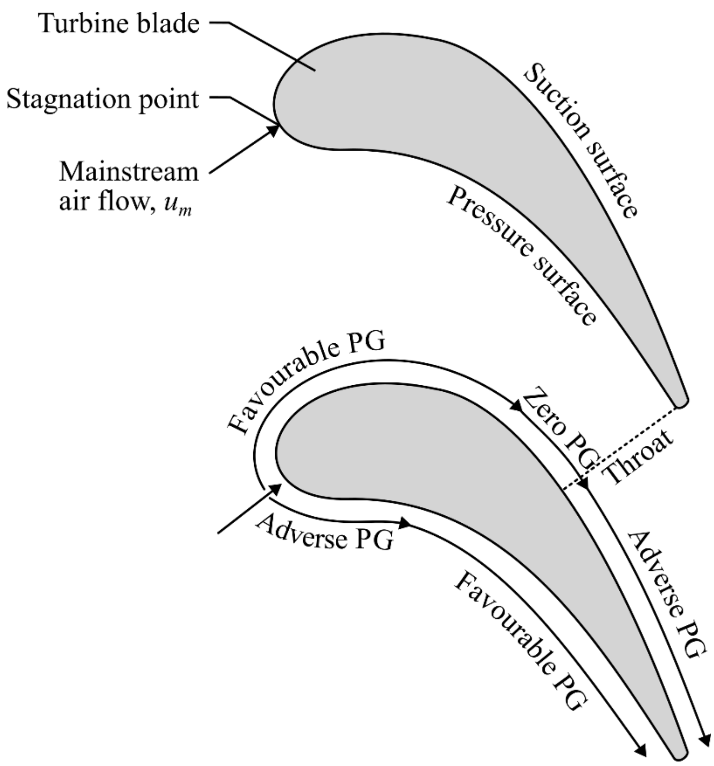

Figure 1.2: Pressure gradients (PGs) existing along the blade passage of a gas turbine [4], [5], [6], [21]

In favourable pressure gradients, the boundary layer thins upstream of the ejection point due to the increased convective acceleration of boundary layer flow [4], [21]. The increased streamwise velocity of the boundary layer flow creates a higher-pressure region on the ejected coolant jet column due to stagnation. The difference in pressure upstream and downstream of the ejection point generates a net downward force (towards the blade surfaces) on the coolant jet column. Therefore, the jet core moves closer to the blade surface with y_1 being decreased (Figure 1.1(b)), and thus the cooling effectiveness increases [4], [22]. On the other hand, in an adverse pressure gradient, the jet core trajectory moves farther away from the blade surfaces (i.e., lift-off) due to the relative decrease in the acceleration of the boundary layer flow and the thickening of the boundary layer. As a result, the film cooling effectiveness decreases near and downstream of the ejection point [16].

The detachment of the coolant jet from the blade surface has not been explicitly analysed in previous studies. Rather, the film cooling effectiveness is compared at various blowing ratios for a given pressure gradient condition. The blowing ratio (M) that is the mass flux of coolant relative to that of the mainstream, commonly varies between M = 0.5 to 2.0 for differing blade designs and applications. Here, the blowing ratio is defined as $M = \rho_c v_c / \rho_m v_m$ where ρ is the density and v is the velocity with the subscripts c and m referring to the coolant and mainstream flow, respectively [23]. Although the film cooling effectiveness values provide insight into the flow interaction, the film cooling effectiveness data is limited to a symmetry plane with respect to the film cooling jet and not rather the complex three-dimensional nature of such a jet in crossflow. Schmidt et al. [24] recorded the adiabatic wall temperature across a flat surface in a zero-pressure gradient (constant area test section) channel and favourable pressure gradient channel flow. They noted that the FCE decreased in the zero-pressure gradient channel when the blowing ratio was greater than $M = 1.0$. However, above $M = 1.5$ the FCE was the same for the zero and favourable pressure gradients. Extracted from this finding was that the coolant jet detached from the lower surface at higher blowing ratios. However, no insight into the flow interaction causing the observed detachment was provided. Jessen et al. [16] used particle image velocimetry (PIV), to test the jet lift-off of staggered film cooling holes under zero and adverse pressure gradients implemented by contouring an upper test section wall. Their work showed that the coolant jet penetrated deeper into the boundary layer in adverse pressure gradients compared to zero pressure gradients, thus, reducing the FCE as the coolant jet did not influence the endwall FCE data collected. However, the focus of the study was to observe the effects of both density and rows of holes on the FCE and not particularly (although stated) on the effect of the pressure gradient on the detachment of the jet from the lower endwall surface.

A study by Qin et al. [17] used pressure sensitive paint (PSP) on a flat and curved surface to compare the effects of curvature and streamwise pressure gradient on the FCE. This study, however, counter-intuitively determined that in an adverse pressure gradient, the FCE increased at low blowing ratios ($M < 0.75$), compared to when ejecting into a favourable pressure gradient. Qin et al. [17] additionally found that further increasing the blowing ratio to $M > 0.75$ in an adverse pressure gradient showed a decrease in the FCE. Particularly near the ejection point up to $x/D < 3.0$ where x is the streamwise distance downstream of the ejection point measured from the centre of the ejection hole and D is the diameter of the hole. Hay et al. [25] tested the heat transfer coefficient over a flat plate under favourable, zero and adverse pressure gradients created using a contoured upper wall at various blowing ratios. Similarly to Schmidt et al.(Schmidt and Bogard 1995), the results obtained by Hay [25] also found that the effect of high blowing ratios dominated the effect of the imposed pressure gradient on the flow. However, the detachment of the coolant jet was not mentioned or analysed as a factor effecting the FCE. Teekeram et al.[26] tested the heat transfer coefficient in a similar setup to Hay et al. [25] but with a slot hole configuration. This study found that decreasing the pressure gradient (i.e., stronger favourable) resulted in a large decrease in the heat transfer coefficient than mild favourable, zero and mild adverse pressure gradients at the same blowing ratios. Teekeram et al. [26] attributed this increased cooling to the attachment of the coolant jet but without visual data to reaffirm their conclusion.

To clarify the apparent contradictions relating to the effect of a streamwise pressure gradient and blowing ratio on the attachment and detachment of the coolant jet, the effect of each parameter must be considered separately. Both detachment and attachment of the film cooling jet is simultaneously a function of the streamwise pressure gradient and blowing ratios. Firstly, under a constant pressure gradient, increasing the blowing ratio has been noted to result in an increase in the detachment of the jet. Secondly, under a constant blowing ratio, an imposed favourable pressure gradient will more likely cause the coolant jet to remain attached compared to an adverse or zero pressure gradient. To group the point of coolant jet detachment from the endwall under the effect of both the pressure gradient and blowing ratio, this study investigated the "critical blowing ratio". The critical blowing ratio is classified as the blowing ratio at which the coolant jet detaches from the endwall surface under the influence of a given streamwise pressure gradient. The aforementioned studies [16], [17], [24], [25], [26], albeit with the common focus on the film cooling effectiveness, indicate that detachment of the coolant jet exists under a streamwise pressure gradient and varying blowing ratio. However, the experimental methods used in literature limited the acquisition of experimental data that would enable the capture of both the "critical blowing ratio" and the interaction between the film cooling jet and mainstream flow under the influence of a given streamwise pressure gradient. A series of experimental measurements were carried out to visualise and quantify the specific issue that is the relationship between pressure gradient and blowing ratio for the attachment and detachment of film cooling jet. The imposed pressure gradients (favourable, mild favourable, zero, and mild adverse) were accomplished by endwall contouring, i.e. the adjustment of one of the endwalls in the channel. Pneumatic pressure measurements were used to quantify the pressure across the channel depending on the endwall contouring to achieve the required pressure gradient. The inlet mainstream flow prior to the endwall contouring was constant to maintain a Re_D of 14 000. The blowing ratio varied in increments of 0.1 from M = 0.5 to 2.0 by adjusting the coolant flow rate. Planar laser visualisation was used to visualise the coolant jet structure, plume height and detachment lengths. Particle image velocimetry was used to map the velocity vector field to quantify the velocity of the jet and mainstream flow and to capture the structure of the kidney vortices.

1.2. Literature Review

1.2.1. Workings of gas turbine engines

Gas turbine engines are used in several fields (such as aviation, nautical science, and in power stations) to generate electrical energy or thrust. Figure 1.3 shows a cut-out sideview schematic of a gas turbine engine used in aviation, in this case, a turbofan jet engine. Gas turbine engines consist of a common layout comprised of three sections: a compressor, a combustion chamber, and a turbine. Air intake flows through the compressor (axial or centrifugal) where ambient air is compressed, thus increasing the ambient pressure at an approximate ratio of ~1.25:1 and ~8:1 per stage for an axial and centrifugal respectively (depending on the application) [4]. The compressed air is subsequently drawn into the combustion chamber where the air mixes with fuel and is ignited to create combustion. Hot air (~1700°C [1], [4]) at high velocities (~700m/s [1], [4]) is ejected from the combustion chamber directed to the turbine. The turbine, of interest in this study, is made up of several stages consisting of series of stator and rotor blades as shown in Figure 1.3(b). Stator blades are attached along the circumference of a static ring. Their purpose is to guide the flow to the rotor blades which converts the kinetic energy of the air into mechanical energy through rotation of a shaft that powers the compressor.

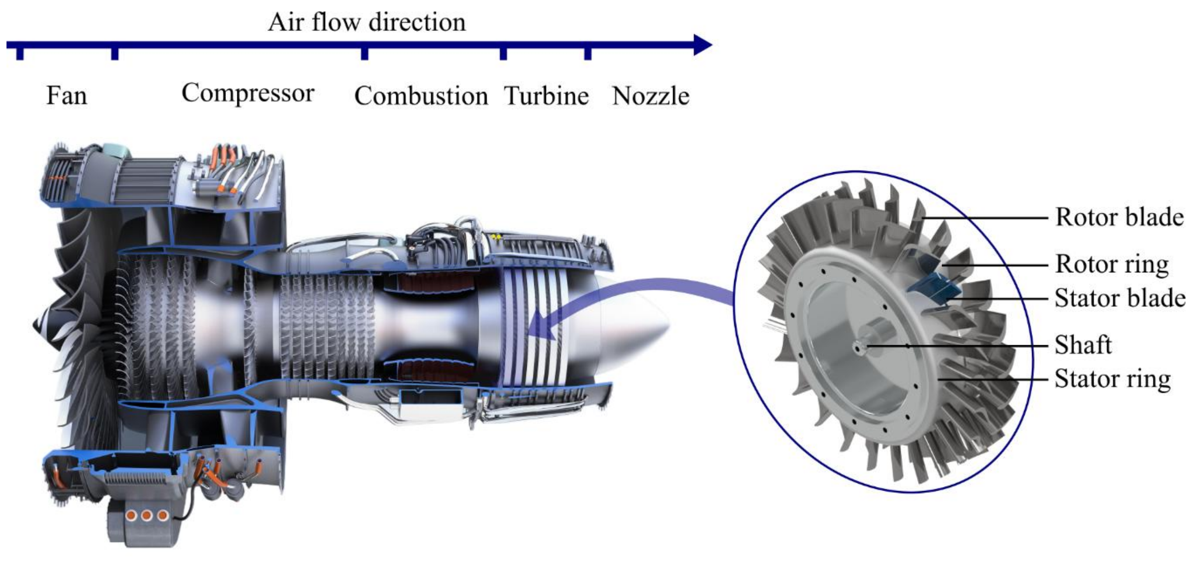

(a) (b)

Figure 1.3: Schematic of (a) a turbofan gas turbine engine adapted from [27] and (b) a turbine stage adapted from [28]

The high-pressure section of the turbine as shown in Figure 1.3(a) has turbine blades that are exposed to temperatures exiting the combustion chamber that exceed the melting point (~1200°C [1], [4]) of the turbine blade material (nickel-based super-alloy, e.g., Inconel 939 [1]). This extreme thermal loading on the blade causes damage, thus, reducing the lifespan of the blade. However, increasing the turbine inlet temperature (TIT) increases the work output [29] of the turbine and the overall efficiency of the gas turbine engine. To increase the lifespan of the blades whilst operating at high TITs, combinations of internal and external cooling techniques are introduced along different sections of the blade to cool the turbine blades. Depending on the application of the gas turbine engine and whether it is a rotor or a static blade, the blade design will vary to accommodate necessary cooling techniques.

1.2.2. Cooling of turbine blades

To reduce the temperature of the blades, internal and external cooling methods are implemented. Internal cooling consists of passages incorporated within the blade to extract heat from the blade. Cool air at ~700°C [1], [4] is bled from the compressor stage of the gas turbine engine and supplied to internal passages of the turbine blade. Pin-fins, passage blockages, dimples and angled ribs are some methods designed into the passages to increase the heat transfer away from the blade. This is accomplished by increasing the surface area of the passage exposed to the cool air as well as augmenting the turbulence within the channels [4]. The cool air flows through the internal configuration of the turbine blade and is ejected from the trailing edge as shown in Figure 1.4.

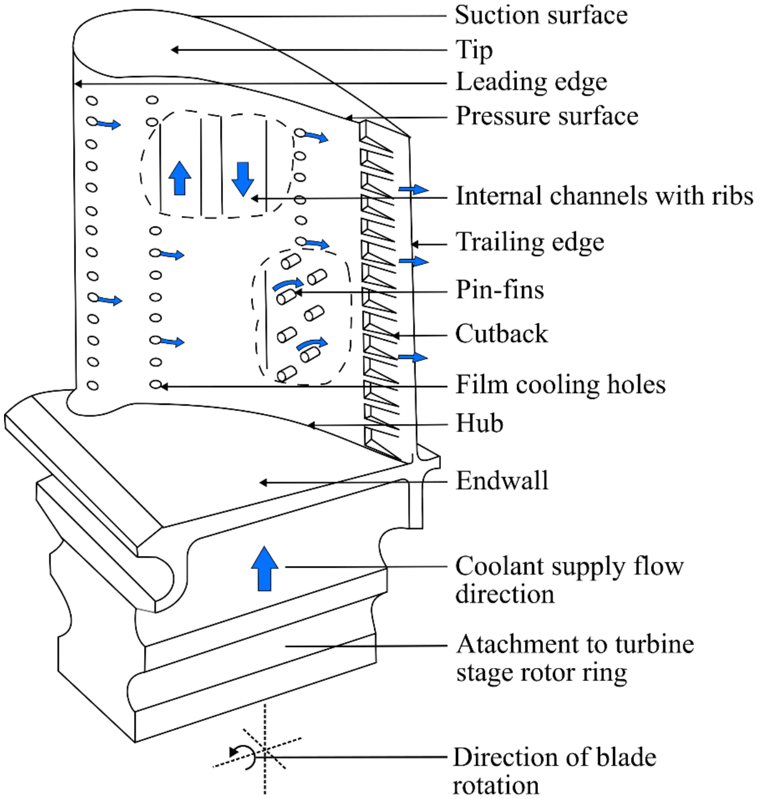

Figure 1.4: Annotated diagram of turbine rotor blade internal and external cooling adapted from [30]

External cooling as the name suggests targets the external surfaces of the turbine blade. The common use of external cooling is known as film cooling. This technique redirects the cool air supplied to the turbine blade to the external surface through strategically placed holes along the blade surface as shown in Figure 1.4. The technique is intended to act as a barrier between the hot mainstream gas and the blade surface by creating a thin “film” of cool air [31]. The positioning of the film cooling holes in the streamwise and spanwise direction of the blade depends on the mainstream air flow characteristics around the turbine blade. This is due to the complex nature of the flow around a turbine blade.

1.2.3. Air flow over a turbine blade

The airflow around a turbine blade can be analysed by observing two cases. Firstly, the two-dimensional flow around the airfoil profile representing a slice taken across the midspan of the turbine blade and secondly, the three-dimensional flow over a turbine blade considering the full span of a blade and adjacent blades. Considering the first case, the mainstream air encounters the turbine blade at the leading edge where the mainstream flow stagnates (known as the stagnation point as shown in Figure 1.5 where the velocity of the flow is zero) and diverges over the suction (convex) and pressure (concave) surfaces as seen in Figure 1.5. The static pressure difference between the suction surface (SS) and pressure surface (PS), summarized in Figure 1.5, applies a force on the blade known as the lift force. This resultant force creates a moment about the shaft axis that the rotor rings (and corresponding blades) are connected to thus resulting in the rotation of the turbine. As air flows over the SS and PS, a boundary layer, shown in Figure 1.5 develops over the surfaces due to viscous effects near the wall. Within the boundary layer, changes in the velocity, temperature and pressure affect the heat transfer rates across the blade surfaces.

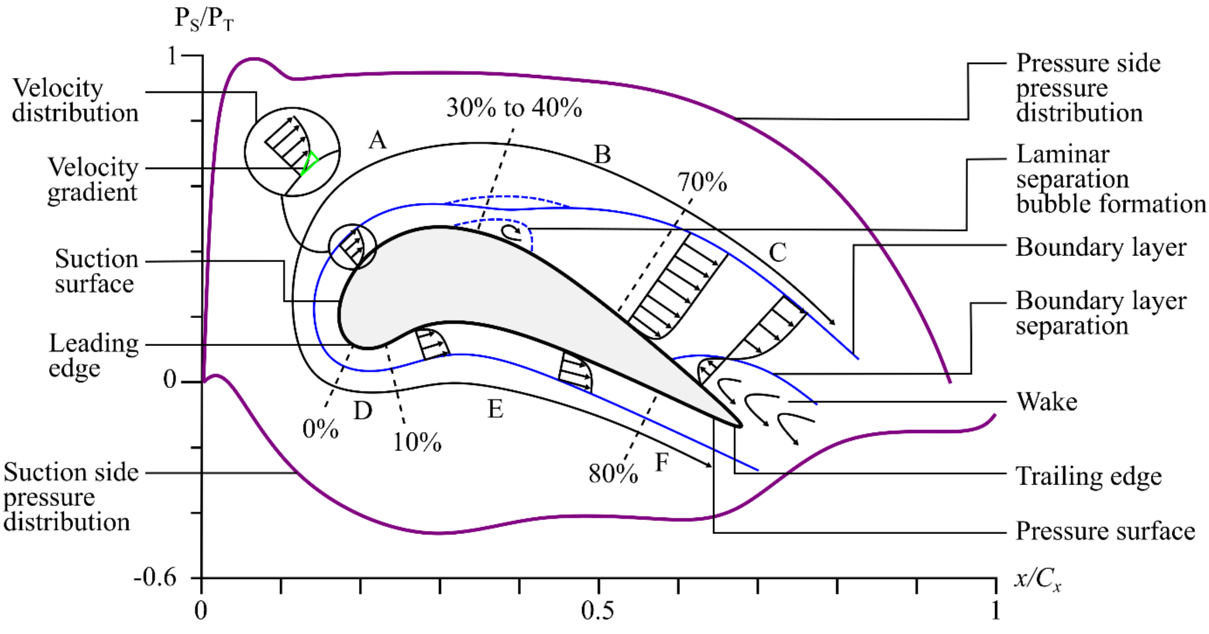

Figure 1.5: Summarised boundary layer and static pressure distribution around the mid span of a rotor blade for Reynolds numbers between $0.5 - 1.5 \times 10^6$ and turbulence levels of $2 - 10\%$ [13]– [22]

Suction surface

On the SS, the velocity of the air increases rapidly in section A from the stagnation point until 30% to 40% surface distance (SD) due to the decrease in static pressure across the leading edge as seen in

Figure 1.5. In this region the flow is laminar. High local heat transfer rates occur near the stagnation point due to the large velocity gradient ($\frac{\partial u}{\partial y}$) shown in Figure 1.5 but decrease towards 40% SD as the velocity gradient near the wall decreases. In section B, the pressure distribution is mostly constant with gradually increasing velocity as the flow begins to transition. The local heat transfer rate reaches a peak near the laminar to turbulent transition at 70% SD. The velocity of the air beyond 70% SD in section C begins to decrease due to the adverse pressure gradient (increasing static pressure) and the flow transitions to fully turbulent. The local heat transfer rate decreases in the turbulent region as the velocity gradient decreases relative to the transition region. The boundary layer thickness on the SS increases from 0.1 mm in the laminar region to 0.7 mm in the turbulent region as calculated by Ubaldi (1990) for a rotor blade with an axial chord length of 300 mm tested at a Reynolds number of 1.6×10^6 [40].

A laminar bubble, shown in Figure 1.5, is the detachment and reattachment of the boundary layer on the SS. The laminar bubble forms when the inlet Reynolds number is below a critical value depending on certain blade profiles [6], [21]. Near the trailing edge, boundary layer separation shown in Figure 1.5 occurs when the pressure increases to a point where the kinetic energy of the air particles cannot overcome the pressure gradient [41]. For separated flow, either in the laminar or turbulent boundary layer, the heat transfer rates are reduced below those in the attached boundary layer due to low momentum of the recirculating flow and heat exchange. However, as the separated region thickens, the turbulence levels increase which contribute to elevated heat transfer rates via turbulent mixing. At the point of reattachment, if any, the flow concentrates on a singular point and high heat transfer rates occur [41]. Separated flow negatively affects the aerodynamic efficiency of the turbine blade.

Pressure surface

Over the PS, the flow is accelerating slowly in section D to about 10% surface distance (SD) due to the increase in static pressure in this region as seen in Figure 1.5. The local heat transfer rate decreases to a minimum at 10% SD in this laminar region as the velocity gradient decreases rapidly at the wall. In section E, the velocity of the flow is gradually increasing due to the favourable pressure gradient (decreasing pressure). This region is characterised as a laminar-transitional region with an almost constant boundary layer thickness [40]. The local heat transfer rate remains near the minimum value in Section E. After 80% SD, in section F, the pressure decreases rapidly to a minimum at the trailing edge and the velocity increases rapidly. The local heat transfer rate increases towards the trailing edge as the flow in section F transitions and becomes turbulent. The boundary layer thickness does not increase in section F according to Ubaldi [40]. However, the constant boundary layer thickness with increased turbulent mixing causes increased blade temperatures near the trailing edge [5], [41].

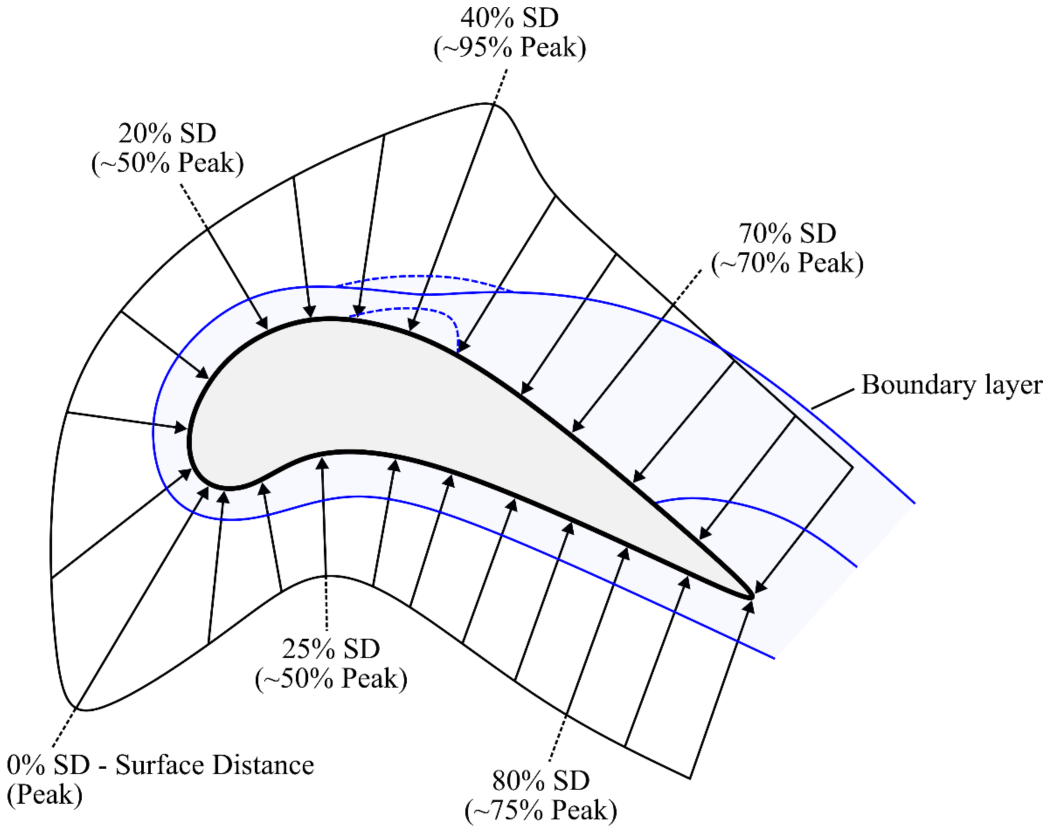

Figure 1.6: Heat transfer rate around a turbine blade based on data adapted from Han et al. [4] with a superimposed boundary layer flow

Secondary Flows

Apart from the two-dimensional boundary layer flow analysed, three-dimensional flows or otherwise known as "secondary flows" between turbine blades also affect the heat transfer rates and flow around the blades [42]. At the leading edge, shown in Figure 1.7, a horseshoe vortex forms as the endwall boundary layer rolls up into a vortical motion [43]. The horseshoe vortex diverges to the PS and SS as seen in Figure 1.7. The horseshoe vortex formation increases the turbulence intensity of the hot gas near the leading edge which contributes to the increase in temperatures in this region. The horseshoe vortex on the pressure side detaches from the leading edge of the PS due to strong pressure gradients between the PS and SS of opposite blades [44], [45]. This vortex becomes the passage vortex as it propagates between blades. The passage vortex detaches from the endwall surface as it approaches the SS of the adjacent blade. The suction side horseshoe vortex stays attached to the endwall and SS until it encounters and wraps around the passage vortex causing it to detach from the endwall. These secondary vortices coupled with strong pressure gradients between turbine blades causes flow on the PS to flow downwards towards the endwall and upwards on the SS towards the tip as seen in Figure 1.7.

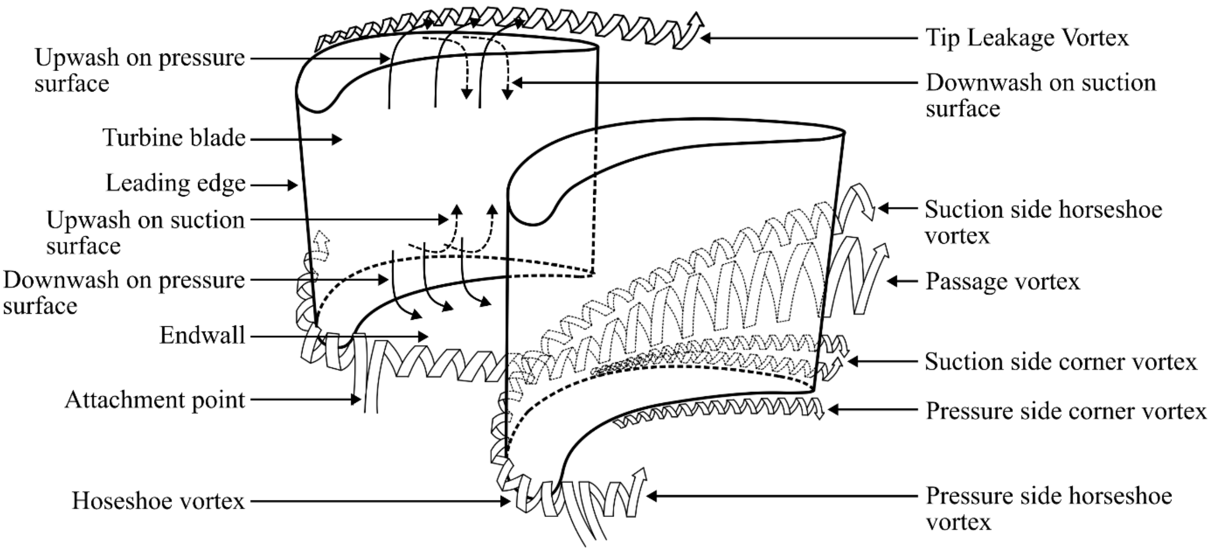

Figure 1.7: Secondary flows around a turbine rotor blade adapted from [4], [46]

At the tip of the rotor blade, a gap (~1% [31] of the spanwise length) exists between the blade and the casing. As the turbine rotates rapidly, the large pressure gradient between the PS and SS forces the flow over the blade creating a vortex on the SS known as the tip leakage vortex. This vortex drives the flow on the PS up near the tip and down on the SS as shown in Figure 1.7. The mainstream flow on the SS concentrates at the mid span, whereas flow on the PS is driven towards the tip and the hub away from the centre of the surface. These vortices increase the mixing of the mainstream air near the blade surfaces which has a significant influence on the heat transfer around turbine blades [46]. Specifically, over the passage endwall between blades, at the endwall corner of the blade, the leading edge and the trailing edge.

1.2.4. Location of film cooling holes

High heat transfer rates around the turbine blade are primary targeting points for the positioning of film cooling holes whilst considering the effects that the mainstream flow in those regions would have on the film coolant jets as the streamwise pressure gradient over the blade changes which affects the attachment of the coolant jet to the blade surface. As such, multiple arrays of film cooling holes are positioned along the blade surface, in the spanwise and streamwise directions for maximum possible coverage which varies between applications.

At present, several rows of film cooling holes are placed on the SS and PS as shown in Figure 1.8 to increase the coolant coverage whilst trying to reduce the dilution of the coolant to the mainstream flow. Showerhead cooling holes, shown in Figure 1.8, are closely spaced rows of film cooling holes (in the streamwise direction) placed by the stagnation point due to the high thermal loading experienced on the leading edge of turbine blades. Up to 5 holes are usually placed equidistant (in the streamwise direction) near the stagnation point. On the SS, 2 or 3 film cooling holes are placed at around 20%, 30% and 60% surface distance (SD). In earlier studies, Camci and Arts (1990) [37], Abuaf et al. (1997) [34], and Drost et al. (1997) [32] tested turbine blades with cooling holes placed only in the laminar region before 40% SD. However, more recent studies by Gao et al. (2008) [31], Liu et al. (2010) [38] and Narzary et al. (2012) [33] started testing with film cooling holes placed in the transitional region at around 60% SD. On the PS, 4 film cooling holes are used and positioned at around 15%, 30% and/or 50%, 65% and only at 75% SD in Gao et al. (2008) [31] and Narzary et al. (2012) [33]. These holes vary between cylindrical and shaped holes angled at around 30° to 45° from the blade surface.

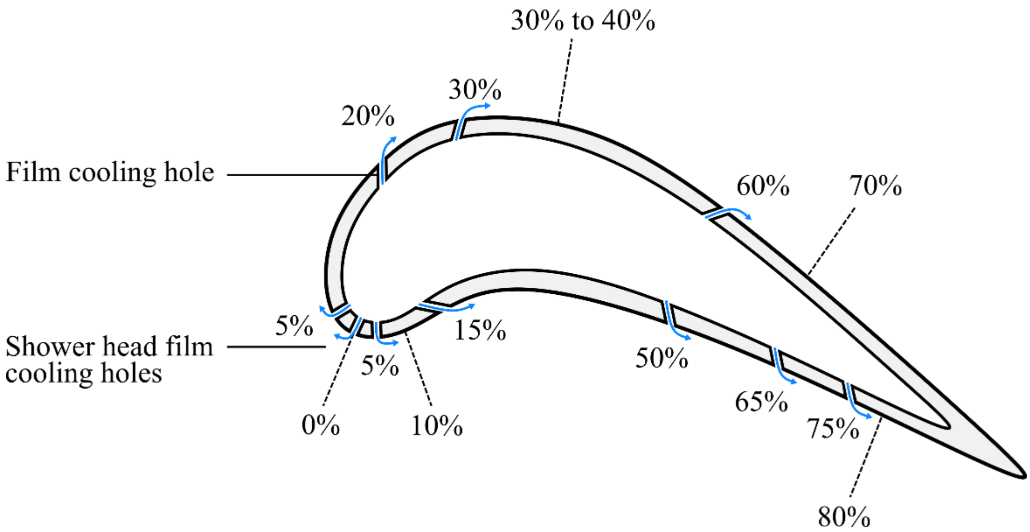

Figure 1.8: Summarised film cooling hole positions around the mid span of a rotor blade for several different studies on improving film cooling parameters (percentages reflect the distance over the blade surface) [14]– [16], [19], [20]

From the summarised studies in Figure 1.8, film cooling holes are seen to be placed in common sections of the blade where the flow is rapidly accelerating in laminar or transitional boundary layers and in regions of high heat transfer rates. Specifically, rows of film cooling holes are placed near the leading edge, transition region on the SS and near the trailing edge on the PS. The ratio between the hole diameter of the film cooling holes to boundary layer thickness (D/δ) varies across the turbine blade due to the influence of the pressure gradient on the boundary layer as shown in Figure 1.5 and Figure 1.6. Previous papers have used a range of D/δ in their studies. Jessen et al. [16] $D/\delta = 0.5$, Sinha et al [47] $D/\delta = 0.5$ to 3.0, Schmidt et al [24] $D/\delta \sim 2.5$, Eberly et al. [48] $D/\delta \sim 0.8$, Johnson et al. [49] $D/\delta = 1.0$, Colban et al. [50] $D/\delta \sim 0.8$. A broad range can be found where lower values of D/δ represent a larger boundary layer (considering an adverse pressure gradient near the trailing edge), and higher values of D/δ represent thinner boundary layer (considering a favourable pressure gradient near the leading edge).

1.2.5. Structure of film cooling jet

The coolant jet ejection through film cooling holes immediately interacts with the mainstream flow around the turbine blade. This subsequent interaction behaves the same way as a jet in crossflow. It is important to note that, although a jet in crossflow under a streamwise pressure gradient have not been looked at in detail, the understanding of the flow structure of a jet in crossflow aids in the interpretation of the results.

The ejection of the secondary flow through a film cooling hole immediately impedes the path of the mainstream flow, leading to the formation of a stagnation region at the leading edge of the coolant jet. This stagnation occurs as the momentum of the coolant jet locally opposes that of the mainstream flow, causing a region of high pressure at the upstream interface between the two streams [51]. The mainstream flow, unable to pass directly through this stagnation zone, is forced to diverge in multiple directions: part of the flow is deflected laterally around the jet column, part is directed downward towards the endwall surface, and a portion moves in the upstream direction, creating a reverse flow region [22], [52], [53].

This reverse flow upstream of the jet column, combined with the lateral deflection of the mainstream fluid, induces boundary layer separation near the endwall. As the boundary layer lifts off or detaches from the endwall, it generates a recirculating flow structure that wraps around the jet column, forming a distinct vortex system known as the "Horseshoe vortex (HSV)" [44] [8], [9]. The formation of the horseshoe vortex is primarily influenced by the interaction between the high-momentum mainstream flow and the lower-momentum in the streamwise direction of the coolant jet, thus, creating strong shear forces that drive the vortex development [20] [8], [9].

Once formed, the horseshoe vortex does not remain stationary but propagates downstream along the surface of the endwall, carried by the surrounding flow. As it moves, it undergoes further development and stretching, which can lead to its eventual breakdown far downstream of the ejection point. The HSV remains a dominant feature in the near-field wake of the film cooling hole, significantly affecting both heat transfer characteristics and mixing efficiency between the coolant and mainstream flow [4], [5], [8]. The presence of the HSV and the associated flow recirculation can also create regions of increased local heat transfer due to vortex-induced mixing, which may lead to localized hot spots and reduce the cooling film's effectiveness [4], [5].

Another vortical structure apart from the horseshoe vortex system is present in a jet in crossflow. A closer look the structure of a jet in crossflow reveals that the jet core consists of a pair of counter-rotating vortices, commonly referred to as the "Kidney vortex" [4], [8], [9]. This vortex forms at the interface between the mainstream flow and the coolant jet, where a thin shear layer of thickness ϵ develops due to the sharp increase in tangential velocity between the jet and the mainstream flow (as illustrated in Figure 1.1(a)), with $\epsilon \rightarrow 0$ [11]. This abrupt velocity gradient results in a discontinuity in tangential velocity, inducing vorticity within the shear layer and leading to the formation of a cylindrical vortex sheet [8], [9], [11], [14].

The flow in this cylindrical vortex sheet is inherently unstable due to the Kelvin-Helmholtz instability, which occurs when two parallel fluid streams of different velocities interact, leading to the growth of shear-layer perturbations and the eventual roll-up of the vortex sheet [11]. This instability is driven by velocity differences across the shear layer, where small disturbances in the interface between the mainstream and jet amplify over time, forming coherent vortex structures [8], [9], [11]. As this instability evolves, the cylindrical vortex sheet rolls up into distinct vortex loops, as shown in Figure 1.1(b), leading to the formation of three dominant vortex structures: (i) leading-edge vortices, (ii) lee-side vortices, and (iii) Kidney vortices [8]. The leading-edge and lee-side vortices arise from the natural roll-up of the shear layer, whereas the Kidney vortices develop at the periphery of the jet where it interacts with the mainstream flow (around $y \approx 0$) [8]. Here, the vortex sheet folds along its edges in the direction of the mainstream flow, initiating the formation of a counter-rotating vortex pair, labelled as "(i)" in Figure 1.1(b).

The counter-rotating vortices in the jet core induce an inward rotational motion, pulling the outer boundary of the jet toward the centre. This inward motion generates a net upward force on the jet, influencing its trajectory and contributing to its detachment from the surface [10]. The detachment occurs at a location denoted as y_1 (as indicated in Figure 1.1(a)), where the jet is lifted off due to the interaction of the induced vortex motion with the mainstream flow [10]. This detachment creates a region of low-velocity recirculating flow immediately downstream of the film cooling hole [9].

Additionally, the detached jet forms a wake region downstream, where the interaction of the counter-rotating vortex pair with the surrounding flow results in complex turbulence and mixing effects [11]. The wake consists of recirculating flow zones and vortex shedding, which enhance entrainment of mainstream air into the jet [7], [15]. This entrainment can cause cooling air to be drawn away from the surface, reducing film cooling efficiency.

Overall, the combined effects of Kelvin-Helmholtz instabilities that lead to the development of the kidney vortex in the jet core induce the jet to detach or move away from the wall creating wake formations that play a crucial role in affecting both the cooling performance and aerodynamic behaviour of the jet.

1.2.6. Effect of blowing ratio on film cooling effectiveness

There are several parameters that can affect the structure of a film cooling jet and consequently the film cooling effectiveness. For example, blowing ratio, streamwise pressure gradient, and hole geometries including hole angle, shape, and size are some examples of these parameters. The hole geometry was analysed from previous studies and real-world gas turbine blade applications to select the necessary hole geometry for this study. The blowing ratio and streamwise pressure gradient are two important characteristics that will be looked at in this study as these parameters have previously been shown to have a direct influence on the film cooling effectiveness.

As mentioned in the introduction, the blowing ratio is the mass flux of the coolant relative to that of the mainstream, defined as $M = \rho_c v_c / \rho_m v_m$ where ρ is the density and v is the velocity with the subscripts c and m referring to the coolant and mainstream flow, respectively [4], [23], [26] The blowing ratio varies between 0.5 and 2.0 depending on application and previous studies have, in majority, investigated between this range to optimise the film cooling effectiveness. The effects of blowing ratio, in isolation, i.e. no induced pressure gradient, have been studied directly and indirectly between studies with a common outcome.

At lower blowing ratios ($M << 1.0$) the coolant is released with low momentum relative to that of the mainstream leading to rapid diffusion, low lateral surface coverage, but with near field increased film cooling effectiveness [4], [12]. At higher blowing ratios ($M >> 1.0$) the coolant jet penetrates the mainstream flow due to excessive momentum, lifting off from the surface and reducing its ability to provide effective cooling [4], [12]. This phenomenon, known as jet detachment, results in increased heat transfer to the surface due to reduced coolant coverage. Additionally, higher blowing ratios intensify vortex structures, such as the kidney vortex and horseshoe vortex, further promoting coolant entrainment into the jet and diminishing film cooling efficiency [8], [12]. Therefore, selecting an appropriate blowing ratio is essential to balance coolant coverage, aerodynamic losses, and thermal protection in gas turbine cooling applications. However, although simply stated, in gas turbine blades, the complex nature of flow around the turbine blade increases the difficulty in simply improving a single parameter such as optimising the blowing ratio.

1.2.7. Effect of hole geometry on film cooling effectiveness

The shape and size of holes play another significant role in the improvement of film cooling effectiveness. A hole at 90° to the surface is less effective than a hole placed at any acute angle to the surface. Goldstein et al. [10] and Jubran et al. [54] found that regardless of blowing ratio, decreasing the hole angle, $\theta < 90°$ improved the film cooling effectiveness as the tangential component of the coolant jet increased relative to the normal velocity component driving the coolant jet closer to the endwall surface thus increasing the coolant coverage. Haven et al. [20] conducted water tunnel experiments to investigate the impact of hole exit geometry on the "near-field characteristics" of crossflow jets. The studied hole shapes (round, elliptical, square, and rectangular) had identical cross-sectional areas. Laser-induced fluorescence (LIF) and particle image velocimetry (PIV) were used in this experiment for flow measurement and visualisation. The results showed that a wider hole increased the lateral separation of the counter-rotating vortices, shown as z_1 in Figure 1.1, thus reducing the detachment of the coolant jet. A study by Lange et al. [12] observed the interaction between the mainstream and coolant jet with different hole geometries, cylindrical, rectangular and triangular in a constant area channel. This study used laser induced fluorescence, particle image velocimetry and thermo-chromic liquid crystal to uncover the structure of the flow. The results showed that a circular cross section performed better than the other geometries used over the range of blowing ratios implemented $0.5 < M < 1.5$. Additionally, the results from the laser induced fluorescence showed how the attachment of the coolant jet improved with a decrease in blowing ratio.

An inclined cylindrical hole is commonly used in gas turbine applications due to its simplicity in manufacturing. In gas turbine applications, these cylindrical holes are commonly inclined between 30°-45° to the blade surface for improved adhesion of the coolant jet to the surface [1], [4].

1.2.8. Effect of streamwise pressure gradient on film cooling effectiveness

The streamwise pressure gradient significantly influences the interaction between the coolant jet and the mainstream flow, thereby affecting film cooling effectiveness. In a favourable pressure gradient (where the pressure decreases in the streamwise direction), the boundary layer undergoes convective acceleration, resulting in a thinner boundary layer upstream of the coolant ejection point [22], [24]. This acceleration increases the stagnation pressure on the impinging coolant jet, generating a higher-pressure region at the jet's leading edge. The pressure difference between the upstream and downstream regions of the ejection point induces a net downward force on the coolant jet column, pushing it closer to the blade surface [22]. As a result, the jet remains attached to the surface for a longer distance, ensuring better surface coverage and enhancing film cooling effectiveness [24], [47]. Additionally, the thinner boundary layer allows for better coolant penetration, reducing mainstream entrainment and further improving cooling performance [12], [20].

Conversely, in an adverse pressure gradient (where the pressure increases in the streamwise direction), the boundary layer flow undergoes deceleration, leading to boundary layer thickening [16]. A thicker boundary layer reduces the mainstream velocity near the wall, diminishing the stagnation pressure on the coolant jet. This weakens the downward force on the jet, causing it to penetrate further into the mainstream flow rather than adhering to the blade surface. As a result, jet lift-off occurs, reducing the coolant's ability to provide effective thermal protection[16], [17].

2 Critical Research Question

How do streamwise pressure gradients (favourable, mild favourable, zero, and adverse) affect the attachment, kidney vortex development and endwall topology of a film cooling jet at various blowing ratios?

3 Objectives

- To determine the effect of blowing ratio (M = 0.5, 1.0, and 1.5) on the attachment of a film cooling jet under zero pressure gradient.
- To determine the effect of streamwise pressure gradient (favourable, mild favourable, zero, and mild adverse) on the attachment of a film cooling jet at blowing ratios between M = 0.5 and 2.0 in increments of M = 0.1.
- To map the structure of a film cooling jet (attachment, detachment, kidney vortex spacing, and endwall structure) at different blowing ratios and streamwise pressure gradients (favourable, mild favourable, zero, and mild adverse) using particle image velocimetry, planar laser visualisation, and endwall oil-dye visualisation.

4 Experimental Methods

An experimental study was performed to determine the effect that pressure gradients and blowing ratios have on the attachment and detachment of a coolant jet of a turbine blade under gas turbine engine representative conditions. The experimental analysis was conducted by considering the effects the blowing ratio and pressure gradient have on the coolant jet. The flow over a turbine blade as mentioned in previous sections is complex and three-dimensional with several secondary vortical structures influencing the boundary layer flow over the blade surface specifically near the hub and tip of the turbine blade. A two-dimensional slice of the midspan of the turbine blade is considered for this investigation to isolate the boundary layer flow without the influence of secondary vortical structures as shown in Figure 4.1.

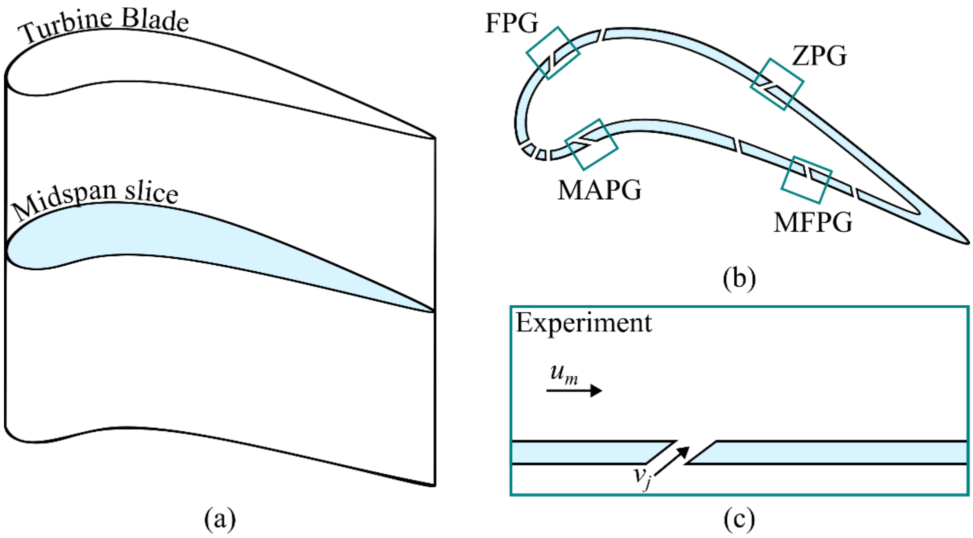

Figure 4.1: Experimental breakdown from (a) midspan slice of turbine blade to (b) cross section of midspan slide of turbine blade with holes to (c) a flat surface experiment setup isolating a section of the turbine blade (pressure gradient and blowing ratio)

Four pressure gradients taken over a turbine blade surface were replicated in this study as shown in Figure 4.1. These include a favourable pressure gradient (near the leading edge on the suction surface where the boundary layer flow velocity is increasing), a mild favourable pressure gradient (near the trailing edge over the pressure surface of a turbine blade), a zero pressure gradient (where the boundary layer flow over the suction surface transitions from laminar to turbulent flow) and a mild adverse pressure gradient (taken near the leading edge of the pressure surface of a turbine blade where the boundary layer flow velocity is decreasing) as shown in Figure 4.1. The favourable (FPG), mild favourable (MFPG), zero (ZPG), and mild adverse (MAPG) pressure gradients are replicated in a continuous suction-type wind tunnel through variation of the upper endwall surface in the test section. Pressure measurements were taken across the test section to quantify the pressure gradient imposed. Planar laser visualisation was used to visualise the coolant jet structure, plume height and detachment lengths. Particle image velocimetry was used to map the velocity vector field to quantify the velocity of the jet and mainstream flow and to capture the structure of the kidney vortices. Endwall visualisation was accomplished with a fluorescent oil-dye mixture.

4.2 Test rig

Figure 4.2(a and b) show schematics for the experimental setup and test section that was conducted in a closed-circuit suction-type wind tunnel. Four configurations of the test section, with varied contoured upper walls, were implemented to vary the pressure gradient across the channel. The inlet area had dimensions, height (H) × width (W) of 250.0 mm × 100.0 mm respectively. The length (L) of the channel was 1200.0 mm with a test section length (L_T) of 820.0 mm as shown in Figure 4.2. The exit heights of the channel were 100.0 mm, 150.0 mm, 250.0 mm and 320.0 mm as shown by h_1, h_2, h_3, and h_4 in Figure 4.2(b) corresponding to favourable (FPG), mild favourable (MFPG), zero (ZPG) and mild adverse (MAPG) pressure gradients respectively. A constant area single cylindrical hole with a diameter of D = 20.0 mm and a length of 124.0 mm was positioned in the centre of the test section (x, y and z = 0, with a relative position to the inlet of L_{hole} = 410.0 mm) at an angle of θ = 30° to the lower endwall as shown in Figure 4.2. This hole configuration was selected as it is commonly implemented across turbine blades due to its simple geometry and improved film cooling effectiveness [4]. This is the case as the normal velocity vector component of the coolant jet is reduced relative to the tangential component, thus, reducing detachment of the coolant along the blade surface [10], [53]. Additionally, the hole diameter of 20 mm was selected as it was necessary for velocity field measurement and flow visualisation purposes, where a larger jet diameter enables more velocity vectors to be resolved, thus, increasing the spatial resolution. Moreover, to adhere to engine representative testing conditions used in literature, the mean mainstream and secondary flow velocities were calibrated based on the Reynolds number, blowing ratio, and the hole to boundary layer flow ratio. A 20 mm hole diameter was selected as this hole diameter provided the necessary flow conditions based on the ranges of Reynolds number (10 000 to 27 000), blowing ratios (0.5 to 2.0), and hole to boundary layer flow ratio (0.5 to 3.0) used in literature to represent engine representative testing conditions [4], [16], [31], [32], [50], [55].

The channel was manufactured using transparent acrylic sheets with a thickness of 10.0 mm. The design with technical drawings and assembly of the test section is outlined in Appendix A and Appendix F. The use of transparent acrylic walls for the test section was necessary to allow for optical access to capture the behaviour of the secondary flow jet in crossflow. A honeycomb mesh was placed at the inlet of the constricted test section where a bell-mouth entry was placed to direct the flow from the large cross-sectional area of the main wind tunnel (width × height of 320.0 × 320.0 mm) to the cross-sectional area of the test section. Table 4.1 shows the summary of the tested parameter values.

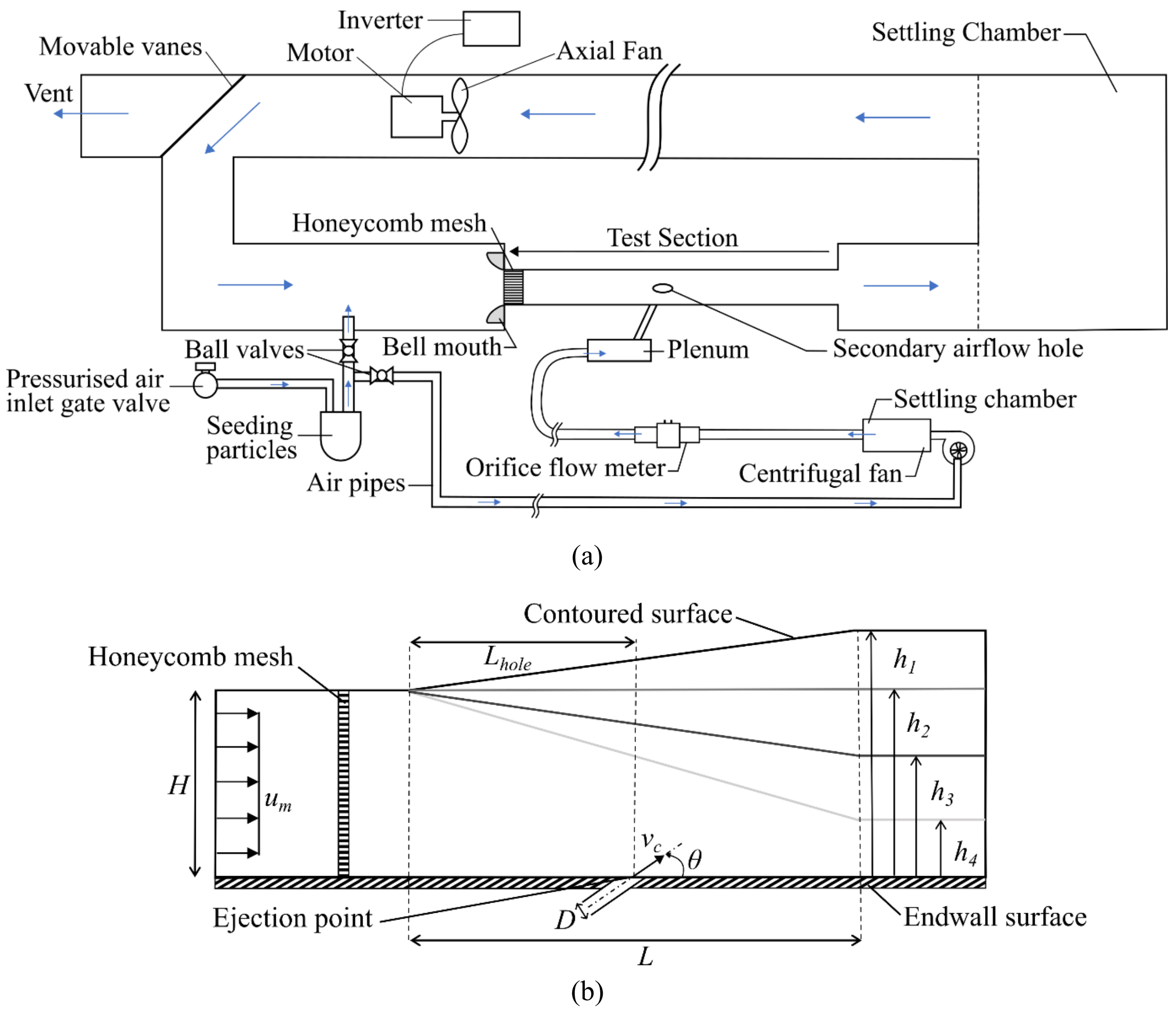

Figure 4.2: Schematics for the (a) experimental setup and (b) favourable, mild favourable, zero and mild adverse pressure gradients generated in the test section by endwall contouring

The primary air flow was drawn into the test section by an axial fan downstream of the test section controlled by a frequency inverter. A honeycomb mesh was placed upstream of the test section to straighten the flow prior to entering the test section. The primary airflow velocity over the ejection hole was set to maintain a Reynolds number of $Re_D \sim 1.4\times10^4$, relative to the cylindrical hole diameter as follow [6], [21], [56]:

$$Re_D = \frac{\rho_m u_m D}{\mu_m} \quad (1)$$

Where: ρ_m is the density of the air in the mainstream flow, u_m is the mainstream flow velocity at the hole location, μ_m is the kinematic viscosity of the mainstream flow and D is the diameter of the cylindrical hole of the coolant supply. The mainstream velocity of the test section was measured using a pitot tube connected to a 16-channel digital manometer DSA 3217. The differential pressure obtained by the digital manometer was averaged across 240 readings obtained over 10 seconds for every 5.0 mm intervals across the channel height. The pressure readings were converted into local velocities to obtain the inlet velocity profiles and the corresponding integral mean velocity, u_m ~ 11 m/s.

The coolant or secondary airflow was supplied via a centrifugal DC fan, placed 2000.0 mm upstream of the ejection point, controlled by a frequency inverter. A 21.0 mm inner diameter pipe was connected between the centrifugal fan and a plenum. The plenum had a width × length × height of 80.0 mm × 400.0 mm× 80.0 mm and was placed 100.0 mm below the bottom surface and connected via a 20.0 mm inner diameter pipe with a length of 124.0 mm to the hole on the bottom surface of the test section. The plenum dimension range were conducive to plenum dimensions used in literature [57], [58], [59], [60], [61]. Various fan speeds were calibrated using both a pitot tube and orifice flow meter to determine the flow rate of the secondary flow. More information on the construction of the experimental setup and calibration can be found in Appendix A and Appendix B respectively.

Table 4.1: Channel measurements and testing parameters

Parameters	Values
Re_D	14 000
Mean velocity of mainstream, u_m (m/s)	~11
Mean velocity of film cooling jet, v_j (m/s)	~5.5 to 22.0
T_c/T_m	1
Blowing ratio, M	0.1 increments from 0.5 to 2.0
Film cooling hole diameter, D (mm)	20
Test section inlet height, H (mm)	250
Test section width, W (mm)	100
Test section exit height h_1, h_2, h_3, h_4 (mm)	100.0, 150.0, 250.0, 320.0
L (mm)	820.0
L_{hole} (mm)	410.0
θ (degrees)	30.0

4.3 Calibration of Test rig

4.3.1 Pressure in mainstream vessel

The pressure gradient across the channel was varied by introducing a contoured upper endwall in the test section that varied the cross-sectional area through the channel as shown in Figure 4.2(b). Pressure taps were placed along the bottom endwall surface of the channel to record the pressure variation for each upper endwall configuration namely, favourable, mild favourable, zero and adverse as represented by channel exit heights h_1, h_2, h_3 and h_4 respectively in Figure 4.2(b). The exit heights were varied to recreate the pressure gradient over a turbine blade surface. The turbine blade pressure distribution was obtained from a paper by Behr et al. [55] that implemented engine representative conditions.

The pressure distribution across the test section was evaluated experimentally by placing 16 pressure taps flush along the endwall surface of the test channel connected to a 16-channel digital manometer

DSA 3217. The differential pressure obtained by the digital manometer was averaged across 240 readings obtained over 10 seconds for every pressure tap simultaneously. The pressure taps were made using 21-gauge needles attached to silicon tubing that were connected to the digital manometer to record the differential pressure at the specified locations. The static pressure variation across the bottom endwall was recorded and compared to engine representative pressure variation over sections of a turbine blade compiled by Behr et al. [55] as shown in Figure 4.3.

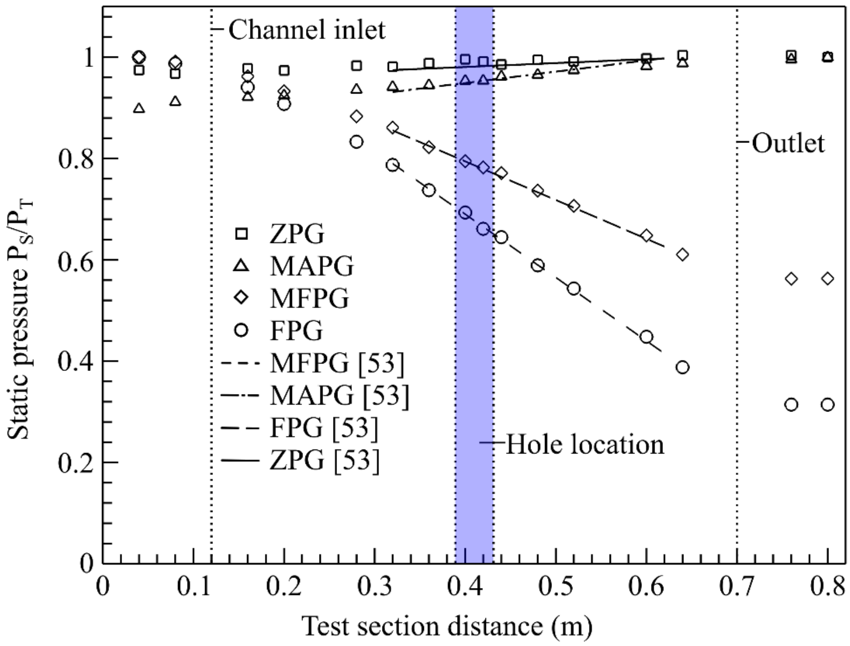

Figure 4.3: Static pressure distributions along the lower surface for favourable (FPG), mild favourable (MFPG), zero (ZPG), and mild adverse (MAPG) pressure gradients

4.3.2 Acceleration parameter

The pressure gradients were further quantified using the acceleration parameter, *K*, defined in following the study [62] as:

$$K = \frac{v_m du_m}{u_m^2 dx} \tag{3}$$

Where v_m is the kinematic viscosity of the primary flow, u_m is the streamwise velocity of the primary flow and du_m/dx is the derivative of the streamwise velocity with respect to *x*, the streamwise distance. The acceleration parameter was measured based on the local static pressure measurements in Figure 4.3 and the freestream flow velocity at the hole location for each channel. For the favourable, mild favourable, zero and mild adverse pressure gradients the acceleration parameters were, $K = 2.61\times10^{-6}$, $K = 1.53\times10^{-6}$, $K = 0.00\times10^{-6}$ and $K = -0.31\times10^{-6}$ respectively. These values are comparable to those obtained by Qin et al. [17] (K = -0.23×10^{-6}, 0, and 0.72×10^{-6}), Ammari et al. [63]

(K= 5×10^{-6}, 1.9×10^{-6}, and 0), Teekeram et al. [26] (K = 2.62×10^{-6}, 1.54×10^{-6}, 0.76×10^{-6}, and -0.22×10^{-6}), Pai and Whitelaw (K = 1×10^{-6}, 1.82×10^{-6}, and 3.30×10^{-6}), Maiteh et al. [64] (K = -1.11×10^{-6}, and 1.11×10^{-6}), and Jessen et al. [16] (K = -0.5×10^{-6}, and 0). The range of acceleration parameters varies between papers due to the experimental inlet conditions selected. However, the pressure gradient (*dP/dx*) through the channel as shown in Figure 4.3. is the same compared to previous papers and turbine blade data which the contour surface calculations were based on.

The local velocity in the *x*-direction is calculated based on the change in area through the test section by substituting the continuity equation into Bernoulli's equation as follows [56], [65]:

$$v_2 = \sqrt{\frac{(P_1 - P_2) + 0.5\rho v_1^2}{0.5\rho}} \tag{4}$$

Where P is the local static pressure in Pa, and v is the local velocity through the channel in m/s at the local positions denoted by subscripts *1* and *2,* where *1* represents an upstream position relative to *2*. The variation in the local velocity was mapped out accordingly against the local *x*-direction position in the channel. The derivate of the mainstream velocity was subsequently calculated.

4.3.3 Blowing ratio (*M*)

The flow rates implemented were based on blowing ratios (M), which is the mass flux of the coolant relative to that of the mainstream flow [66], [67]:

$$M = \frac{\rho_c \bar{v}_c}{\rho_m \bar{u}_m} \tag{5}$$

Where: ρ is the density of air (calculated based on the ambient temperature and pressure using the ideal gas law) with subscripts *c* and *m* denoting the secondary jet and mainstream flow respectively, $\bar{v}_c$ is the mean velocity of the secondary jet flow and $\bar{u}_m$ is the mean mainstream velocity. As the temperature of the air for the secondary and mainstream airflow was the same, the density ratio becomes, $\frac{\rho_c}{\rho_m} = 1$. As such, the blowing ratio becomes only a function of the mean velocity ratio between the coolant jet and the mainstream flow, $\frac{\bar{v}_c}{\bar{u}_m}$.

The blowing ratio was set, for the initial tests, to M = 0.5 (for the MAPG and MFPG), 1.0 (for the ZPG), and 1.5 (for the FPG) as per blowing ratios observed from preliminary numerical simulations and past papers. The blowing ratio was increased or decreased in increments of 0.1 between these primary blowing ratios to analyse the specific blowing ratio at which the secondary flow transitioned from attached to detached away from the endwall surface.

4.3.4 Mainstream and secondary velocity profiles

Transverse velocity profiles of both the mainstream and secondary flow were taken in isolation of one another to reduce interferences that each may cause on the other. The local velocity of the mainstream flow (relative to a change in the *y*-direction across the centre of the channel) was calculated using a pitot tube directly at the centre of where the hole would be placed (410.0 mm from the test section inlet). Figure 4.4 shows the velocity distribution of the channel for the favourable, mild favourable, zero and mild adverse pressure gradients. Initially, the mainstream axial velocity $u(y)$ along the test section height H (i.e., the y-axis in A-A') was measured at the centre of the film cooling jet's exit as shown by the inset of Figure 4.4(a). The mean velocity of the mainstream (u_m) was set for the Reynolds number of Re_D = 14,000, based on the film cooling jet diameter (D). It should be noted that the present Reynolds number lies within the range comparable to Gao et al. (Re_D ~ 10,000) [31], Drost et al. (Re_D ~ 27,000)[32], Day et al. (Re_D ~ 21,000)[68], Sakar et al. (Re_D ~ 8,000) [69], Colban et al. (Re_D ~ 24,000) [50], and Camci et al. (Re_D ~ 13,000) [37], that are claimed to be representative of typical film cooling conditions in a gas turbine, and further allowing for the comparison to the flat plate experimental setup.

The boundary layer height (δ) varied between test section configurations as seen in Figure 4.4 due to the imposed pressure gradient through the test section. The data from both Pitot tube and PIV (to be described in detail in the following section) consistently shows that the mainstream has a uniform profile outside of the boundary layer, and the corresponding boundary layer thickness is δ ~ 25 mm (or δ /H ~ 0.10) for the ZPG. As a finite yet set pressure gradient was imposed, the thickness of a boundary layer varies as being δ ~ 15 mm (or δ /H ~ 0.09) for the FPG, δ ~ 20 mm (or δ /H ~ 0.10) for the MFPG, and δ ~ 30 mm (or δ /H ~ 0.11) for the MAPG as shown in Figure 4.4. The thinning of the boundary layer is caused by both favourable pressure gradients (FPG and MFPG) whereas thickening occurs with the adverse pressure gradient (MAPG). Moreover, the relation of the hole to boundary layer thickness (D/δ) varies depending on the streamwise pressure gradient imposed. For a FPG, D/δ = 1.3 (δ = 15 mm), for a MFPG, D/δ = 1.0 (δ = 20 mm), for a ZPG, D/δ = 0.8 (δ = 25 mm), and for a MAPG, D/δ = 0.7 (δ = 30 mm). These values fall within the range of D/δ found in literature covered in §1.2.4.

From PIV and the Pitot tube both show that the jet exit velocity profile is independent of the blowing ratio since the reduced velocity data collapse well onto a single curve under the zero-pressure gradient (ZPG). Similarly, this relationship was also seen for the favourable (FPG), mild adverse (MFPG), and adverse pressure gradient (MAPG).

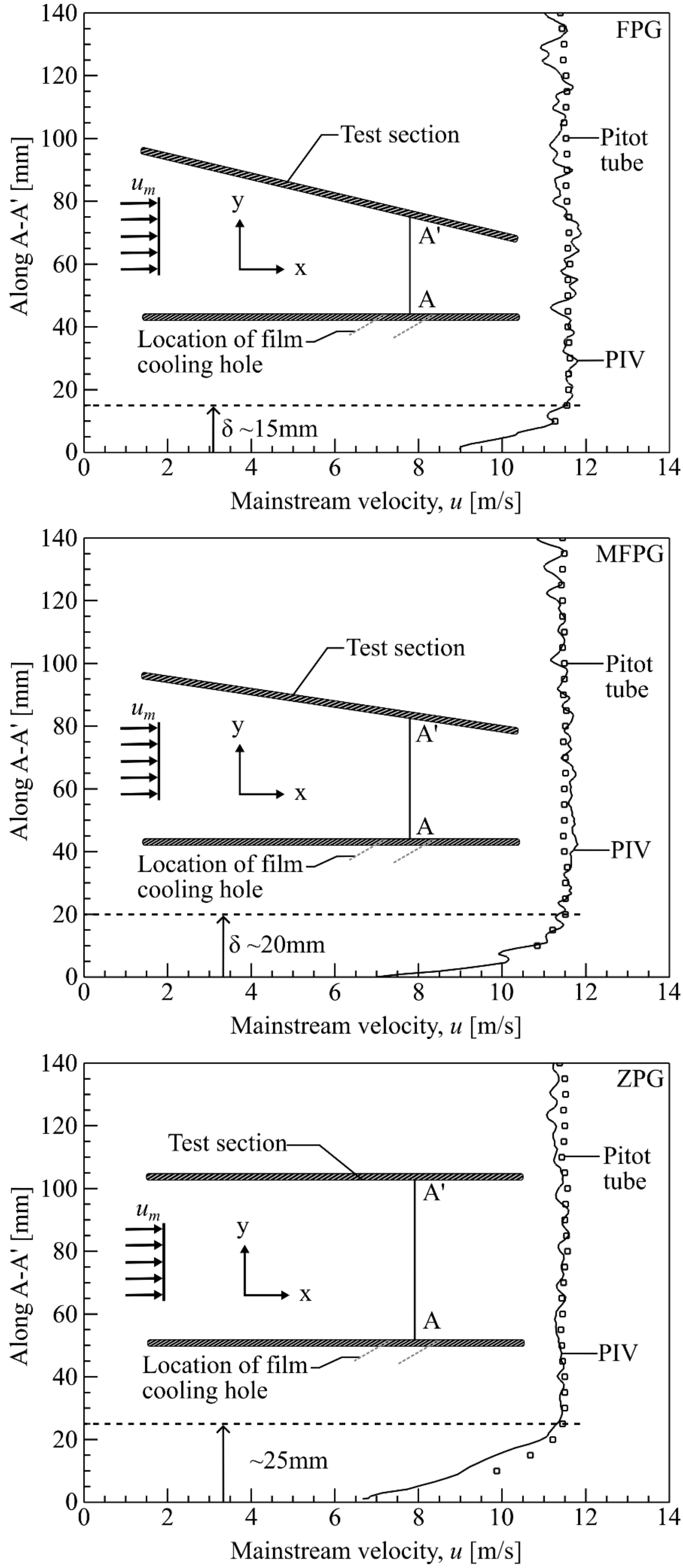
FPG
Test section
Pitot tube
PIV
A'
A
y
x
Location of film cooling hole
δ ~15mm
Along A-A' [mm]
Mainstream velocity, u [m/s]
MFPG
Test section
Pitot tube
PIV
A'
A
y
x
Location of film cooling hole
δ ~20mm
Along A-A' [mm]
Mainstream velocity, u [m/s]
ZPG
Test section
Pitot tube
PIV
A'
A
y
x
Location of film cooling hole
~25mm
Along A-A' [mm]
Mainstream velocity, u [m/s]

(a)

(b)

(c)

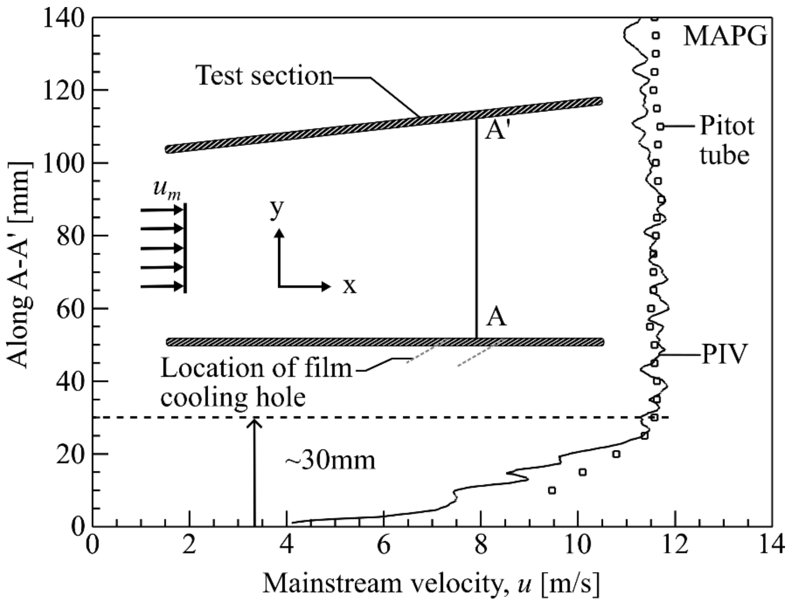

(d)

Figure 4.4: Mainstream local velocity at x = 410.0 mm taken along A-A' for (a) FPG, (b) MFPG, (c) ZPG, and (d) MAPG, without a secondary flow present (coolant hole was blocked for this data set)

The mean velocity was calculated based on the area weighted average of the local velocities as a function of their positions through the channel height as follows [56], [70], [71]:

$$\bar{u}_m = \frac{1}{A}\int_0^A u(y)dA \tag{6}$$

Where: $u(y)$ is the local velocity as a function of the y-position across the channel height, and A is the cross-sectional area of the channel at the hole location. The mean velocity for the FPG, MFPG, ZPG, and MAPG was 11.13 m/s, 11.05 m/s, 11.01 m/s, and 11.01 m/s respectively. The velocity profile for the secondary flow was extrapolated along B-B' (normal to the oncoming flow which corresponds to an obtuse angle of 120°) as shown in Figure 4.5 at the exit of the hole. Local velocities were collected in intervals of 1 mm up to the extent of the jet width (past the diameter (D) of the hole due to the expansion of the jet upon exiting the hole). From Figure 4.5, the normalised velocity profile collapses onto one trend for the three blowing ratios tested. This indicates consistent flow behaviour exiting the hole that is not affected by any external factors regardless of the fan speed. Therefore, the streamwise pressure effects on the attachment and detachment of the jet can be tested in isolation.

The calibration of the mean velocity for varying fan speed was accomplished using an orifice flow meter placed 300 mm downstream of the centrifugal fan supplying the secondary air flow as sown in Figure 4.2(a). The ratio between the actual flow rate (pitot tube) and the ideal flow rate (orifice flow meter) is known as the discharge coefficient. The discharge coefficient is used to calibrate the readings obtained by the orifice flow meter to be able to get the actual flow rate obtained at the exit of the hole. This is of particular interest when determining the blowing ratio when the mainstream flow influences the secondary flow velocity. Appendix B provides further explanation on the experimental setup used to calibrate and evaluate the mean velocity of the secondary flow with and without mainstream flow. The discharge coefficient (C_d) was calculated based on the following equation [72]:

$$Q_a = \frac{C_d A_0}{\sqrt{1\text{-}(A_o/A_1)^2}} \sqrt{2g\left(\frac{\Delta P}{\gamma}\right)} \tag{7}$$

Where: C_d is the discharge coefficient, g is the gravitational constant taken as 9.81m/s, ΔP is the change in pressure across the orifice, $P_1 - P_2$, such that the subscript 1 and 2 are upstream and downstream of the orifice respectively, A_0 is the area of the orifice and A_1 is the area upstream of the orifice. The actual flow rate Q_a is the mean velocity determined from the data collected from the pitot tube velocity profile multiplied by the cross-sectional area of the pipe. The mean velocity ($\bar{v}_c$) is calculated using the area wetted average from equation 6 which was simplified for a pipe in respect to the radial position (r), the elemental radial change (dr) and the radius (R) of the channel as follows:

$$\bar{v}_c = \frac{2}{R^2}\sum_{0}^{R} v(r) r dr \tag{8}$$

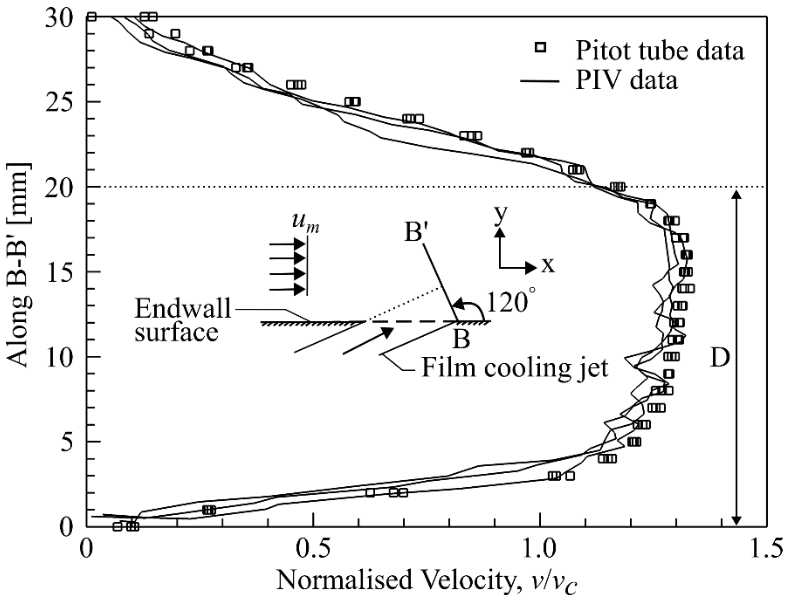

Figure 4.5: Comparisons of film cooling jet (without crossflow for 3 different fan speeds with each corresponding to the blowing ratio of M = 0.5, 1.0 and 1.5)) profiles along B-B’, obtained by both Pitot tube and particle image velocimetry (PIV)

4.4 Flow field mapping and visualisation

4.4.1 Velocity field mapping using Particle Image Velocimetry (PIV)

Flow field measurements were conducted using planar particle image velocimetry (PIV) to capture the jet trajectory, the change in mainstream flow velocity under the influence of streamwise pressure gradients, the critical blowing ratio, the kidney vortex structure, and the lateral spread of the coolant jet downstream of the ejection point. The jet lift-off (attachment and detachment) was analysed using three planes henceforth known as case 1, 2 and 3. Case 1 captured data on the *x-y* plane at $z = 0D$ from $x = -2D$ to $x = 8D$ in the streamwise direction. Case 2 is set in the horizontal *x-z* plane between $x = -2D$ to $x = 4D$ at $y = 2$, 5, 10, 15, 20, 25, 30, 35, 40, and 45 mm. Case 3 relates to PIV data that was transformed to vertical slices from planes at a 45° angle to the *y-z* plane at $x = -2D$, $-1D$, $0D$, $1D$, $2D$, $3D$, $4D$. Code used to transform the plane by 45° is found in Appendix C.

A Dantec Dynamics Dual Power 65-15 laser with a wavelength of 532 nm and a maximum energy output of 80 mJ was used to illuminate the seeding particles introduced into the flow field. The seeding particles were atomized mineral oil (Shell Ondina 901L0996) with a mean diameter of ~1μm. The particles were introduced into the primary flow 2.0 m upstream of the test section and at the inlet of the centrifugal fan supplying the secondary flow. The seeding particles were recirculated through the closed loop wind tunnel configuration to spread the particles evenly across the test section. A single CCD (charge-coupled device) camera (12.125 Hz maximum sampling rate) was used to capture the particle displacement within the 2D illuminated plane. Figure 4.6 shows the positioning of the camera and laser to capture images perpendicular to the laser light sheet. The particles in the observed object plane were mapped onto an image plane captured by the CCD camera. The image resolution was 1296 × 966 pixels with a pixel pitch of 3.75μm. The field of view of the PIV measurement area for case 1 was 210 × 155 mm, and the image magnification factor was M_0 ~0.023. Case 2 and 3 had the same field of view of 100 × 77 mm with an image magnification factor of M_0~0.049. The measurement period encompasses two sequential pulses of the laser light sheet separated by a finite time interval between 10μs and 65μs (calculation shown in Appendix D), defined by the maximum centreline velocity of the secondary airflow at a specific blowing ratio.

For case 1 the laser was fitted with an adapter to direct the emitted laser pulses to a conical mirror placed inside a glass tube casing connected to the laser adapter. Details on the conical mirror and the isotropic illumination for PIV experiments can be found in this paper by Atkins et al. [73]. This method solves the refraction and shadow issue encountered by previous papers in illuminating the test section through a contoured surface placed to induce streamwise pressure gradients. The conical mirror reflected the laser light 90 degrees allowing for illumination across the centre of the test section. The energy output of the laser was set to 30mJ to maximise the number of runs undertaken using a single conical mirror. The camera was positioned perpendicular to the light sheet at 1.5 meters. For case 2 and 3 a Dantec lens was attached to the laser to emit the laser pulses directly into the test section horizontally, for case 2, and at a 45° angle for case 3. The cameras were positioned perpendicular to the light sheet at 0.9 meters.

Each run captured 200 images (with an elapsed time of ~20 seconds) that were post processed to obtain the flow field vector map using PIV software (Dantec Dynamic Studio V8). The vector field between two successive image frames produced an instantaneous vector map that were sub-dived into regions known as interrogation areas of 16 × 16 pixels in size with an overlap of 50%. The interrogation size is selected with roughly 6-7 pairs of particles present within the interrogation area to reduce the uncertainty of the PIV vector maps. For a specific location in the flow field, the time-averaged velocity field is evaluated over a group of 200 instantaneous vector maps sampled at a frequency of 12 Hz. A minimum pixel image was obtained from the retrieved images and subtracted from the raw images to reduce any potential background noise. An image mask was applied to the arithmetic images to subtract regions without flow, the bottom wall and contour of the upper wall specifically for the favourable pressure gradient. An average correlation image was obtained from the arithmetic images. Peak validation, range validation, moving average validation, and an average filter were applied to the average correlation image (time-averaged velocity field) to reduce spurious vectors. For each set of images obtained the spatial resolution of the velocity vector map containing 161 × 112 vectors was a vector spacing of ~ 0.6 mm.

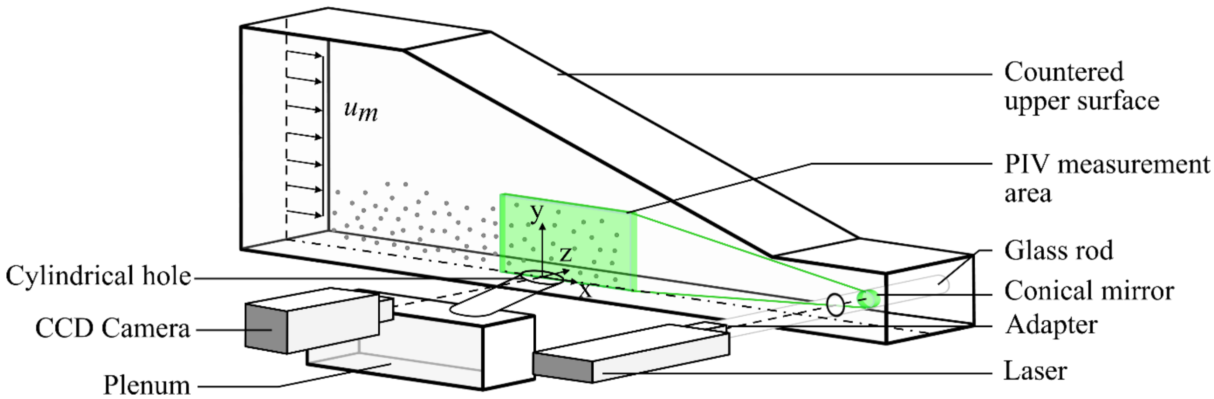

(a)

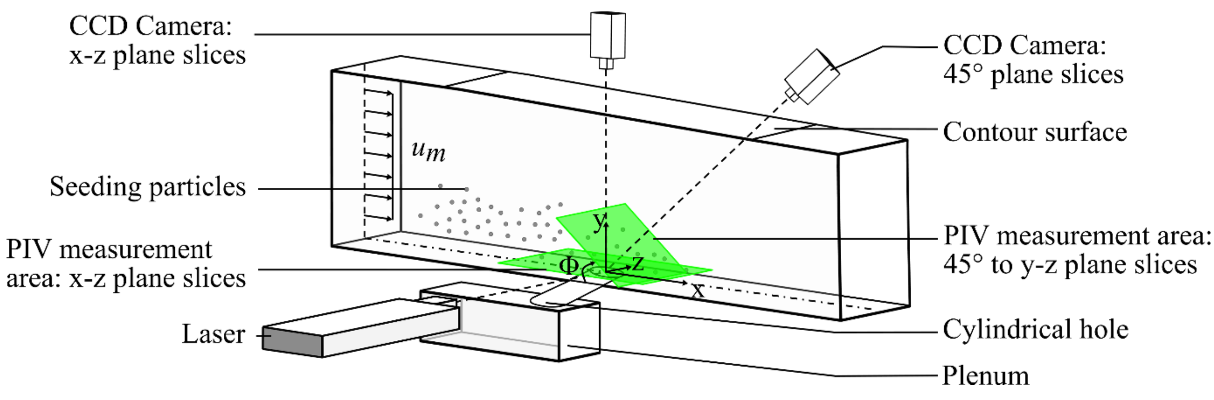

(b)

Figure 4.6: Schematic of the camera and laser positioning to obtain a PIV measurement area. (a) On the *x-y* plane at z = 0 mm (Case 1) and (b) On the *x-z* plane at y = 2 mm, 5 mm, 10 mm, 15 mm, 20 mm, 25 mm, 30 mm, 35 mm and 40 mm, and at a 45° angle to the *y-z* plane at x = -2D, -1D, 0D, 1D, 2D, 3D, 4D with the film cooling jet diameter of D = 20 mm (Cases 2 & 3)

4.4.2 Flow field visualisation using Planar Laser Visualisation (PLV)

Planar laser visualisation is a flow visualisation technique that incorporates the use of a laser to illuminate seeding particles across a thin plane. This technique uses the same system as that used for the particle image velocimetry technique (a Dantec Dynamics Dual Power 65-15 laser and a CCD camera with 12.125 Hz maximum sampling rate). However, only seeding particles (Shell Ondina 901L0996 with a mean diameter of ~1μm) are introduced into the "targeted" flow for visualisation. Incorporating seeding particles only into the "targeted" allows for a clear contrast between the flow structures (illuminated particles) and the mainstream flow (black background due to lack of particles reflecting light). To this end, the atomised mineral oil particles were introduced only into the film cooling jet. The laser light sheet illuminated the particles carried by the jet in the vertical *x-y* plane, and the high contrast between the mainstream and the film cooling provides insight of the extent of attachment or detachment of the jet flow to the endwall surface, and the details of how the jet interacts with the endwall.

The distinction between the PLV and PIV images gathered is in the concentration of particles. Where for PLV only the particles are shown in the coolant jet (analysed flow structure) compared to the homogenously seeded image used for PIV that requires more particles to resolve the velocity components of the full tested area.

4.4.3 Endwall visualisation using a florescent oil-dye mixture technique

Endwall surface flow pattern was visualized using an oil-dye mixture technique. Florescent powder was mixed with a light diesel fuel, and the mixture was then applied to the endwall surface using a brush to achieve targeted even distribution upstream, downstream, and around the ejection hole. The aerodynamic shear stresses, at the endwall, redistributed the mixture and visualization of the surface flow patterns was realized. This pattern represented a time-averaged visualization of the endwall flow topologies. Validation and interpretation of such topologies has been independently validated against near endwall PIV measurements in a previous study by Schekman et al. [74].

Before the application of the mixture, the surface was painted in black to enhance the reflectivity and contrast between the endwall and dye patterns. An ultraviolet (UV) light illuminated the surface flow pattern while it was being photographed. Further the experiment was run for a sufficient length of time to allow for at least a partial evaporation of the diesel. This allowed for the patterns to be imaged with the wind tunnel turned off without the disturbed diesel mixture flowing back over the patterns, disrupting the image. If, however, large pooling of oil-dye occurred then disruption could only be at best minimised. More details associated with this flow visualization technique can be found in Kim et al. [75].

4.5 Uncertainty analysis

This study considers a steady state system which over time has variations in the repetition of tests conducted. These errors or uncertainties are random errors as they vary between tests. Although the total error is defined as the sum of the systematic and random errors, the bias from the true value, the systematic error, was reduced based on calibration of the experimental apparatus by comparison between data sets such as the pitot tube, and the orifice flow meter. The uncertainty associated with the random errors or random uncertainty as defined in Colman and Steele [70], is calculated based on the standard sample deviation of the individual values of the tests from the mean sample value. To obtain a random uncertainty with a confidence interval of 95% (indicating the probability that a particular test value falls within this range 95% of the time) is defined based on a t critical value from a t-distribution graph as follows [70]:

$$P_{X_{mean}} = \frac{tS_N}{\sqrt{N}} \tag{9}$$

Where: N is the sample population (i.e. the number of individual readings), S_N is the sample standard deviation, and the critical t value is obtained from Appendix E and is based on the degrees of freedom ($v = N - 1$) and the sample population (N).

For this study, the blowing ratio is a function of the mean mainstream and coolant velocities which are both a function of the local velocity which in turn is a function of the pressure difference through the pitot tube and orifice flow meter. The uncertainty associated with the local velocity, flow rate through the flow meter and blowing ratio was 1% 1.8%, and 1% respectively determined based on 20:1 odds (95% confidence) method outlined by Coleman and Steele [70]. This considers the uncertainty based on random errors and not the systematic (bias) errors which were minimised through calibration.

The uncertainty associated with the PIV vector maps is based on the displacement between individual pairs of particles tracked within an interrogation window between exposure frames 1 and 2 according to a parent vector map that has not been modified, i.e. the cross-correlation map [76], [77]. In this method the systematic uncertainty regarding alignment of laser plane and camera, timing and synchronisation of laser and camera capture, particle tracing capabilities (particle slip velocity, i.e.

particle velocity relative to flow velocity), image peak-locking (particle size relative to pixel size) and illumination of laser (dual laser sheet pulse alignment and intensity) are accounted for during calibration and experimental setup and as such are not considered as significant sources of error. Therefore, only the random errors in the particle disparity method developed by Sciacchitano et al. [77], [78] and conducted using the PIV software (Dantec Dynamic Studio V8) are accounted for [78]. This includes the effects of particle image displacement, out-of-illuminated-plane motion, seeding density and particle image diameter [77]. Although the 'exact' velocity measurement is not known, this method applies an algorithm that performs image-matching estimations to produce an instantaneous distribution of the uncertainty measurement of the velocity vector field [77]. The particle disparity uncertainty accounting for a particle size of 2-3 pixels with an interrogation window of 16 × 16 pixels is ~0.2 pixel units and ~0.4 pixel units in the freestream and jet respectively. Therefore, the full-scale relative measurement error is ~1.6% and ~3.3% in the freestream and jet respectively.

4.6 Validation of the blowing ratio

The blowing ratio was validated through comparison of the pitot tube and PIV data obtained through various tests. The difference between pitot tube and PIV data points shown in Figure 4.4 and Figure 4.5 obtained for the mainstream velocity profile and secondary flow velocity profiles was ≤ 8.2%, and ≤ 6.8% respectively. The calculated mean velocity for both the pitot tube and extracted PIV data for the mainstream and secondary velocity profile was ≤ 1% for both cases. The process to determine the blowing ratio, knowing that the pitot tube and PIV data were closely matched followed the detailed calibration setup procedure that can be found in Appendix B.

4.7 Channel wall effects

The wall effects on the jet flow associated with the development of the boundary layer through the channel consisting of a 100.0 mm width was tested to determine whether there was any significant influence on the jet profile. Cross-width channel velocity profiles were extracted for a width of (1) 100.0 mm, and (2) 320.0 mm (the maximum channel width). Both tests were conducted with a constant channel height of 250.0 mm. The variation in channel height to obtain the required pressure gradient through the channel posed an issue on the limits of the experimental facilities available. This is the case as an increase in fan speed would be required to maintain the required flow rate through the channel for the most favourable pressure gradient setup. A channel width of 100.0 mm and a hole diameter of 20.0 mm were selected to best utilise the experimental apparatus without exceeding the rated fan speed limits of operation. A comparison of the velocity profiles through the channel width are shown in Figure 4.7 for varying blowing ratios of $M = 0.5$, $M = 1.0$, and $M = 1.5$.

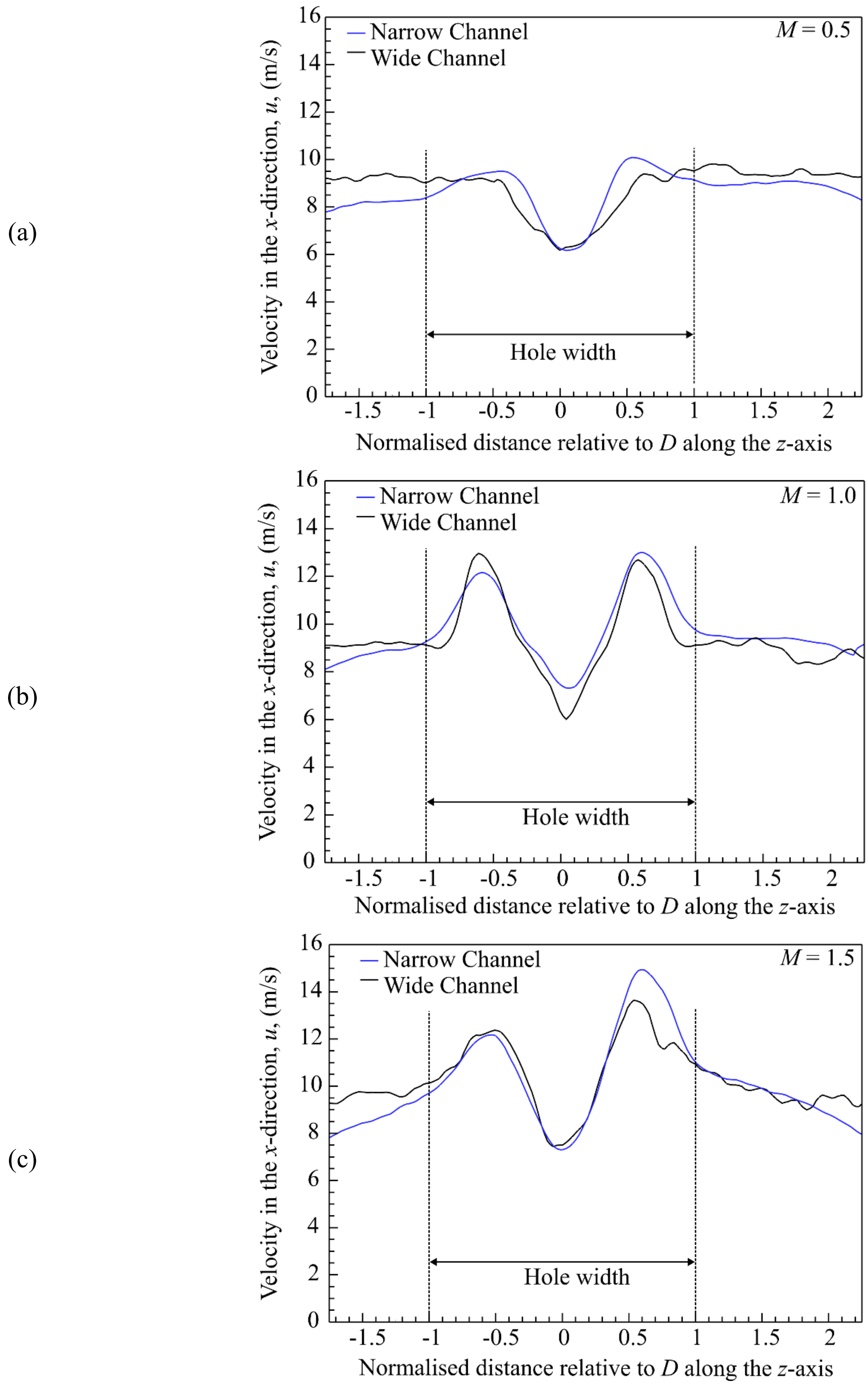

Figure 4.7: Comparison of the transverse PIV velocity profiles through a zero-pressure gradient channel on the x-z plane at $y/D = 0.5$ and $x/D = 3$ for (a) $M = 0.5$, (b) $M = 1.0$, and (c) $M = 1.5$

The x-direction (u-velocity component) of the resultant mainstream and secondary flow velocity is observed in Figure 4.7. At the centre of the jet the velocity profiles between the wide channel and narrow channel are closely matched and follow a similar trend. The width of the jet is also similar in size.

Beyond the jet, the mainstream velocity profile varies as the boundary layer of the wall causes the mainstream flow to decrease towards the wall as expected. However, the boundary layer flow does not influence the jet flow as the velocity of the jet is closely matched in magnitude over the hole width for the narrow 100.0 mm width and wider 320.0 mm channel widths.

5 Results and Discussion

In this study, an experimental investigation was performed to evaluate mainstream-jet-endwall interaction when the streamwise pressure gradient and the blowing ratio was varied. In particular, using the PIV technique the structure of the jet kidney vortex was revealed, and it was shown how the pressure gradient and blowing ratio affects the attachment of the jet to the endwall. In addition, endwall oil dye flow visualization demonstrated in detail how the kidney vortex jet structure interacts with the endwall surface. These results are described further in the following sections.

5.1 Film cooling jet in differing blowing ratios under a zero-pressure gradient (ZPG)

The film cooling jet interacting with crossflow (mainstream) is shown in Figure 5.1, whereby PIV measurements were obtained in a symmetric plane under the zero-pressure gradient (ZPG) at three selected blowing ratios: $M = 1.5$, 1.0 and 0.5. Figure 5.1(a) shows the high blowing ratio (e.g., $M = 1.5$) and that the film cooling jet is detached from the endwall after being ejected into the mainstream, which is clearly seen from the flow visualization (i) and the velocity contours in the *x-y* plane (ii). Specifically, the detached region is revealed from the flow visualization (i) by the dark region between the jet flow and endwall surface caused by the low concentration of seeding particles. The jet remains detached up to $x/D = 3.0$ which is the downstream extent of the measured flow field using PIV. In addition, both upper and lower peripheries of the film cooling jet in the symmetry *x-y* plane run almost parallel to the jet axis, which indicates limited radial diffusion of the jet and there is almost no apparent arching of the jet core as the jet is convected downstream. The absolute velocity $|V|$ contour of the jet in the symmetry plane by Figure 5.1 (a, ii) shows that the incoming boundary layer mainstream flow retards approaching the inclined column of the film cooling jet and follows the jet's leading-edge as if the jet's column is a solid backward inclined circular object [79]. Along the jet axis, the core velocity appears to remain unchanged roughly until $s/D \sim 2.0$ from the jet exit indicated.

The velocity field mapped by PIV in the *x-y* and *y-z* planes (iii & iv) shows the structure of the kidney vortex as of a pair of counter-rotating vortices that develop in the streamwise direction. Here, two localised regions of increased flow velocity at the core of each kidney vortex can also be discerned in the *x-y* plane at $y/D = 0.5$ in (iii). From Figure 5.1(a, iv) the location of the kidney vortex cores relative to the endwall and lateral spreading (in the *z*-axis direction) are determined with the PIV measurements that are decomposed as *y-z* plane vertical slices made at three x/D positions. As the jet is convected downstream the distance between the core of each vortex in the *z*-axis (z_1) remains largely constant. On the other hand, the height of the vortex cores above the endwall (y_1) increases as seen in Figure 5.1(a, iv). The distance y_1 is largely similar to the height of the jet core in the *x-y* plane. As the x/D distance increases, a region of low-velocity flow downstream of the film cooling hole is created as seen in Figure 5.1(a, ii & iii). This is coupled with the circulation of the vortices and causes entrainment of the mainstream flow towards the centre of the jet [7], [15]. This drives the outer boundary jet flow towards the centre and results in a net upwards force on the jet [10]. As the jet convects downstream, the jet lift-off distance y_1 monotonically increases since the jet is detached as shown in Figure 5.2.

(a)

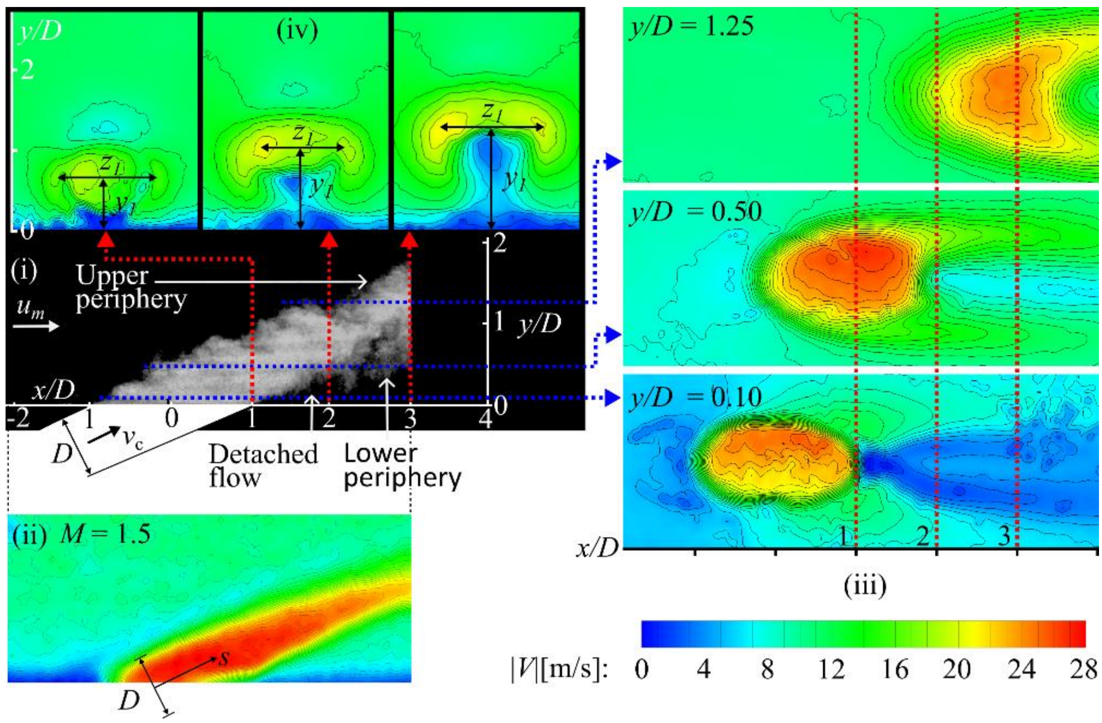

(b)

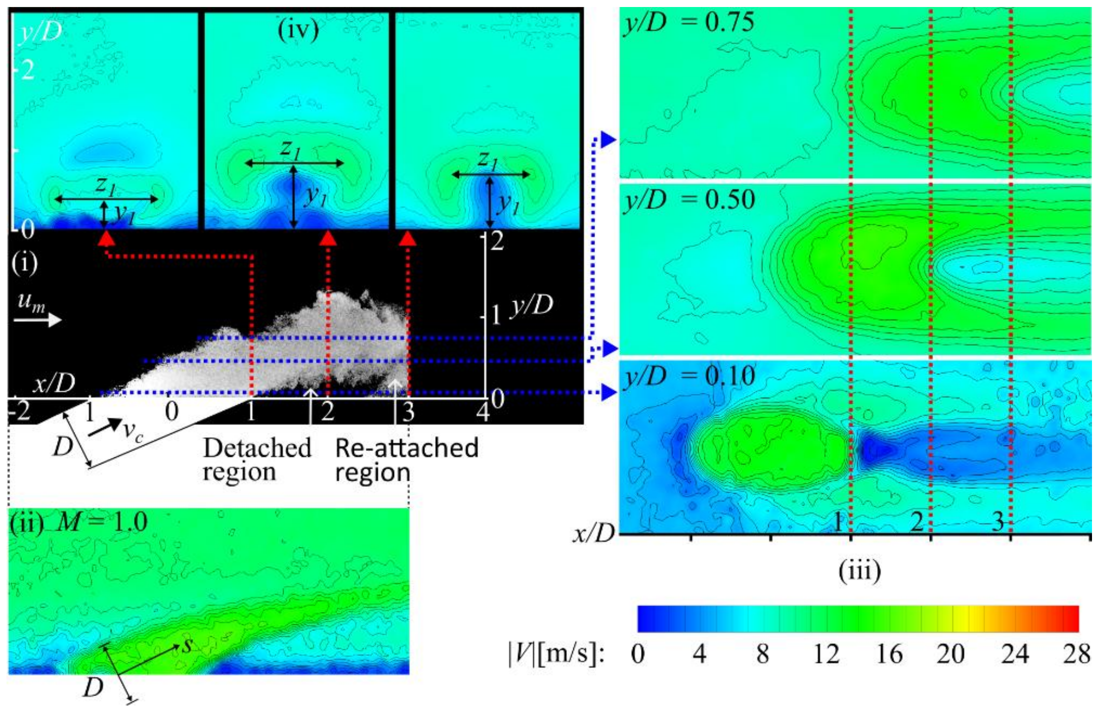

(c)

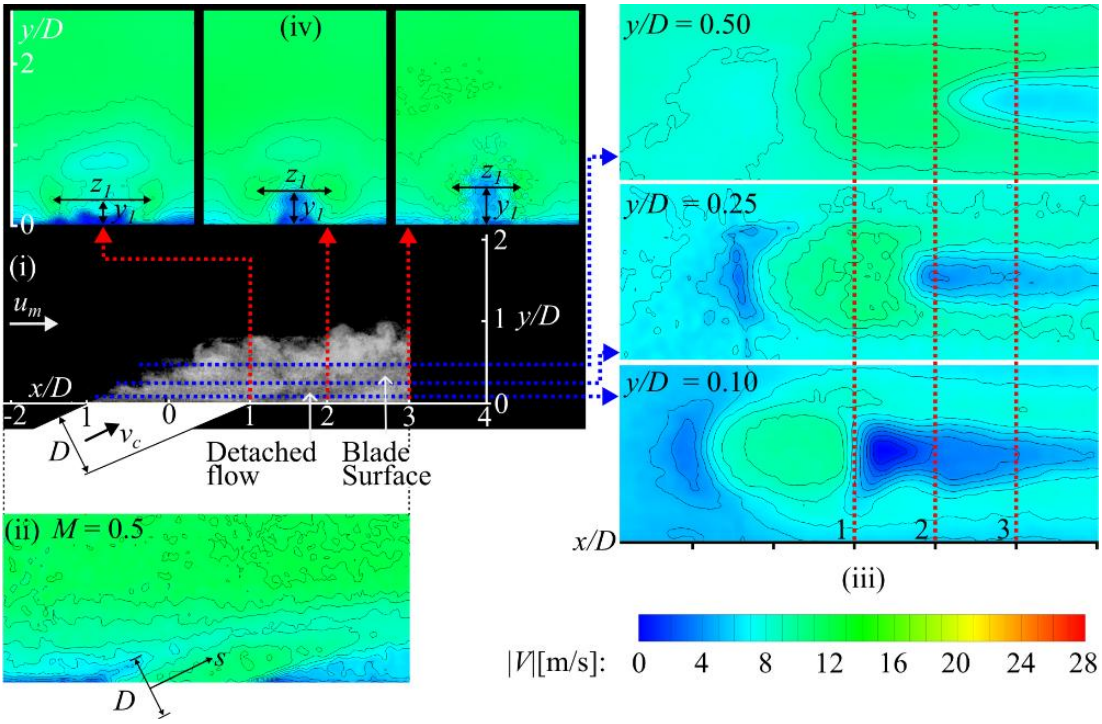

Figure 5.1: Film cooling jet structure including Kidney vortex in crossflow under ZPG while varying M for Re_D= 1.4×10^4 (u_m ~ 11.5 m/s). (a) At M = 1.5 (detached flow), (b) At M = 1.0 (semi-detached flow), (c) At M = 0.5 (attached flow).

Figure 5.1(b) reveals the jets behaviour when the blowing ratio decreased to M = 1. Here the film cooling jet's momentum flux matches that of the mainstream, and similar to M = 1.5, a detached region is apparent (i.e., dark region) downstream of the jet exit Figure 5.1(b, i). However, in contrast to Figure 5.1(a), distinct arching of the jet core towards the endwall occurs (see Figure 5.1(b, i & ii)). Roughly at $x/D \approx 2.8$ from the ejection hole axis, the lower periphery of the jet shear layer re-attaches to the endwall surface (see Figure 5.1(b, i). The velocity contours in Figure 5.1(b, ii), show that the core of the jet moves away from the endwall, however with increased arching compared with Figure 5.1(a, i & ii)). Three horizontally (x-z plane) slices with varying elevation from the blade surface in Figure 5.1(b, iii) show similar structures to the blowing ratio M = 1.5 case but with lowered jet velocity values. Here, interaction of the mainstream with the jet is clearly shown where significant flow deceleration in the immediate upstream region of the jet occurs, to demonstrate that the inclined jet acts to partially obstruct the mainstream (i.e., y/D = 0.1). The velocity contours in the y-z plane (see Figure 5.1(b, iv)) show upward entrainment of the flow at the centreline by the kidney vortices. In addition, Figure 5.1(b, iv) shows the centre-to-centre distance (z_1) between the cores of the counter-rotating vortices, which for the semi-detached flow, decreases after attachment at about x/D = 3.0. Furthermore, the detached distance from the endwall surface, y_1 of the re-attached film cooling jet decreased. The jet core, including kidney vortices, is thus convected towards the endwall while diminishing in size compared to the case with M = 1.5 (see Figure 5.1(a)). The flow visualization in Figure 5.1(b, i) has the entire jet for -1 ≤ x/D ≤ 3 visualized and highlights that the jet attachment does not necessarily occur at an instantaneous point downstream for the entire jet. This jet flow is termed as "semi-detached" with a region downstream of the jet exit where no portion of the jet flow interacts with the endwall. Here the classification of semi-detached flow is defined since the ejected cooling jet is detached at the exit and then reattaches to the endwall surface at a close downstream location (i.e., ~3D). Previous research defined the location of the reattachment jet in conjunction with the placement of the film cooling holes array on a turbine blade surface. Here, the positioning of film cooling holes along a turbine blade surface has been optimised to increase the coolant coverage to maximise the FCE. These positions vary substantially between individual designs. The coolant ejection through upstream film cooling holes is typically designed to re-attach within the spacing between rows of film cooling holes and the respective spacings presented in previous papers over a turbine blade are: ~4D measured from the hole centre on the blade pressure surface (PS) and ~12D on the suction surface (SS) by Gao et al. [31], ~3D, ~5D and ~9D on the PS and ~12D on the SS by Narzary et al. [33], ~3D and ~12D on the PS by Lee et al. [80], ~6D on the SS and ~2D to ~10D on the PS by Zhang et al. [2]), and ~5D on the PS and SS by Ames et al. [81]. More relevant to the present study over flat endwall surfaces, the hole spacings are: ~3D by Jessen et al. [16], ~3D by Jabbari et al. [82], 10D by Hay et al. [83], 5D and 10D by Jubran et al. [84], ~2D by Maiteh et al.[85], and 3D by Kingery et al. [86]. Consequently, the reattachment length of the cooling jet to the endwall surface adopted in this study is 3D downstream of the coolant ejection hole.

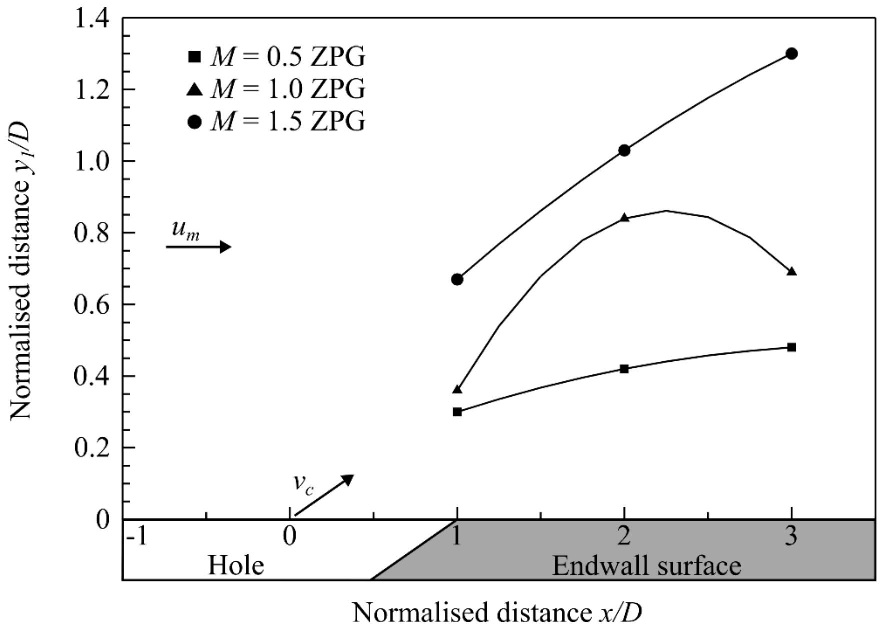

Figure 5.2: Normalised distance y_1/D for a zero pressure gradient (ZPG) at x/D = 1, 2, and 3 with blowing ratios of M = 0.5, 1.0, and 1.5

When the blowing ratio is reduced further to M = 0.5 (Figure 5.1(c)), the film cooling jet velocity is half of the mainstream. Figure 5.1(c, i) shows that immediately after the jet exits, a portion of the jet is seen to be attached to the endwall, and a very low velocity downstream of the exit is observed in Figure 5.1(c, ii & iii). The height of the vortex cores, y_1, increases slightly but remains low for all three cases considered as seen in Figure 5.1(c, iv) and Figure 5.2. The centre-to-centre distance of the two counter-rotating vortices, z_1, decreases monotonically after exit while convecting downstream. Overall, the lateral coverage of the film cooling jet is reduced in comparison to the case with $M = 1.0$.

In summary, increasing the blowing ratio of the film cooling jet ($M = 0.5 \rightarrow 1.0 \rightarrow 1.5$) sequentially causes the jet and endwall to interact as: (i) attached, (ii) semi-detached, (iii) detached flows for the zero-pressure gradient (ZPG) condition. Furthermore, the kidney vortex formed resulting from the interaction between the mainstream and the film cooling jet becomes stronger, which implies the stronger mixing between the mainstream and jet stream.

5.2 Endwall flows with differing blowing ratios under a zero-pressure gradient (ZPG)

Figure 5.1(a) shows that the jet is detached from the endwall with the higher blowing ratio $M = 1.5$, and a region of low velocity downstream of the jet exit developed at $z/D = 0.0$ in both the *x-y* plane (ii) and *x-z* plane for $y/D = 0.1$ (iii). As the blowing ratio decreased jet attachment was observed, yet the low momentum region near the jet exit persisted [67], [86]. To further understand the coverage of the cooling jet over the endwall surface near the jet exit region, and the specific characteristics of detached and attached jet flow, an endwall oil-dye visualization technique was performed. This experimental method qualitatively reveals the distribution of the endwall shear stresses around and downstream of the jet exit to highlight details of the mainstream-jet-endwall interaction [87]. Figure 5.3 shows the resolved flow fields for attached (a), semi-detached (b) and detached (c) jet flow cases corresponding to the test conditions in Figure 5.1. Three distinct wake regions (i.e., I, II & III) were schematically illustrated and described in detail in the following section.

Wake Region I is shown in Figure 5.3(a) and occurs immediately downstream of the jet exit, where oil pooling near the exit of the jet is seen. The pooling results from high mainstream entrainment (i.e., high oil-dye concentration) and strong recirculation near the jet exit (see Figure 5.3(f)) so that the fluid is not able to be convected downstream. In particular, the Wake Region I appears to be fed by (i) the mainstream flow wrapping around the jet flow at the exit and (ii) the horseshoe vortex system originating at the separation line (see Figure 5.3(d and e)). As the mainstream endwall flow approaches the jet flow, an adverse pressure gradient upstream of the jet develops that is associated with the reduced mainstream velocity upstream of the jet (see Figure 5.1). Consequently, separation and roll-up of the boundary layer into a horseshoe vortex structure takes place [87]. Flow separation is identified by the well-known separation line that develops in the oil dye pattern around the jet that is seen in Figure 5.3(e) for the semi-detached case. This present interpretation of the separation line and horseshoe vortex structure development is based on previous flow visualization studies [75], [88], [89]. Here, it appears that the horseshoe vortices wrap around the jet structure and become entrained into Wake Region I where oil dye pooling is seen. The entrained region has a complex flow structure featuring a pair of irregular shaped vortices as seen in Figure 5.3(f).

For a horseshoe vortex structure around a solid inclined cylinder, the surrounding flow converges at the centreline of the wake, i.e. z/D = 0.0, forming a single trailing wake stream [88]. In contrast, for the current case the jet flow obstructs the mainstream and a split wake develops. The split is initiated by a teardrop shaped region denoted as Wake Region II. This region is indicated in Figure 5.3(f) and can be seen for all three cases in Figure 5.3(a, b, and c). After converging and forming the tail of the tear drop, Wake Region II persists downstream as a narrow band of dye. The flow from Wake Region I then wraps around Wake Region II and forms a pair of distinct dark bands (denoted as Wake Region III) that extend downstream in the streamwise direction. The distinction between Wake Region I and III occurs at the start of Wake Region II (i.e., at $x/D \approx 1.5$). The absence of dye particles in Wake Region III indicates a larger endwall shear stress that disperses the dye particles quickly before they are deposited on the endwall [75], [88].

Figure 5.3(a, b, and c) shows the variation of the wake region (i.e., I, II, III) endwall pattern with blowing ratio under the zero pressure gradient condition. Wake Region I remains fixed with a change in blowing ratio. The blowing ratio does not substantially affect the formation of the horse vortex system and in turn Wake Region I since the horseshoe vortices are entrained within the wake at the exit of the jet. Wake Region II is unchanged with the varying blowing ratio, where the tear drop shape is initiated and terminated at approximately the same downstream position for all three blowing ratios ($x/D \approx 1.5$ and $x/D \approx 3.0$ respectively).

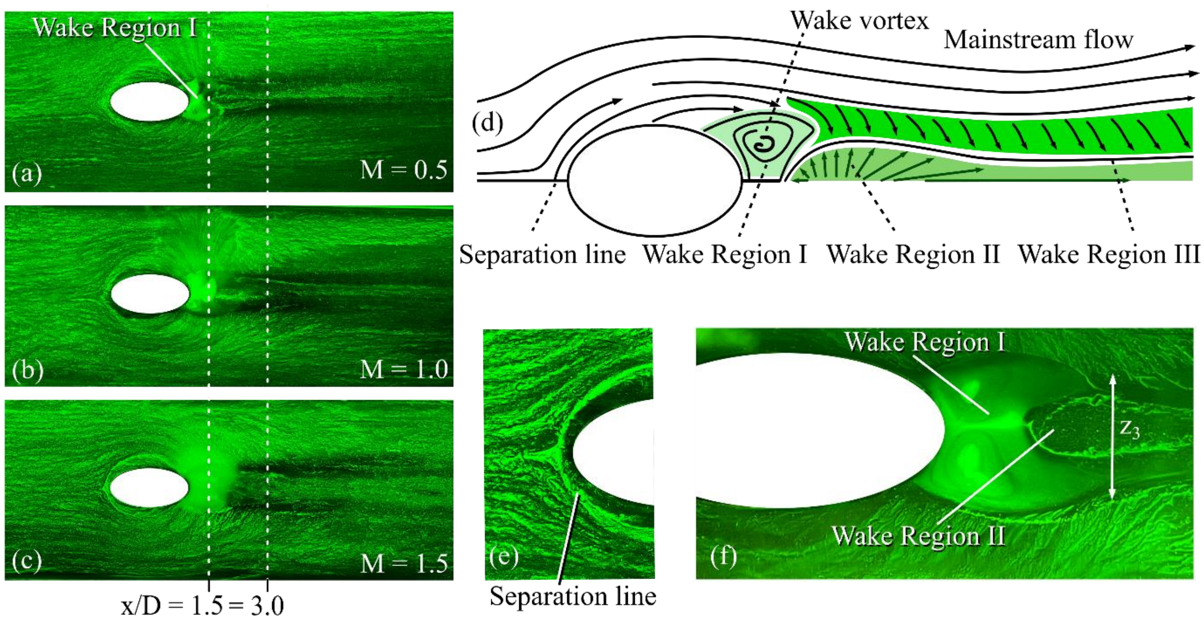

Figure 5.3: Endwall oil-dye flow visualisation for ZPG while varying M for $Re_D = 1.4\times10^4$ (u_m = 11.5 m/s). (a) Attached jet flow, M = 0.5 (b) Semi-detached flow, M = 1.0 (c) Detached flow, M = 1.5 (d) Flow topology schematic, (e) Closeup of upstream region for semi-detached case and (f) closeup of downstream wake region for semi-detached case.

In contrast, Wake Region III varies distinctly across Figure 5.3(a, b, and c), with increasing blowing ratio. Here the Wake Region III width is seen to decrease and form a waist at x/D = 3.0 (i.e., narrowest section of the wake). For the detached jet case (Figure 5.3(c)) the region contracts slightly but following the termination of Wake Region II, Wake Region III begins to diverge. For the attached jet case, where M = 0.5 (Figure 5.3(a)) Wake Region III is at the narrowest. This behaviour can be correlated to the PIV velocity contours in the y-z plane Figure 5.1. Specifically, the lateral distance between the kidney vortex core z_1 decreases as the blowing ratio is reduces, that follows a similar trend to the Wake region III waist width that gets progressively smaller as shown in Figure 5.4. For the detached case (Figure 5.1(a, iii)), z_1 remains approximately constant while for the attached case (Figure 5.1(c, iii)) z_1 decreases drastically by x/D = 3.0. This would indicate that Wake Region III is related to the formation of the kidney vortices in the jet flow and that the mainstream-jet flow interaction affects the endwall flow pattern via the kidney vortex. In addition, Figure 5.4 demonstrates that the blowing ratio has a substantial effect on the lateral spreading of the cooling jet that ultimately influences the coverage of the jet on the endwall surface. With increased blowing ratio under the cooling jet spreads laterally, and detaches from the endwall surface, under the zero-pressure gradient condition.

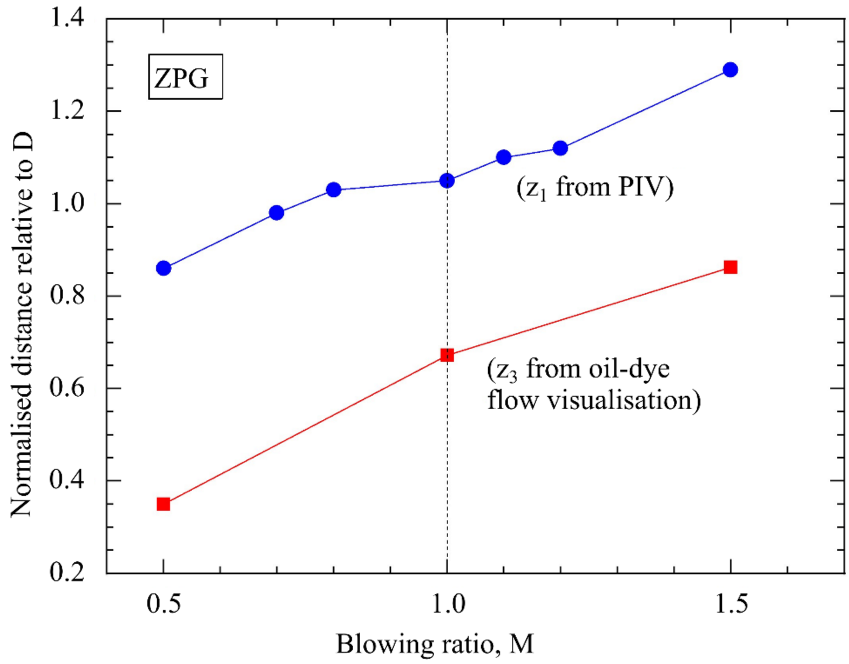

Figure 5.4: Comparison of the PIV velocity data for the lateral spreading distance (z_1) of the kidney vortex, and oil dye visualization endwall wake width (z_3) at the $x/D = 3$ for the zero-pressure gradient condition.

5.3 Film cooling jet in crossflow under differing pressure gradients

The effect of a streamwise pressure gradient on the film cooling jet's attachment, detachment and endwall coverage at a fixed blowing ratio ($M = 1.0$) is considered. The laser planar flow visualisation and PIV velocity contours are shown in Figure 5.5 for cases: (a) with a zero-pressure gradient (ZPG, $K = 0.0$), (b) mild adverse pressure gradient (MAPG, $K = (-)0.3\times10^{-6}$), (c) mild favourable pressure gradient (MFPG, $K = 1.5\times10^{-6}$) and (d) favourable pressure gradient (FPG, $K = 2.6\times10^{-6}$). For a zero-pressure gradient (ZPG) as a reference, the jet flow was seen in Figure 5.1(b) to initially detach and then reattach to the endwall at approximately at $x/D \approx 2.8$. At $x/D = 3.0$ the jet core is at $y/D \approx 0.7$, which is similar to the height of the kidney vortices above the endwall surface (i.e. $y_1 \approx 0.7$) as shown in Figure 5.1(b, iv).

The flow field for the mild adverse pressure gradient (MAPG) is shown in Figure 5.5(b), where the film cooling jet is detached from the endwall surface in contrast to the ZPG case in Figure 5.1(b, i) or Figure 5.5(a). In addition, the jet core is higher at $y/D \approx y_1 \approx 0.9$ at the $x/D = 3.0$ location. Thus, the kidney vortices for the adverse pressure gradient case moves further away from the endwall and the flow visualization shows that the mainstream flow (black region) is directed towards the endwall. With a mild favourable pressure gradient (MFPG) (Figure 5.5(c)) the laser planar visualization of the jet flow reveals slight detachment of the jet from the endwall surface, which is less than the MAPG seen in Figure 5.5(b). The velocity contours also indicate that the jet core height at $x/D = 3.0$ decreases between a zero-pressure gradient (Figure 5.5(a)) to the mild favourable pressure gradient (Figure 5.5(c)), and thus a slightly lower kidney vortex height (y_1) is expected for this case. Flow visualization and PIV velocity measurements of the favourable pressure gradient (FPG) case is shown in Figure 5.5(d) which indicates complete attachment of the jet flow to the endwall surface. Additionally, based on the velocity contours the height of the jet core is substantially lower at $y/D \approx y_1 \approx 0.45$ at the $x/D = 3$ location.

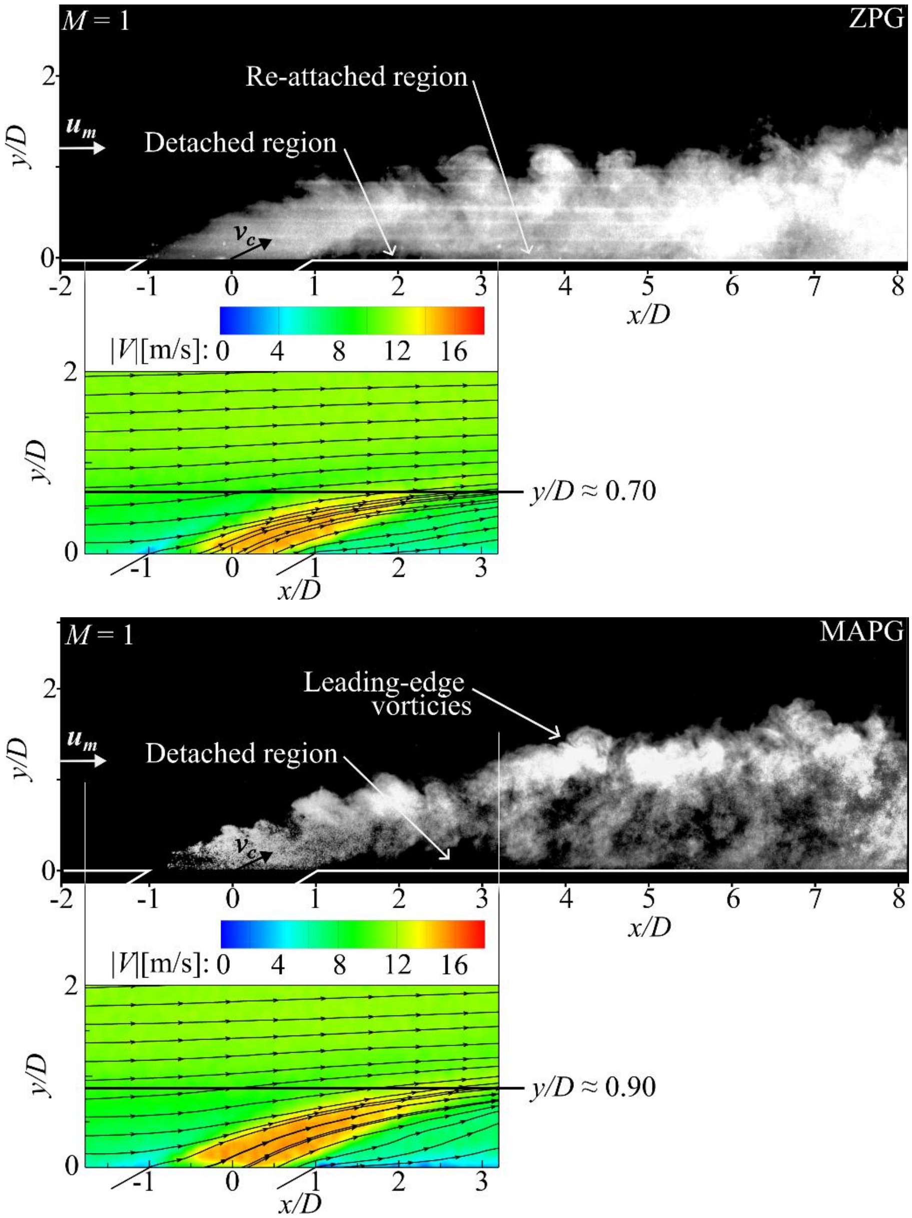

(a)

(b)

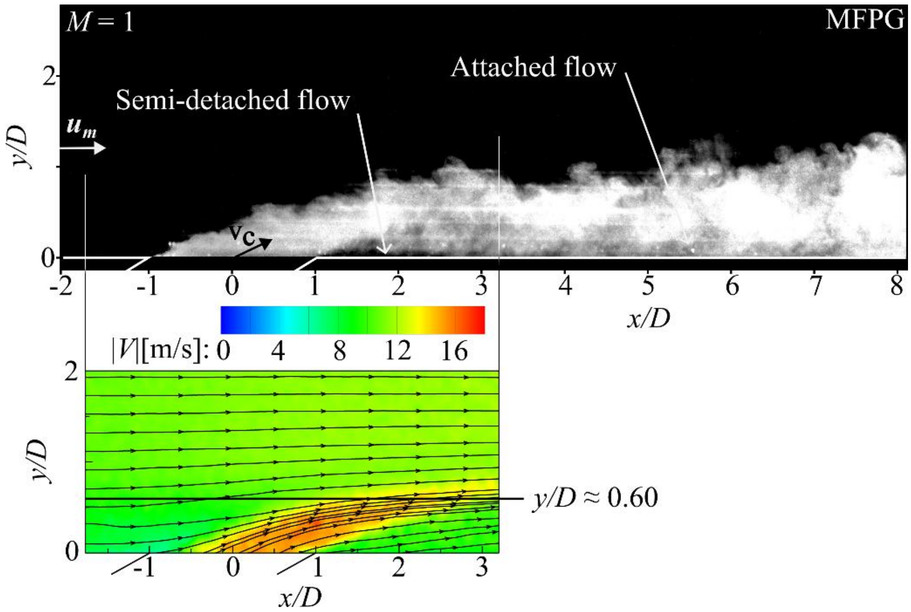

(c)

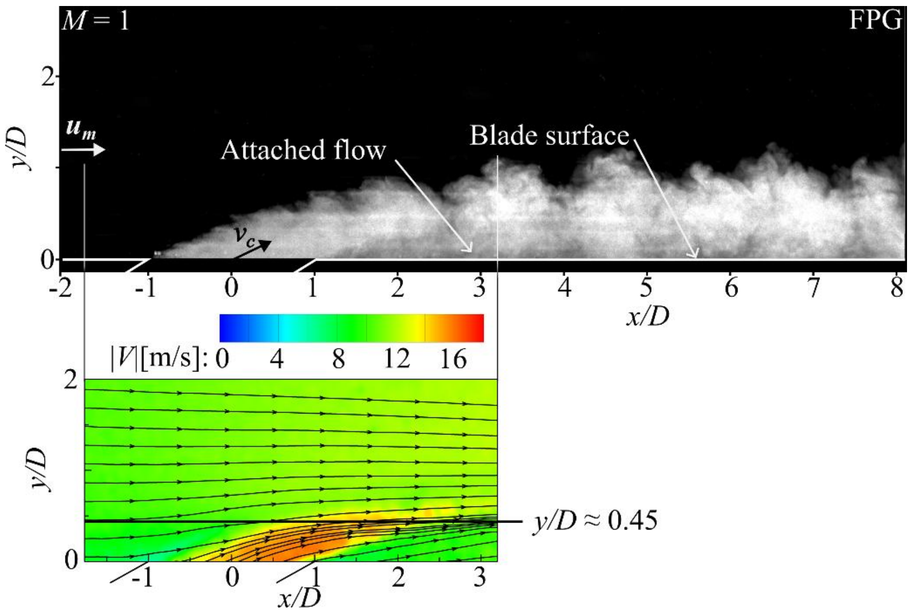

(d)

Figure 5.5: Film cooling jet interacting with the mainstream in a symmetry plane at M = 1.0 while varying a pressure gradient (a) for a mild adverse pressure gradient (MAPG): detached flow, (b) for a zero-pressure gradient (ZPG): semi-detached flow, (c) for a mild favourable pressure gradient (MFPG): semi-detached flow, (d) for a favourable pressure gradient (FPG): attached flow.

Fluorescent oil-dye endwall flow visualisation is shown in Figure 5.6(a, b, c, and d) for the favourable, mild favourable, zero, and mild adverse pressure gradients respectively at a constant blowing ratio of M = 1.0. In all four cases, the flow diverts around the coolant jet hole where a separation point is seen as explained in Figure 5.3(e). The location of the separation point upstream does not vary by a significant degree between all four cases. This is explained by the calibration of the mainstream flow taken at the centre of the hole by x/D = 0 where the velocity was calibrated to be u_m = 11.5 m/s for an engine representative number of Re_D= 1.4×10^4. Downstream of the ejection point the effects of the imposed streamwise pressure gradient are observed. Between x/D = 1.0 and x/D = 3.0, a small, blurred region is observed in Figure 5.6. This is observed to distort the image at Wake Region I and Wake Region II as describe in Figure 5.3(d and f). These images shown in Figure 5.6 are raw images and as such the slight interference of the oil prior to complete evaporation is shown. Full evaporation of the oil was not necessary as the endwall flow features are adequately visible for the comparative analysis between all four pressure gradient cases. Wake Region I and Wake Region II is seen to increase slightly with a decrease in the acceleration parameter (K) as the flow decelerates, i.e. from $K = 2.6\times10^{-6}$ (FPG), to $K = 1.5\times10^{-6}$ (MFPG), to K = 0.0 (ZPG), and to $K = (-)0.3\times10^{-6}$ (MAPG). Wake Region I is seen to extend between $x/D \approx 1.5$ to $x/D \approx 2.0$ from the FPG to MAPG respectively.

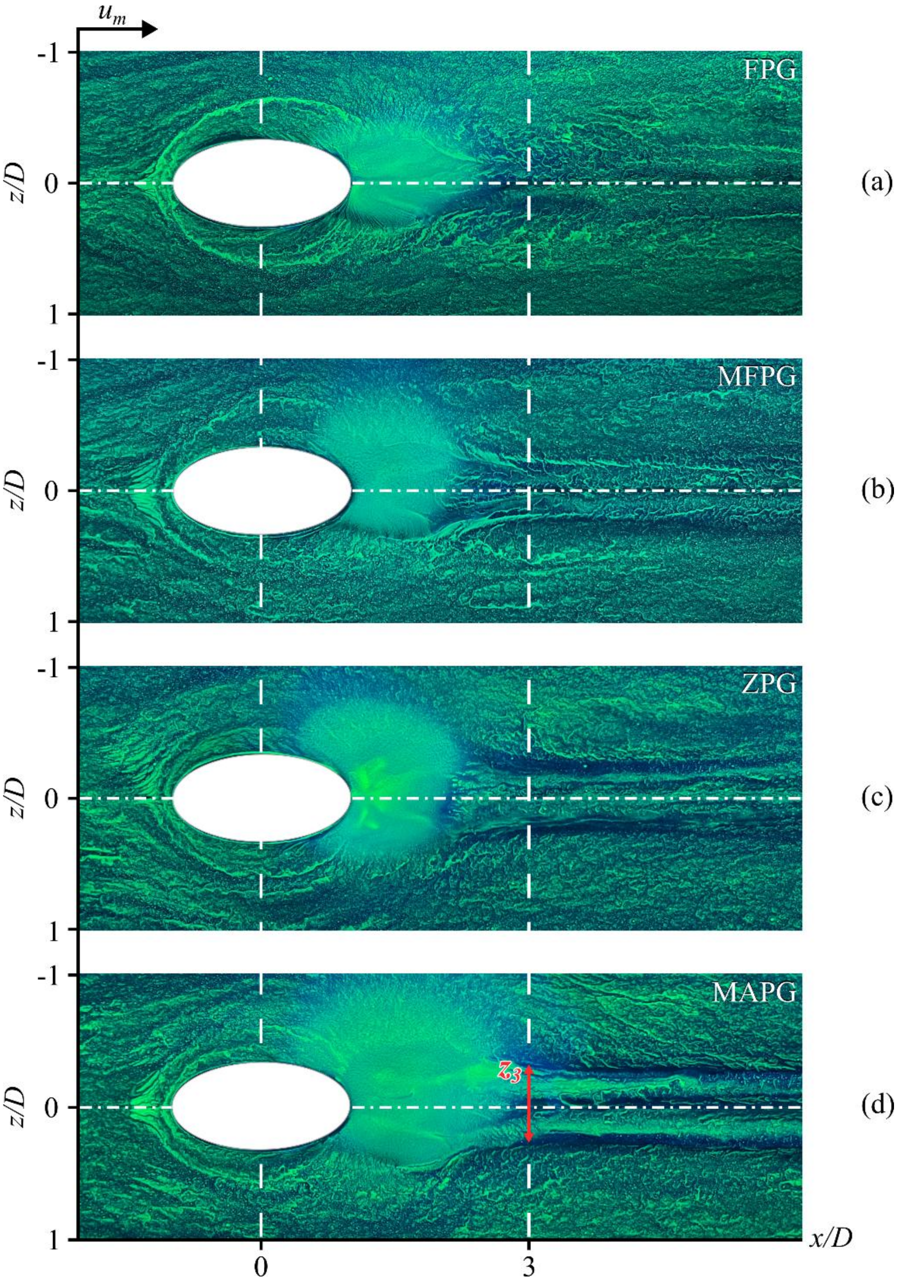

Figure 5.6: Endwall oil-dye flow visualisation for (a) FPG, (b) MFPG, (c) ZPG, and (d) MAPG while maintaining a constant M = 1.0 for $Re_D = 1.4\times10^4$ (u_m = 11.5 m/s)

Downstream of the ejection point at $x/D = 3.0$, Wake Region III (as shown in Figure 5.3(d)) is observed by the dark streamline streaks that propagate and encompass the wake region up to the end of the image at $x/D = 6.0$. In all four pressure gradient cases the dark streamwise streaks are observed, however, the MAPG case inhibits a more pronounced distinction line. This could be explained by the entrainment of the flow towards the centreline of the jet at $z/D = 0.0$. This matches with the findings of Andreopoulos et al. [7] in his experimental investigation of the wake region of jets in cross flow, as the results showed that vortical structures are entrained upwards towards the detached jet. The spacing between the dark streamwise streaks are labelled as z_3 as shown in Figure 5.6(d) in red. At $x/D = 3.0$, the value of z_3 increases with a decrease in acceleration parameter similar to Wake Region I and Wake Region II.

5.4 Overall Jet-Endwall Interaction with Varied Blowing Ratio and Pressure Gradient

Figure 5.7 demonstrates how the jet's coverage and attachment to the endwall is affected simultaneously with the variation of blowing ratio and pressure gradient. For a fixed pressure gradient, Figure 5.7(a) shows that the kidney vortex core spacing (z_1) and the endwall Wake Region III width (z_3) increases with blowing ratio. The pressure gradient appears to affect the rate of growth of the kidney vortex core spacing and wake width. For example, the adverse pressure gradient case (MAPG) shows that the endwall wake width and kidney vortex core spacing grow at the highest rate (i.e., steepest gradient $\mathrm{d}z_1/\mathrm{d}M \approx 1.27$) as the blow ratio increases. In contrast, for the zero-pressure gradient (ZPG), mild favourable (MFPG), and favourable pressure gradient (FPG) cases, the gradient is approximately the same $\mathrm{d}z_1/\mathrm{d}M \approx 0.25$, 0.32, and 0.33 respectively. Hence the kidney vortex structure and endwall coverage is more strongly affected by blowing ratio for the zero to adverse pressure gradient range. In addition, Figure 5.7(a) indicates that there is a good correspondence between the jet kidney vortex lateral spreading and the projection of the vortex cores onto the endwall, since the wake width slopes ($\mathrm{d}z_1/\mathrm{d}M \approx \mathrm{d}z_3/\mathrm{d}M$) is closely matched to the kidney vortex core lateral spacing for the certain pressure gradients tested. The systematic offset between z_1 and z_3 is related to the kidney vortex core spacing, typically being larger than the endwall Wake Region III. Figure 5.7(b) shows a map of the attachment of the jet to the endwall surface based on blowing ratio and pressure gradient (i.e., acceleration parameter). Three regimes of jet-endwall interaction are defined as (i) attached, (ii) semi-detached, and (iii) detached that were determined according to the planar laser visualization experiments.

Initially, if the blowing ratio is fixed (e.g., $M = 1$) and the pressure gradient varies the jet flow is detached from the endwall when external pressure gradient is adverse $K < 0$**.** However, as the pressure gradient becomes favourable (i.e., $K > 0$) the tendency of the jet to separate from the endwall reduces. For the strong favourable pressure gradient (i.e., $K \approx 2.6\times10^{-6}$), the jet flow attaches strongly to the endwall, and the height of the kidney vortex (i.e., $y/D \approx y_1 \approx 0.45$) decreases (see Figure 5.5(d)). Similarly, increasing the blowing ratio from a low value of $M = 0.1$ to 2.0 for a fixed streamwise pressure gradient (e.g., K = 0) results initially in the jet flow being attached to the endwall. However, when a critical blowing ratio is reached (i.e., $M \approx 0.8$) the cooling jet detaches and then reattaches to the endwall (see Figure 5.1(b)) at the x/D = 3 location. Further increasing the blowing ratio, then results in complete detachment and limited interaction of the cooling jet with the endwall, rather the mainstream interacts directly with the endwall which is likely to adversely affect filming cooling effectiveness (FCE). From the results obtained, an indication to the behaviour of the film cooling effectiveness could be deduced based previous research. It is well known that to improve the film cooling effectiveness, the film temperature along the endwall surface should retain the coolant ejection temperature [1], [10], [23], [63], [66]. Detachment of the film coolant jet causes entrainment of the mainstream flow and increases dilution of the jet, thus, resulting in an increase in the temperature at the endwall surface (i.e. blade surface). Therefore, applying a blowing ratio and pressure gradient combination that results in attached flow should result in an increase in the film cooling effectiveness compared to detached flow or semi-detached flow.

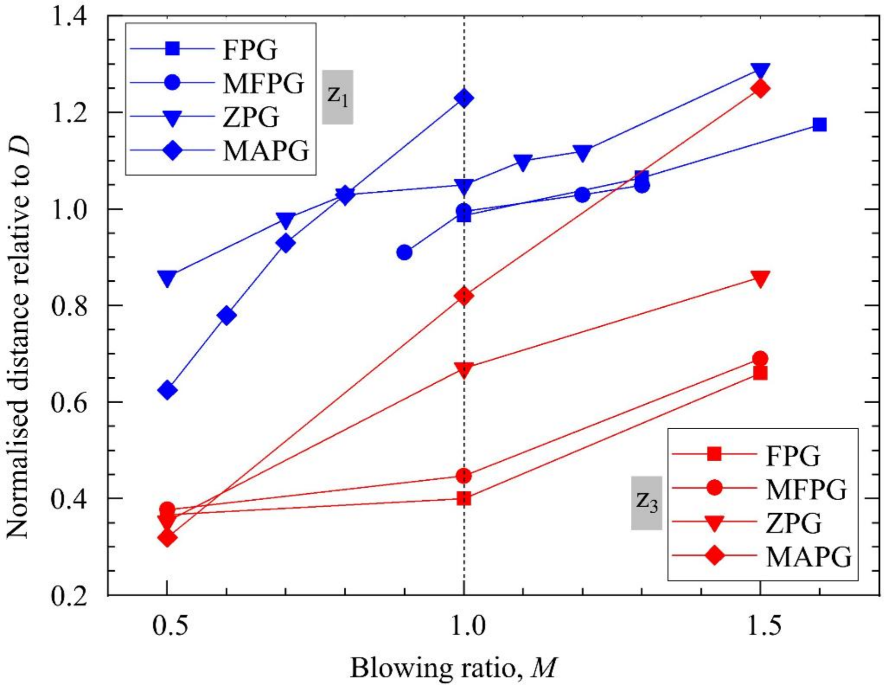

(a)

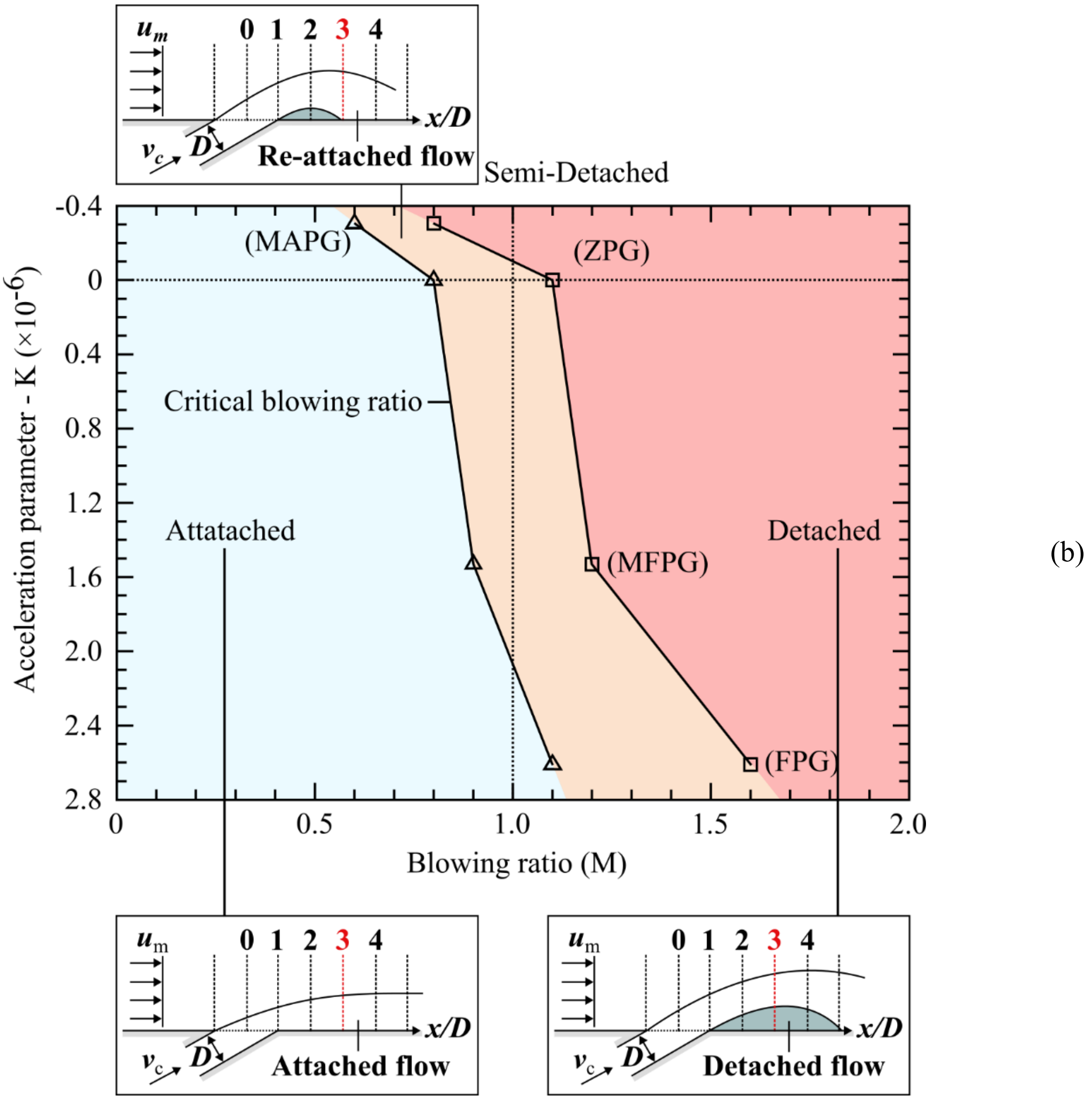

Figure 5.7: (a) summary of the y_1 and z_1 values for varying blowing ratios under a ZPG (∇), MAPG (◊), MFPG (○), and FPG (□), and (b) summary of the critical blowing ratio, and attached (Δ), semi-detached (between Δ and □) and detached (□) film cooling jets at varying blowing ratios and pressure gradients

5.5 Summary of Mainstream – Jet – Endwall Interaction

The PIV velocity map and endwall oil dye visualization, provide new insight of the jet structure and interaction of the jet with the endwall. Figure 5.8 is a schematic combining the jet's kidney vortex development together with the endwall wake structures for an inclined filming cooling jet submerged in the mainstream. For a favourable pressure gradient (FPG), and moderate blowing ratio (M = 1) the experimental results have demonstrated that the film cooling jet is attached to the endwall, and the kidney vortex affects the endwall coverage by the jet, at predominantly the Wake Region III. The present results showed a strong correspondence between the jet structure (i.e., lateral kidney vortex core spacing (z_1) that was characterized using PIV and the endwall wake structure (Wake Region III, wide z_3) using oil-dye visualization. Furthermore, Wake Region III width, appears to be affected significantly by the blowing ratio (M), and less by the pressure gradient as shown by Figure 5.7(a). On the other hand, Wake

Region II, endwall pattern is not substantially affected by variations of blowing ratio (*M*), and pressure gradient (PG), and typically extends up to the *x/D* =3 downstream location. The endwall flow oil dye visualization (see Figure 5.3) reveals important details of how the mainstream interacts with the inclined jet. Here, Wake Region I is formed by the interaction between the mainstream and jet as a horseshoe vortex structure that wraps around the jet and develops a strong recirculation zone at the jet exit. The horseshoe vortex forms upstream of the jet at the separation line adjacent to the endwall, where mixing of the mainstream and jet takes place. The enhanced mixing upstream and at the jet exit is therefore likely to decrease the film cooling effectiveness (FCE) in the localized, Wake Region I zone, due to reduced cooling flow replenishment. Wake Region I typically extends to a distance of *x/D* ≈ 1.5 downstream of the jet exit, and structure of this zone is mostly independent of pressure gradient and blowing ratio.

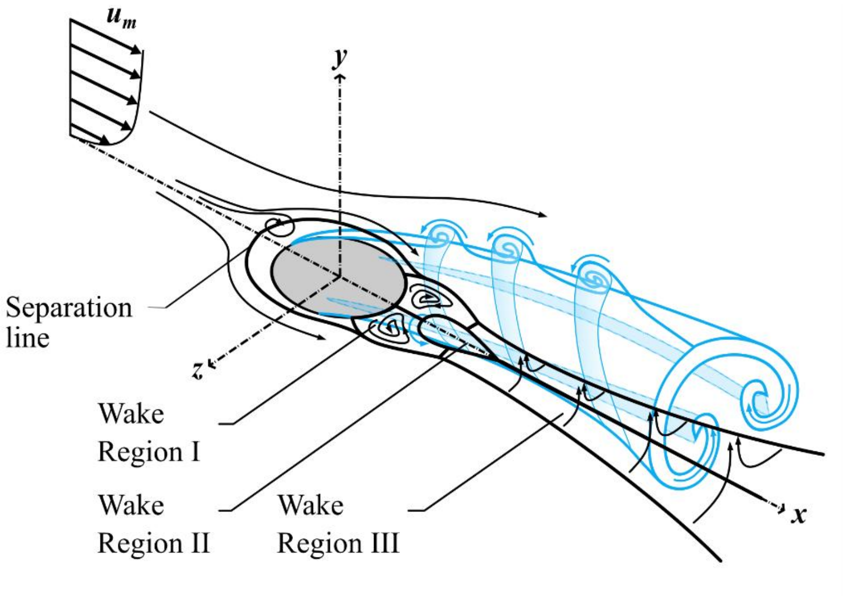

Figure 5.8: Schematic of the kidney vortex and endwall structure of a coolant jet in crossflow

6 Conclusion

An experimental study was undertaken to evaluate how both blowing ratio (M) and streamwise pressure gradient (PG) affects the coverage of the film cooling jet over the endwall surface. Consideration was given to demonstrate the structure of the jet's kidney vortex, and detachment and attachment of a film cooling jet from/to a downstream endwall surface. To this end, a series of experiments conducted for four pressure gradients: favourable, mild favourable, zero, and mild adverse PGs, respectively corresponding to the acceleration parameter of K = 2.6×10^{-6}, 1.5×10^{-6}, 0.0, and (-) 0.3×10^{-6} were conducted. Furthermore, the blowing ratio was varied systematically from M = 0.5 to 2.0 for a fixed Reynolds number of Re_D = 14,000 based on a film cooling jet diameter of D = 20.0 mm, ejecting at the angle of 30° measured from the endwall surface.

For visualization and quantification of film cooling jet structures e.g., plume height and detachment lengths, particle image velocimetry with planar laser illumination was employed. Our data demonstrates that the dependence of film cooling jet's detachment and attachment on the PG exists only in $0.5 < M < 1.1$: the film cooling jet becomes detached from the flat endwall surface as the PG becomes favourable transitioning from being adverse i.e., the increased K. On the contrary, below M = 0.5, the PG plays no part in determining the detachment and attachment of a film cooling jet, all being attached. Similarly, above M = 1.6, the film cooling jet is all detached regardless of the PG. Furthermore, the oil dye visualisation demonstrated how the film cooling jet interacts with the endwall and provided insight into the coverage of the jet over the surface under various blowing ratios and pressure gradients.

7 Recommendation for Future work

This study looked at the effects of blowing ratio and pressure gradients on the coolant jet attachment and detachment from the endwall surface. This was accomplished by replicating engine representative pressure gradients across a flat endwall test section surface and introducing a secondary flow with varying blowing ratios. Time averaged data was collected using particle image velocimetry (PIV), planar laser visualisation (PLV), and oil-dye endwall visualisation. The results demonstrated that the pressure gradient influenced the film cooling jet detachment and attachment between the critical blowing ratios of $0.5 < M < 1.1$.

This study recommends further investigation into the effects of an imposed streamwise pressure gradient has on rows of film cooling holes. Particularly looking at the endwall topology and jet detachment for varying hole spacings (both in the z-direction, and x-direction). This would provide insight into the effects that an upstream impingement (coolant jet) has on the downstream hole. This would require careful consideration on the pressure gradient imposed and hole spacing as the mainstream flow velocity continues to increase downstream of the ejection point. This would lead into optimising hole spacing, location and critical blowing ratio across turbine blade geometries.

This study also recommends investigating the effects that secondary flows on the boundary layer have on the attachment and detachment of the coolant jet. The cooling near the hub and tip of a gas turbine blade has secondary flows that affect that coolant trajectory which reduce the coolant coverage in these regions. Investigating the effects that secondary flows have on a coolant jet would improve the coverage and understanding of how to improve the coolant deposition in this region of the blade.

8 References

[1] J. C. Han, 'Advanced Cooling in Gas Turbines 2016 Max Jakob Memorial Award Paper', Nov. 01, 2018, *American Society of Mechanical Engineers (ASME)*. doi: 10.1115/1.4039644.

[2] J. Zhang, S. Zhang, C. Wamg, and X. Tan, 'Recent advances in film cooling enhancement: A review', Apr. 01, 2020, *Chinese Journal of Aeronautics*. doi: 10.1016/j.cja.2019.12.023.

[3] J.-C. Han and L. M. Wright, 'Enhanced Internal Cooling of Turbine Blades and Vanes', 2006.

[4] J.-C. Han, S. Dutta, and S. Ekkad, *Gas Turbine Heat Transfer and Cooling Technology*, 2nd ed. New York: CRC Press Taylor and Francis Group, LLC, 2013.

[5] B. Lakshminarayana, *Fluid Dynamics and Heat Transfer of Turbomachinery*. New York: John Wiley & Sons, Inc, 1996.

[6] J. Anderson, *Fundamentals of Aerodynamics*, 6th Edition. Mc Graw Hill Education, 2017.

[7] J. Andreopoulos and W. Rodi, 'Experimental investigation of jets in a crossflow', *J Fluid Mech*, vol. 138, pp. 93–127, 1984, doi: 10.1017/S0022112084000057.

[8] T. T. Lim, T. H. New, and S. C. Luo, 'On the development of large-scale structures of a jet normal to a cross flow', *Physics of Fluids*, vol. 13, no. 3, pp. 770–775, 2001, doi: 10.1063/1.1347960.

[9] R. M. Kelso and T. T. Lims, 'An experimental study of round jets in cross-flow', 1996.

[10] V. L. Eriksen and R. J. Goldstein, 'Heat Transfer and Film Cooling Following Injection Through nclined Circular Tubes', *Heat Transfer*, pp. 239–245, 1974.

[11] P. G. Saffman, *Vortex Dynamics*. Cambridge University Press, 1993. doi: 10.1017/CBO9780511624063.

[12] H. C. Lange, 'Jet in Crossflow: Experiments on the interaction of flow-structure and cooling efficiency', in *10th International Conference on Heat Transfer, Fluid Mechanics and Thermodynamics*, 2014, pp. 886–896.

[13] A. McCoy, G. Constantinescu, and L. Weber, 'Coherent Structures and Mass Exchange Processes in Channel Flow with Spanwise Obstructions', in *Engineering Turbulence Modelling and Experiments 6*, Elsevier, 2005, pp. 277–286. doi: 10.1016/B978-008044544-1/50026-1.

[14] A. C. Devoria and K. Mohseni, 'Vortex sheet roll-up revisited', *J Fluid Mech*, vol. 855, pp. 299–321, Nov. 2018, doi: 10.1017/jfm.2018.663.

[15] H. Lange, 'Jet in crossflow: experiments on the interaction of flow-structure and cooling efficiency', 2014.

[16] W. Jessen, M. Konopka, and W. Schroeder, 'Particle-image velocimetry measurements of film cooling in an adverse pressure gradient flow', *J Turbomach*, vol. 134, no. 2, Jul. 2011, doi: 10.1115/1.4003175.

[17] Y. Qin, J. Ren, and H. Jiang, 'Effects of streamwise pressure gradient and convex curvature on film cooling effectiveness', in *ASME Turbo Expo*, 2014.

[18] K. Mahesh, 'The interaction of jets with crossflow', Jan. 2013. doi: 10.1146/annurev-fluid-120710-101115.

[19] Nitshe, 'Vortex Dynamics', New Mexico, 2006.

[20] B. A. Haven and M. Kurosaka, 'Kidney and anti-kidney vortices in crossflow jets', *J Fluid Mech*, vol. 352, pp. 27–64, Dec. 1997, doi: 10.1017/S0022112097007271.

[21] H. Schlichting and K. Gersten, *Boundary-Layer Theory*. Springer Berlin Heidelberg, 2016. doi: 10.1007/978-3-662-52919-5.

[22] R. J. Goldstein, 'Film Cooling', Minneapolis, 1970.

[23] S. Bernsdorf, M. G. Rose, and R. S. Abhari, 'Modelling of Film Cooling - Part I: Experimental Study of Flow Structure', in *ASME Turbo Expo: Power for Land, Sea and Air*, 2005, pp. 1–11.

[24] D. L. Schmidt and D. G. Bogard, 'Pressure Gradient Effects on Film Cooling', 1995.

[25] N. Hay, D. Lampard, and C. L. Saluja, 'Effects of the Condition of the Approach Boundary Layer and of Mainstream Pressure Gradients on the Heat Transfer Coefficient on Film-Cooled Surfaces', *J Eng Gas Turbine Power*, vol. 107, pp. 99–104, 1985.

[26] A. J. H. Teekaram, C. J. P. Forth, and T. V Jones, 'Film Cooling in the Presence of Mainstream Pressure Gradients', *J Turbomach*, vol. 113, pp. 484–492, 1991.

[27] S. W. Schekman, T. J. Lu, and T. Kim, 'Gas Turbine Airfoil Cooling Technologies: A Review', Johannesburg, Aug. 2021.

[28] M. Gambini and M. Vellini, 'Preliminary Design of Axial Flow Turbines', 2021, pp. 109–153. doi: 10.1007/978-3-030-51299-6_3.

[29] W. Du, L. Luo, Y. Jiao, S. Wang, X. Li, and B. Sunden, 'Heat transfer in the trailing region of gas turbines – A state-of-the-art review', *Appl Therm Eng*, vol. 199, Nov. 2021, doi: 10.1016/j.applthermaleng.2021.117614.

[30] K. Yeranee and Y. Rao, 'A review of recent studies on rotating internal cooling for gas turbine blades', Jul. 01, 2021, *Elsevier B.V.* doi: 10.1016/j.cja.2020.12.035.

[31] Z. Gao, D. P. Narzary, and J. C. Han, 'Film cooling on a gas turbine blade pressure side or suction side with axial shaped holes', *Int J Heat Mass Transf*, vol. 51, no. 9–10, pp. 2139–2152, May 2008, doi: 10.1016/j.ijheatmasstransfer.2007.11.010.

[32] U. Drost, A. Boics, and A. Hoffs, 'Utilization of the Transient Liquid Crystal Technique for Film Cooling Effectiveness and Heat Transfer Investigations on a Flat Plate and a Turbine Airfoil', 1997.

[33] D. P. Narzary, K. C. Liu, A. P. Rallabandi, and J. C. Han, 'Influence of coolant density on turbine blade film-cooling using pressure sensitive paint technique', *J Turbomach*, vol. 134, no. 3, Jul. 2011, doi: 10.1115/1.4003025.

[34] N. Abuaf, R. Bunker, C. P. Lee Ge, and A. Engines, 'Heat Transfer and Film Cooling Effectiveness in a Linear Airfoil Cascade', *J Turbomach*, vol. 119, 1997.

[35] M. F. Blair and H. D. Joslyn, 'The Effects of Turbulence and Stator/Rotor Interactions on Turbine Heat Transfer: Part II-Effects of Reynolds Number and Incidence', *J Turbomach*, vol. 111, 1989.

[36] L. D. Hylton, V. Nirmalan, B. K. Sultanian, and R. M. Kaufman, 'The Effects of Leading Edge and Downstream Film Cooling on Turbine Vane Heat Transfer', 1988.

[37] C. Camci and T. Arts, 'An experimental convective heat transfer investigation around a film-cooled gas turbine blade', *J Turbomach*, vol. 112, no. 3, pp. 497–503, 1990, doi: 10.1115/1.2927685.

[38] C. L. Liu, H. R. Zhu, J. T. Bai, and D. C. Xu, 'Film cooling performance of converging slot-hole rows on a gas turbine blade', *Int J Heat Mass Transf*, vol. 53, no. 23–24, pp. 5232–5241, Nov. 2010, doi: 10.1016/j.ijheatmasstransfer.2010.07.036.

[39] M. Jahnmiri, 'Boundary Layer Transitional Flow in Gas Turbines', Göteborg, Sweden, 2011.

[40] M. Ubaldi, P. Zunino, U. Campora, and A. Ghiglione, 'Detailed Velocity and Turbulence Measurements of the Profile Boundary Layer in a Large Scale Turbine Cascade', Genova, 1996.

[41] F. P. Incropera, D. P. DeWitt, T. L. Bergman, and A. S. Lavine, *Fundamentals of Heat and Mass Transfer*, 6th Edition. John Wiley & Sons, 2007.

[42] M. Y. Jabbari, R. J. Goldstein, K. C. Marston, and E. R. G. Eckert, 'Three dimensional flow at the junction between a turbine blade and end-waft *', *Warme- und Stoffubertragung*, vol. 27, pp. 51–59, 1992.

[43] C. H. Sieverding, 'Recent Progress in the Understanding of Basic Aspects of Secondary Flows in Turbine Blade Passages', *Engineering for Gas Turbines and Power*, vol. 107, pp. 248–257, 1985.

[44] L. S. Langston, M. L. Nice, and R. M. Hooper, 'Three-dimensional flow within a turbine cascade passage', *J Eng Gas Turbine Power*, vol. 99, no. 1, pp. 21–28, 1977, doi: 10.1115/1.3446247.

[45] L. S. Langston, 'Secondary flows in axial turbines - A review', in *Annals of the New York Academy of Sciences*, New York Academy of Sciences, 2001, pp. 11–26. doi: 10.1111/j.1749-6632.2001.tb05839.x.

[46] R. J. Goldstein and R. A. Spores, 'Turbulent Transport on the Endwall in the Region Between Adjacent Turbine Blades', *Heat Transfer*, vol. 144, no. 5, 1988.

[47] A. K. Sinha, D. G. Bogard, and M. E. Crawford, '90-GT-44 Gas Turbine Film Cooling: Flow Field due to a Second Row of Holes', 1990.

[48] M. K. Eberly and K. A. Thole, 'Time-resolved film-cooling flows at high and low density ratios', *J Turbomach*, vol. 136, no. 6, Nov. 2013, doi: 10.1115/1.4025574.

[49] B. Johnson, W. Tian, K. Zhang, and H. Hu, 'An experimental study of density ratio effects on the film cooling injection from discrete holes by using PIV and PSP techniques', *Int J Heat Mass Transf*, vol. 76, pp. 337–349, 2014, doi: 10.1016/j.ijheatmasstransfer.2014.04.028.

[50] W. Colban, A. Gratton, K. A. Thole, and M. Haendler, 'Heat transfer and film-cooling measurements on a stator vane with fan-shaped cooling holes', *J Turbomach*, vol. 128, no. 1, pp. 53–61, Jan. 2006, doi: 10.1115/1.2098789.

[51] T. Cambonie and J.-L. Aider, 'Transition scenario of the round jet in crossflow topology at low velocity ratios', May 2014, doi: 10.1063/1.4891850.

[52] R. J. Goldstein, E. R. G. Eckert, V. L. Eriksen, and J. W. Ramsey, 'FIlm cooling following injection through inclined circular tubes', 1969.

[53] R. J. Goldstein, E. R. G. Eckert, and J. W. Ramsey, 'Film cooling with injection through a circular hole', 1968.

[54] B. Jubran and A. Brown, ‘Film Cooling From Two Rows of Holes Inclined in the Streamwise and Spanwise Directions’, 1984.

[55] T. Behr Dipl, ‘Control of Rotor Tip Leakage and Secondary Flow by Casing Air Injection in Unshrouded Axial Turbines’, 2007.

[56] J. K. Vennard, *Elementary Fluid Mechanics*, 4th ed. New York: John Wiley & Sons, 1961.

[57] R. Zhu, T. W. Simon, and G. Xie, ‘Influence on film cooling effectiveness of novel holes based on cylindrical configurations’, *Numeri Heat Transf A Appl*, vol. 75, no. 7, pp. 469–488, Apr. 2019, doi: 10.1080/10407782.2019.1606629.

[58] K. M. Womack, R. J. Volino, and M. P. Schultz, ‘Measurements in Film Cooling Flows With Periodic Wakes’, *J Turbomach*, vol. 130, no. 4, Oct. 2008, doi: 10.1115/1.2812334.

[59] D. Luo, K. Zhang, J. Lei, G. Xie, and L. Wright, ‘Analysis of upstream, double-row, cylindrical holes on primary and secondary effects of endwall flow and film cooling’, *Int J Heat Fluid Flow*, vol. 82, p. 108568, Apr. 2020, doi: 10.1016/j.ijheatfluidflow.2020.108568.

[60] M. Straußwald, T. Sander, C. Abram, and M. Pfitzner, ‘Investigating the Influence of Mainstream Turbulence and Large Vortices on Gas Turbine Trenched Film Cooling Flows Using Planar Temperature-Velocity Imaging’, *J Turbomach*, vol. 144, no. 10, Oct. 2022, doi: 10.1115/1.4054215.

[61] E. Issakhanian, C. J. Elkins, and J. K. Eaton, ‘Film Cooling Effectiveness Improvements Using a Nondiffusing Oval Hole’, *J Turbomach*, vol. 138, no. 4, Apr. 2016, doi: 10.1115/1.4032045.

[62] Y. Qin, X. Li, J. Ren, and H. Jiang, ‘Effects of compound angle on film cooling effectiveness with different streamwise pressure gradient and convex curvature’, *Int J Heat Mass Transf*, vol. 86, pp. 482–491, 2015, doi: 10.1016/j.ijheatmasstransfer.2015.03.017.

[63] H. D. Ammari, N. Hay, and D. Lampard, ‘Effect of Acceleration on the Heat Transfer Coefficient on a Film Cooled Surface’, 1990. [Online]. Available: http://asmedigitalcollection.asme.org/GT/proceedings-pdf/GT1990/79078/V004T09A001/2399872/v004t09a001-90-gt-008.pdf

[64] B. Y. Maiteh and B. A. Jubran, ‘Effects of pressure gradient on film cooling effectiveness from two rows of simple and compound angle holes in combination’, *Energy Convers Manag*, vol. 45, no. 9–10, pp. 1457–1469, Jun. 2004, doi: 10.1016/j.enconman.2003.09.007.

[65] P. Dourmashkin, *Classical Mechanics*. 2024. [Online]. Available: https://LibreTexts.org

[66] J. Wang, Z. Zhao, L. Tian, X. Ren, and B. Sunden, ‘Effects of hole configuration on film cooling effectiveness and particle deposition on curved surfaces in gas turbines’, *Appl Therm Eng*, pp. 1–12, 2021.

[67] W. D. York and J. H. Leylek, ‘Numerical Prediction of Mainstream Pressure Gradient Effects in Film Cooling’, in *International Gas Turbine & Aeroengine Congress & Exhibition*, 1999, pp. 1–9. [Online]. Available: http://asmedigitalcollection.asme.org/GT/proceedings-pdf/GT1999/78606/V003T01A046/2412403/v003t01a046-99-gt-166.pdf

[68] C. R. B. Day, M. L. G. Oldfield, G. D. Lock, and S. N. Dancer, ‘Efficiency measurements of an annular nozzle guide vane cascade with different film cooling geometries’, in *International Gas Turbine & Aeroengine Congress & Exhibition*, 1998.

[69] S. Sarkar, K. Das, and D. Basu, ‘Film cooling on a turbine guide vane: A numerical analysis with a multigrid technique’, *Proceedings of the Institution of Mechanical Engineers, Part A: Journal of Power and Energy*, vol. 215, no. 1, pp. 39–54, 2001, doi: 10.1243/0957650011536552.

[70] H. W. Coleman and W. G. Steele, *Experimentation and Uncertainty Analysis for Engineers*, 2nd Edition. New York: John Wiley & Sons, 1999.

[71] B. S. Massey, *Mechanics of Fluids*. Toronto: D. Van Nostrand Company LTD, 1968.

[72] M. C. Potter, D. C. Wiggert, and B. H. Ramadan, *Mechanics of Fluids*, 5th ed. Cengage Learning, 2016.

[73] M. D. Atkins and T. Kim, ‘Isotropic-planar illumination for PIV experiments’, *Exp Fluids*, vol. 56, no. 3, pp. 1–10, Mar. 2015, doi: 10.1007/s00348-015-1932-8.

[74] S. Schekman, M. D. Atkins, and T. Kim, ‘Local end-wall heat transfer enhancement by jet impingement on a short pin-fin’, *Int J Heat Mass Transf*, vol. 128, 2019, doi: 10.1016/j.ijheatmasstransfer.2018.09.056.

[75] T. Kim, T. Lu, and S. Jin Song, *Application of Thermo-Fluidic Measurement Techniques: An Introduction*. Cambridge, United Kingdom: Elsevier, 2016. Accessed: Dec. 16, 2024. [Online]. Available: https://books.google.es/books?hl=en&lr=&id=NJo5DAAAQBAJ&oi=fnd&pg=PP1&dq=info:7bLWLlovJ_YJ:scholar.google.com&ots=Unw59hqTcG&sig=Lb6b7ab1BdIEn-Kv4RHEhIjM3Q4&redir_esc=y#v=onepage&q&f=false

[76] Dantec Dynamic Studio v8 Software Help, ‘PIV Uncertainty’. Accessed: Aug. 14, 2024. [Online]. Available:

https://service.dantecdynamics.com/help/DSHelp8/Content/Analysis/PIV%20Uncertainty/PIV%20Uncertainty.htm?cshid=1118#Charonko

[77] A. Sciacchitano, B. Wieneke, and F. Scarano, 'PIV uncertainty quantification by image matching', *Meas Sci Technol*, vol. 24, no. 4, 2013, doi: 10.1088/0957-0233/24/4/045302.

[78] A. Sciacchitano, 'Uncertainty quantification in particle image velocimetry', Jul. 19, 2019, *Institute of Physics Publishing*. doi: 10.1088/1361-6501/ab1db8.

[79] I. K. Choi, T. Kim, S. J. Song, and T. J. Lu, 'Endwall heat transfer and fluid flow around an inclined short cylinder', *Int J Heat Mass Transf*, vol. 50, no. 5–6, pp. 919–930, Mar. 2007, doi: 10.1016/j.ijheatmasstransfer.2006.08.012.

[80] S. Lee, K. Yee, and D. H. Rhee, 'Optimum arrangement of film cooling holes considering the manufacturing tolerance', *J Propuls Power*, vol. 33, no. 4, pp. 793–803, 2017, doi: 10.2514/1.B36210.

[81] F. E. Ames, 'Aspects of Vane Film Cooling with High Turbulence: Part I-Heat Transfer', *J Turbomach*, vol. 120, 1998.

[82] M. Y. Jabbari and R. J. Goldstein, 'Adiabatic Wall Temperature and Heat Transfer Downstream of Injection Through Two Rows of Holes', *Journal of Engineering for Power*, vol. 100, pp. 303–307, 1978.

[83] W. 0 Afejuku, N. Hay, and D. Lampard, 'Measured Coolant Distributions Downstream of Single and Double Rows of Film Cooling Holes', *J Eng Gas Turbine Power*, vol. 105, pp. 172–177, 1983.

[84] B. Jubran and A. Brown, 'Film Cooling From Two Rows of Holes Inclined in the Streamwise and Spanwise Directions', *J Eng Gas Turbine Power*, vol. 107, pp. 84–91, 1985.

[85] B. Y. Maiteh and B. A. Jubran, 'Effects of pressure gradient on film cooling effectiveness from two rows of simple and compound angle holes in combination', *Energy Convers Manag*, vol. 45, no. 9–10, pp. 1457–1469, Jun. 2004, doi: 10.1016/j.enconman.2003.09.007.

[86] J. E. Kingery and F. E. Ames, 'Full Coverage Shaped Hole Film Cooling in an Accelerating Boundary Layer with High Free-Stream Turbulence', 2015.

[87] C. J. Baker, 'The laminar horseshoe vortex', *J Fluid Mech*, vol. 95, no. 2, pp. 347–367, Nov. 1979, doi: 10.1017/S0022112079001506.

[88] S. Schekman and T. Kim, ‘Thermal flows around a fully permeable short circular cylinder’, *Int J Heat Mass Transf*, vol. 105, pp. 196–206, Feb. 2017, doi: 10.1016/j.ijheatmasstransfer.2016.09.089.

[89] S. Schekman, M. D. Atkins, and T. Kim, ‘Local end-wall heat transfer enhancement by jet impingement on a short pin-fin’, *Int J Heat Mass Transf*, vol. 128, pp. 1033–1047, Jan. 2019, doi: 10.1016/j.ijheatmasstransfer.2018.09.056.

Appendix A

To evaluate the effects of how both blowing ratio (*M*) and streamwise pressure gradient (PG) affects the film cooling jet over the endwall surface, a custom test section was designed and built as seen in Figure A.1. The design of the test section was split into two major components, the mainstream flow and the secondary flow.

The mainstream flow through the test section was required to vary along the streamwise direction to replicate engine representative pressure gradients over a turbine blade, such as the favourable, mild favourable, zero, and mild adverse with corresponding acceleration parameters of K_{FPG} = 2.6×10^{-6}, K_{MFPG} = 1.5×10^{-6}, K_{ZPG} = 0.0, and K_{MAPG} = (-) 0.3×10^{-6}. Additionally, the mean mainstream flow velocity (with a Reynolds number of Re_D = 14 000) at x = 0.0, and z = 0.0 (the centre of the hole) was to be consistent throughout the four cases to isolate the effects of the pressure gradients downstream of the ejection point.

The secondary flow was required to supply air at varying mean velocities to recreate the necessary blowing ratios between M = 0.5 to M = 2.0 in increments of M = 0.1. Additionally, the secondary flow was to merge with the mainstream channel at a 30° angle to the endwall surface with a hole diameter of 20.0 mm.

The design of the test section was to be modular to reduce the setup duration. To be able to replicate four pressure gradients using the same test section, a contoured surface was designed to vary the area through the channel. This design allowed for the experimental setup to remain constant whilst only one part was varied between pressure gradient cases. The secondary flow system and the connection to the mainstream channel was constant with only the contoured surfaces changed using bolts to allow for modularity.

The design of the test section also required careful consideration on the limiting factors of the centrifugal fan flow rates available in the laboratory. Taking into account the change in flow rate depending on the contoured surface meant that the secondary flow would be required to produce variable flow rates for all blowing ratios combinations with all four pressure gradient channels. The final design after considering all the necessary requirements, constraints, and criteria consisted of the parameters found in Table 0.1.

Table 0.1: Final design of mainstream channel and secondary flow system parameters.

Parameter	**Value**
Inlet height of test section	250 mm
Exit height of test section for:	
Favourable pressure gradient	100 mm
Mild favourable pressure gradient	150 mm
Zero pressure gradient	250 mm
Mild adverse pressure gradient	320 mm
Width of test section	100 mm
Length of test section	820 mm
Hole diameter	20 mm
Hole angle	30°

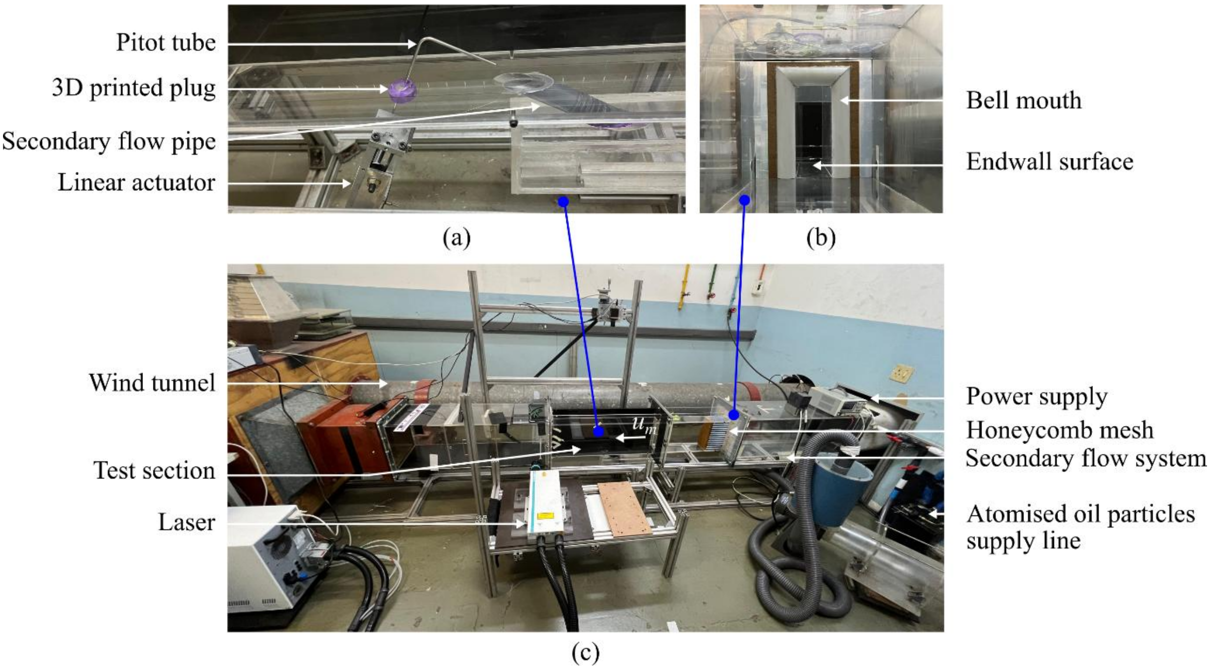

Figure A.1: Test section images for (a) pitot tube position to acquire secondary flow velocity profiles, (b) a through view of the test section inlet, and (c) complete experimental setup

The final design of the test section was assembled as is shown in Figure A.1 and in Appendix F where the technical drawings have been added to. The test section was introduced into an existing suction type wind tunnel with a cross-sectional area of width (w) × height (h) of 320.0 mm × 320.0 mm. The test section was made using 10.0 mm thick acrylic sheets to be able to observe the flow structures using PIV (Particle Image Visualisation), PLV (Planar Laser Visualisation), and oil-dye mixture. Connections between sheets were accomplished using countersunk screws and tapped holes into the acrylic sheets. This allowed for several tests to be conducted using the same equipment whilst reducing the amount of time between tests. A constant area channel with a length (l) × width (w) × height (h) of 570 × 100 × 250 mm was placed upstream of the test section to allow the flow to develop prior to entering the test section with the contoured surfaces. Two honeycomb meshes were placed at the inlet of the constant area channel with hexagonal sides of 10.0 mm (coarse mesh) and 2.0 mm (finer mesh). A bell mouth made from half pipes were stuck onto a thin sheet of wood and screw into the acrylic flange connecting the larger square channel to the narrow channel. The bell mouth allowed for smooth flow entry into the constant channel and thus the test section.

To create the acrylic contoured surfaces, the exact sizes of the acrylic sheets were cut using a laser cutter. The exact angle and shape of the contoured surface was achieved by heating the acrylic part at the precise location for the radius and placing it into a wooden mould for cooling. The wooden moulds (depending on the channel) were precisely manufactured using a CNC mill machine. The contoured acrylic part was heated using an industrial oven pre-heated to 350°C. This made the acrylic malleable in order to deform them into their respective wooden moulds to cool into the required angle to replicate the necessary area constriction through the channel to impose the pressure gradients.

The secondary flow was supplied from a centrifugal fan to the test section as shown in . The centrifugal fan was connected to a plenum made up of 100 mm diameter pipe and two acrylic flanges. A 21 mm diameter pipe was connected between the plenum near the centrifugal fan and the plenum prior to the connection to the lower surface of the channel. The lower surface of the channel had a hole drilled out using a CNC mill machine at the centre of the channel. A PVC round bar with outer diameter of 30.0 mm was manufactured into a pipe with an internal diameter of 20.0 mm. Two parts clear set epoxy was used to connect the manufactured pipe to the lower endwall surface.

The base of the PIV laser was connected to 10.0 mm thick acrylic sheets with a threaded hole placed on top of a constructed base made of wood placed on a structure of extruded aluminium components as shown in Figure A.2. The threaded holes on the acrylic sheets were designed to screw a sharpened bolt through the acrylic to easily level the laser.

The camera was placed on a liner and angular manipulator as shown in Figure A.2 to allow for ease of alignment of the camera to the test section. In particular, this design facilitated the alignment of the camera for the PIV cases 1, 2, and 3, where the camera position was changed.

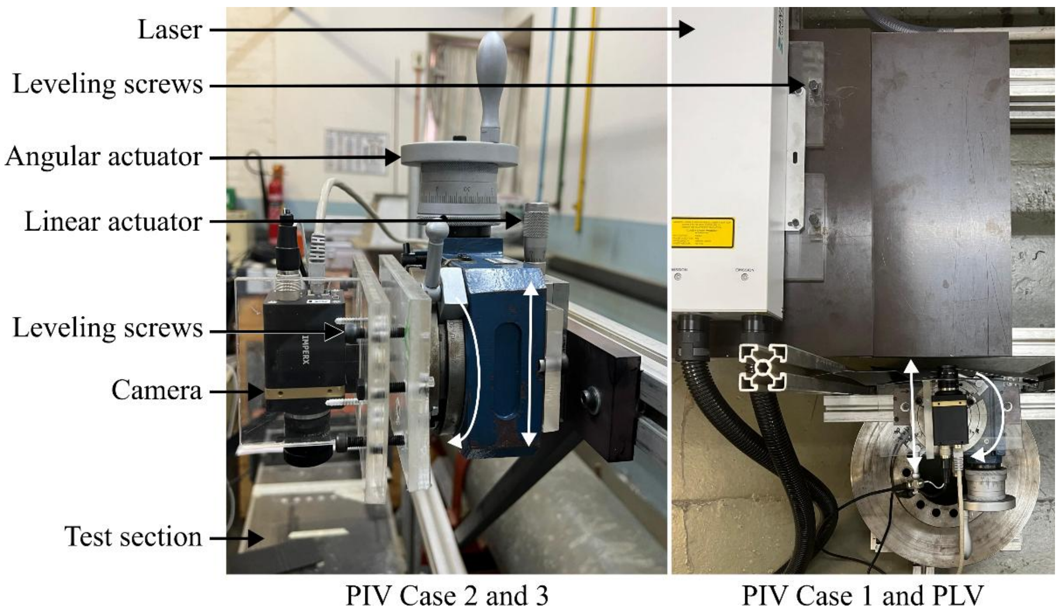

Figure A.2: Camera position and alignment system for PLV and PIV cases 1, 2, and 3

The calibration of the density of particles needed to seed the test area was done on a trial-and-error basis using a valve system placed after the seeding particle chamber. The valve system split the flow of particles from the mainstream and secondary flow. This allowed for particles to only be present during the planar laser visualisation tests where only the jet required seeding particles. Additionally, calibrating the density of particles released into the mainstream and secondary flow was achieved to balance the saturation of particles both in the jet plume and the mainstream flow. An uneven distribution of seeding particles between the jet plume and the mainstream flow resulted in dark regions within the flow visualisation images. These dark regions indicate areas where the Particle Image Velocimetry (PIV) software failed to detect sufficient particle density, leading to low signal intensity. As a consequence, the software was unable to accurately compute velocity vectors in these regions, often generating spurious vectors in the final vector field. Such errors can misrepresent the actual flow behavior and introduce inaccuracies in velocity and vorticity calculations. As such, to mitigate this issue, optimised seeding techniques, such as increasing particle density in low-seed regions by using dual-seeding approaches for both the jet and mainstream flow was employed to improve data reliability. Figure A.3 shows the variation in seeding particles seen during experimentation.

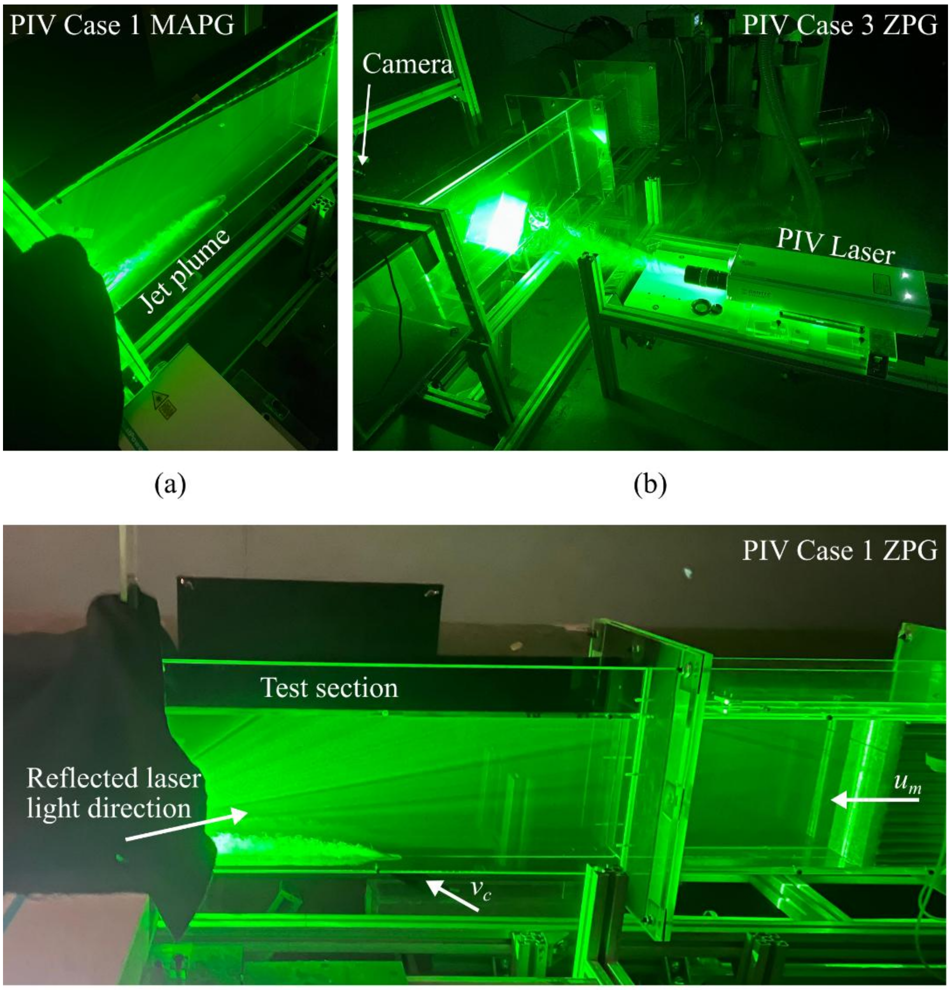

(c)

Figure A.3: Images of PIV data acquisition for three example cases (a) PIV streamwise case 1 (MAPG) angled view, (b) PIV case 3 at 45° to the y-z plane, and (c) PIV streamwise case 1 (ZPG) front view

The laser and camera system was carefully calibrated to capture the required PIV measurements. As described in §4.4.1, data collection was structured into three distinct cases:

- Case 1: Captured data on the x-y plane at $z = 0D$, covering a streamwise range from $x = -2D$ to $x = 8D$.
- Case 2: Captured data on the x-z plane from $x = -2D$ to $x = 4D$, at various heights (y = 2, 5, 10, 15, 20, 25, 30, 35, 40, and 45 mm).
- Case 3: Captured data at a 45° angle relative to the y-z plane, at multiple streamwise locations (x = -2D, -1D, 0D, 1D, 2D, 3D, and 4D).

Figure A.3 illustrates the data acquisition process for Cases 1 and 3. In Figure A.3(a, c), the laser light reflects off a conical mirror to illuminate particles along the centreline of the test section in Case 1. Meanwhile, Figure A.3(b) depicts a laser adapter, which was used to direct the light at a 45° angle, ensuring uniform particle illumination throughout the test section for Case 3.

Appendix B

To determine the blowing ratio, the mean velocity of the jet and the mainstream flow was required. The mean velocity of the mainstream and secondary flow were primarily calibrated separately. The mean mainstream flow velocity was calibrated based on the frequency of the motor. The frequency of the motor was increased in increments of 100 Hz at which points the centreline velocity was captured and plotted. This was performed for the varying pressure gradient channels as the mass flow rate through the test section increases with a decrease in area for a given motor frequency. The required velocity based on the Reynolds number of 14 000 was interpolated between the points for each channel configuration (i.e. favourable, mild favourable, zero, and mild adverse). The mean velocity was calculated as explained in §4.3.4 by taking the area weighted average of the transverse (in the y-direction) velocity profile across the centre (i.e. $z = 0$, and $x = 0$).

The mean velocity of the secondary flow used a similar approach to that of the mean mainstream flow. However, the mean secondary flow velocity at the exit of the ejection point was required under the influence of a pressure gradient. This is necessary as the pressure gradient in the channel affects the velocity of the secondary flow. There were three methods implemented to determine the mean velocity of the secondary flow, these were: using a pitot tube and integrating the velocity profile at the exit to get the area wetted average, using a flow meter, and extrapolating the velocity profile from PIV vector maps. The pitot tube method could not be used in the test section when a pressure gradient was imposed through the channel (i.e. mainstream flow through the channel) as the pitot tube would have to be inclined by 60° so the static pores were positioned perpendicular to the secondary flow streamlines. The mainstream flow, therefore, would approach the pitot tube at an angle and influence the velocity profile of the secondary flow jet. To work around this issue the following plan was implemented.

Firstly (A), the discharge coefficient of the orifice flow meter was determined using the setup shown in Figure B.1 as follows:

1. A traversed velocity profile (y-direction) was taken in increments of 1 mm across the diameter of the pipe measured using a pitot tube connected to a digital manometer.
2. The orifice flow meter was placed as shown in Figure B.1 and the differential pressure was measured using the digital manometer.
3. Applying the integral weighted area average equation from §4.3.4, the mean velocity was calculated from the velocity profile determined in Point 1.
4. Using equations from §4.3.4, the discharge coefficient was calculated to be ~0.7.

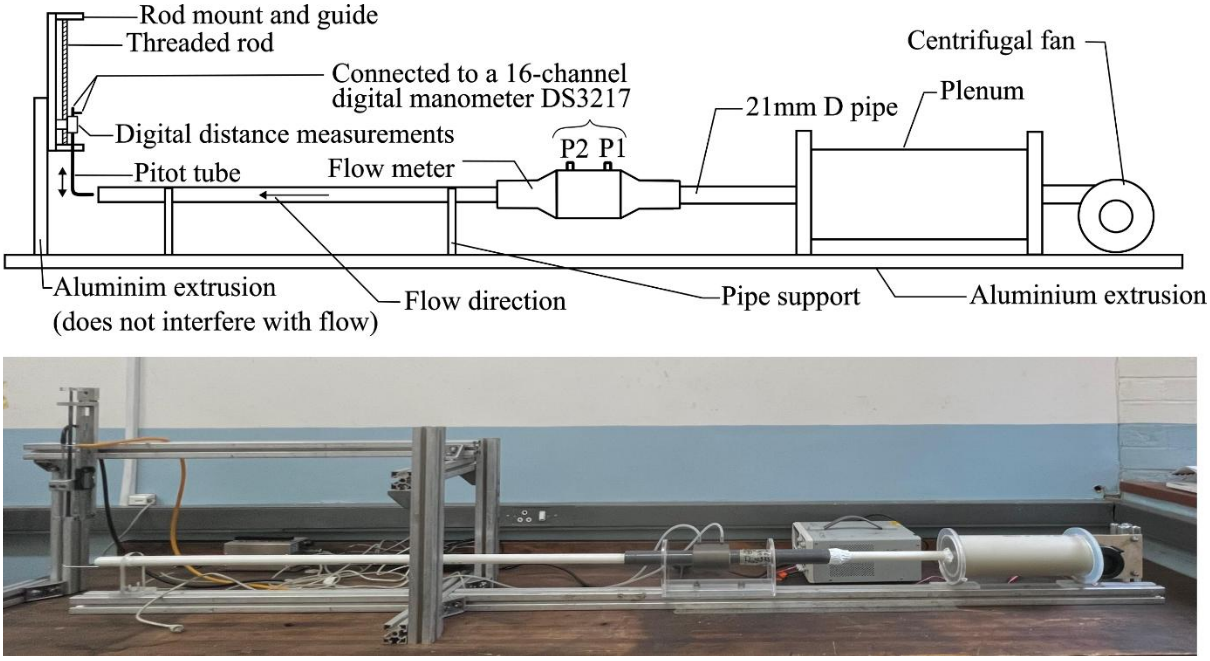

Figure B.1: Secondary flow orifice flow meter calibration to determine discharge coefficient

Secondly (B), a set of data was obtained in the mainstream channel when the secondary flow setup was connected to the test section without introducing mainstream flow (imposed pressure gradients) across the test section as follows:

1. At the ejection point, using a pitot tube, the velocity profile of the jet was obtained for varying fan speeds (measured by regulating the current in amps). Applying the integral weighted area average equation, the mean velocity was obtained.
2. Simultaneously an orifice flow meter placed upstream of the ejection point captured pressure measurement used to calculate the mean velocity of the jet.
3. The pitot tube was placed inside the secondary flow pipe and the centreline velocity in the pipe was obtained and compared to the centreline velocity at the exit. The percentage difference between the centreline velocity inside the pipe to outside the pipe was less than 1%.
4. A relationship between the mean velocity (u_{mean}) and the centreline velocity ($u_{centreline}$) was obtained, where: $u_{centreline}/u_{mean} \approx 1.37$.
5. Additionally, a PIV test was performed to verify the PIV data correlated with the pitot tube data and vice-versa. The % difference between the velocity profile obtained by the PIV and the pitot tube was less than 1%.

Thirdly (C), another set of data of the secondary velocity was obtained for the varying pressure gradients across the channel and varying fan speeds as follows:

1. The orifice flow meter placed upstream of the ejection point captured pressure measurement used to calculate the mean velocity of the jet with the discharge coefficient used.
2. The pitot tube was placed again inside the secondary flow pipe and the centreline velocity in the pipe was obtained.
3. A verification of the mean velocity calculated using the relationships mentioned in B and C with now an imposed pressure gradient was performed against PIV tests.

In summary, the data obtained in (A) was used to determine the discharge coefficient of the orifice flow meter. The data obtained in (B) was used to verify three things; the first was to determine the relationship between the mean velocity and the current of the motor; the second was to determine the difference between the centreline velocity inside and outside of the ejection pipe; and the third was to determine the relationship between the centreline velocity and the mean velocity of the jet. The data obtained in (C) was used determine both the centreline velocity and mean velocity using an orifice flow meter with the effects of the mainstream flow for each of the pressure gradient channels. The data obtained in A allowed for the discharge coefficient to be used in B and C. The data obtained in B allowed for the centreline velocity relationship to the mean velocity to be used in C. The data obtained in C allowed for the mean velocity of the flow to be used to calculate the blowing ratio.

Appendix C

```
%Start of code to transform vectors from the y-z plane at 45° to the vertical 90° y-z plane
clc;
clear;
format long

%Search for file with .dat format with the necessary data to transform.
[filename directory_name] = uigetfile('*.dat');
fullname = fullfile(directory_name, filename);

%Reads matrix of the file selected in search and assigns it to matrix I and B.
I = readmatrix(filename);
B = readmatrix(filename);

%Reads matrix of data of the file selected but stores it as a table with the headings provided in the following lines.
T = readtable(filename,'PreserveVariableNames',true);
opts = detectImportOptions(filename);
T.Properties.VariableNames={'"X[-]"','"Y[-]"','"X (pix)[pix]"','"Y (pix)[pix]"','"X (m)[m]"','"Y (m)[m]"','"U pix[pix]"','"V pix[pix]"','"U[m/s]"','"V[m/s]"','"W[m/s]"','"Length[m/s]"','"IA Width[pix]"','"IA Height[pix]"','"Peak height 1[-]"','"Peak height 2[-]"','"Peak height ratio[-]"','"Peak width 1[pix]"','"Peak width 2[pix]"','"Status[-]"','nothing'};

%Reads the lines 1 to 3 and 19163 to 19168 from the file selected in the search and stores them in Ylines and Ylinesend to be able to compile the transformed file and open in Tecplot 360.
Y = readlines(filename);
Ylines = Y(1:3,1);
Ylinesend = Y(19163:19168,1);

%Defines variable names either blank matrices or ones containing specific data from the file selected.
A = [];
I_v1 = I(:, 9);
I_w1 = I(:, 10);
I_l1 = I(:,12);
O = 45*pi/180;
T(:,21) = [];
I(:,21) = [];
```

```
%Transformation of the vectors from the two planes
for n = 1:1:length(I)
        Av = I_w1(n).*cos(O)+I_v1(n).*sin(O);
        Aw = -I_w1(n).*sin(O)+I_v1(n).*cos(O);
        Al = sqrt(Av^2+Aw^2);
        A = [A; Av, Aw, Al];
 if isnan(A(n,1))
        A(n,1) = 0;
 end
 if isnan(A(n,2))
    A(n,2) = 0;
 end
end

for n = 1:1:length(I)
   I(n,9) = B(n,11);
   I(n,10) = A(n,2);
   I(n,12) = A(n,3);
   I(n,20) = B(n,5)- 0.005;
   I(n,6) = B(n,6) + 0.014;
   I(n,11) = A(n,1);
   I(n,5) = 0.06;
end

%Writes a matrix and saves a '.dat' file with the new data under a specified file name ready to open
on Tecplot 360.
C = {Ylines; I; Ylinesend};
writematrix(Ylines, 'Newfilename.dat');
writematrix(I, ' Newfilename.dat','WriteMode', 'append', 'Delimiter', ' ');
writematrix(Ylinesend, ' Newfilename.dat','WriteMode','append');
```

Appendix D

The particle image velocimetry (PIV) system requires calibration to acquire images at specific flow rates through test sections to map the velocity flow field accurately. The system used in this study used a Dantec Dynamics Dual Power 65-15 laser with a wavelength of 532 nm. This laser has two light sources that pulse consecutively at a specific time interval to produce a light sheet to illuminate the flow field. A camera positioned perpendicular to the laser sheet captures images at the same time interval as the laser. The time required between pulses to capture the flow at a specific velocity is set converting the distance travelled of a particle (over a set distance) in the image plane to that of the object plane over the velocity of the of the flow in the object plane. This is defined as follows:

$$\Delta t = \frac{\left(pix_{pitch} \times \frac{1}{4} \times I_w \times S_f\right)}{u_m}$$

Where the pix_{pitch} is the distance between adjacent pixel centres (dictated by the camera specifications), I_w is the interrogation window size (16×16pix in this study with an overlap of 50%), u_m is the predicted mainstream velocity through the channel, and S_f is the scale factor which is the inverse of the magnification factor defined as follows:

$$S_f = \frac{1}{M_0}$$

Where M_0 is the magnification factor which is the size of the image plane relative to the object plane (the plane where the laser sheet is illuminating in the test section) as follows:

$$M_0 = \frac{pix \times pix_{pitch}}{d_{op}}$$

Where pix is the pixel count in the direction of the flow, pix_{pitch} is the distance between adjacent pixel centres (dictated by the camera specifications), and d_{op} is the perpendicular distance from the camera to the object plane.

Appendix E

237

TABLE A.2 The *t* Distribution[a]

ν	C = 0.900	0.950	0.990	0.995	0.999
1	6.314	12.706	63.657	127.321	636.619
2	2.920	4.303	9.925	14.089	31.598
3	2.353	3.182	5.841	7.453	12.924
4	2.132	2.776	4.604	5.598	8.610
5	2.015	2.571	4.032	4.773	6.869
6	1.943	2.447	3.707	4.317	5.959
7	1.895	2.365	3.499	4.029	5.408
8	1.860	2.306	3.355	3.833	5.041
9	1.833	2.262	3.250	3.690	4.781
10	1.812	2.228	3.169	3.581	4.587
11	1.796	2.201	3.106	3.497	4.437
12	1.782	2.179	3.055	3.428	4.318
13	1.771	2.160	3.012	3.372	4.221
14	1.761	2.145	2.977	3.326	4.140
15	1.753	2.131	2.947	3.286	4.073
16	1.746	2.120	2.921	3.252	4.015
17	1.740	2.110	2.898	3.223	3.965
18	1.734	2.101	2.878	3.197	3.922
19	1.729	2.093	2.861	3.174	3.883
20	1.725	2.086	2.845	3.153	3.850
21	1.721	2.080	2.831	3.135	3.819
22	1.717	2.074	2.819	3.119	3.792
23	1.714	2.069	2.807	3.104	3.768
24	1.711	2.064	2.797	3.090	3.745
25	1.708	2.060	2.787	3.078	3.725
26	1.706	2.056	2.779	3.067	3.707
27	1.703	2.052	2.771	3.057	3.690
28	1.701	2.048	2.763	3.047	3.674
29	1.699	2.045	2.756	3.038	3.659
30	1.697	2.042	2.750	3.030	3.646
40	1.684	2.021	2.704	2.971	3.551
60	1.671	2.000	2.660	2.915	3.460
120	1.658	1.980	2.617	2.860	3.373
∞	1.645	1.960	2.576	2.807	3.291

[a]Given are the values of t for a confidence level C and number of degrees of freedom ν.

Figure E.1: The t-distribution from Table A.1 in Coleman and Steele [70]

Appendix F

In the following pages are the technical drawings used to construct the test section.

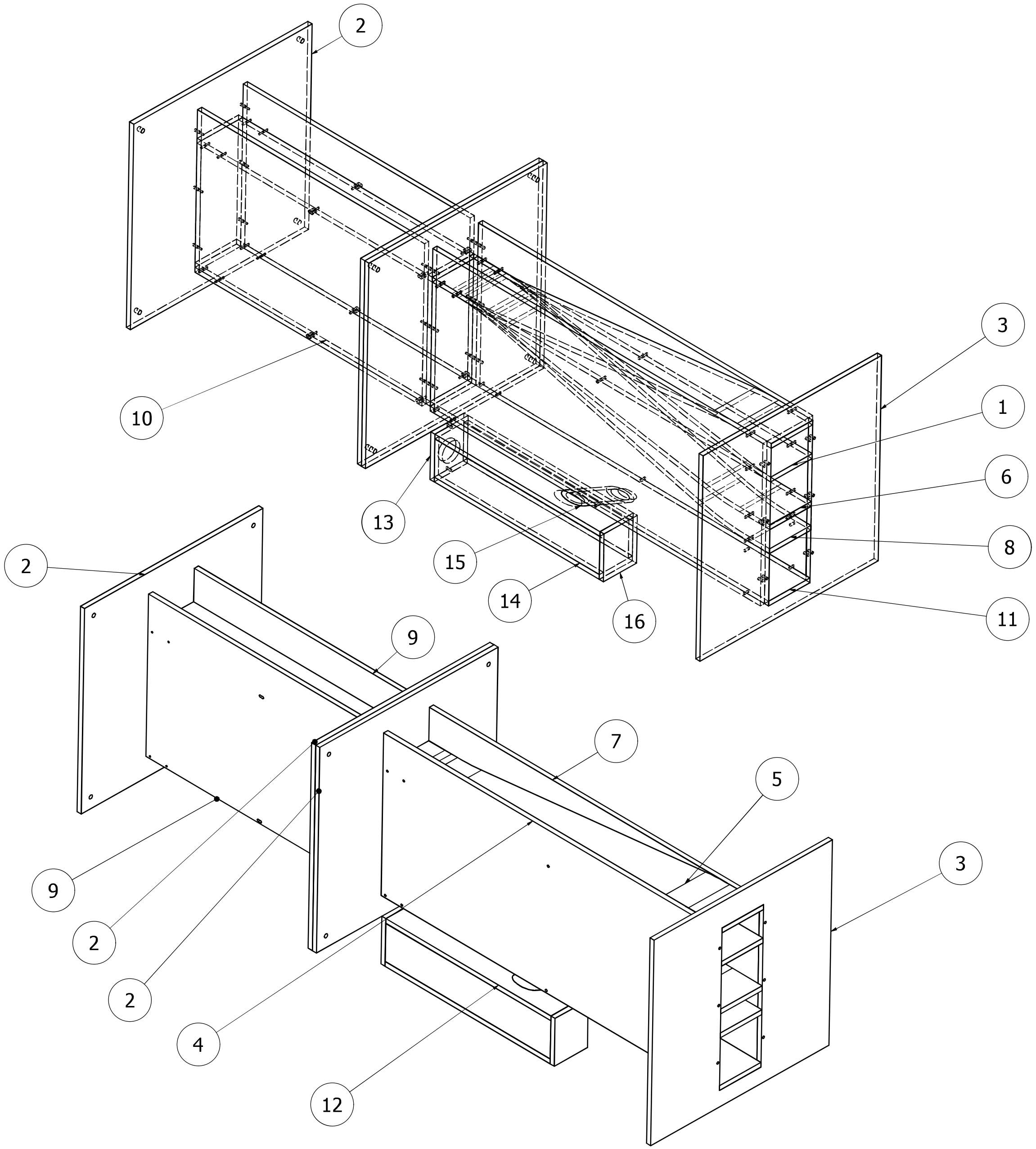

PARTS LIST		
ITEM	QTY	PART NUMBER
1	1	ZPG
2	3	Flange Inlet
3	1	Flange Outlet
4	1	Left Wall
5	1	MAPG
6	1	MFPG
7	1	Right Wall
8	1	FPG
9	2	Inlet Section Walls
10	2	Inlet Lower Surface
11	1	Lower Surface With Hole
12	1	Plenum Top With Hole
13	1	Plenum Connector
14	3	Plenum Side
15	1	Inlet Pipe
16	1	Plenum Back

DRAWN marcg	2025/03/23	
CHECKED		TITLE
QA		
MFG		
APPROVED		
SIZE D	DWG NO Assembly All Channels-1	REV
SCALE 1 / 4	SHEET 1 OF 1	

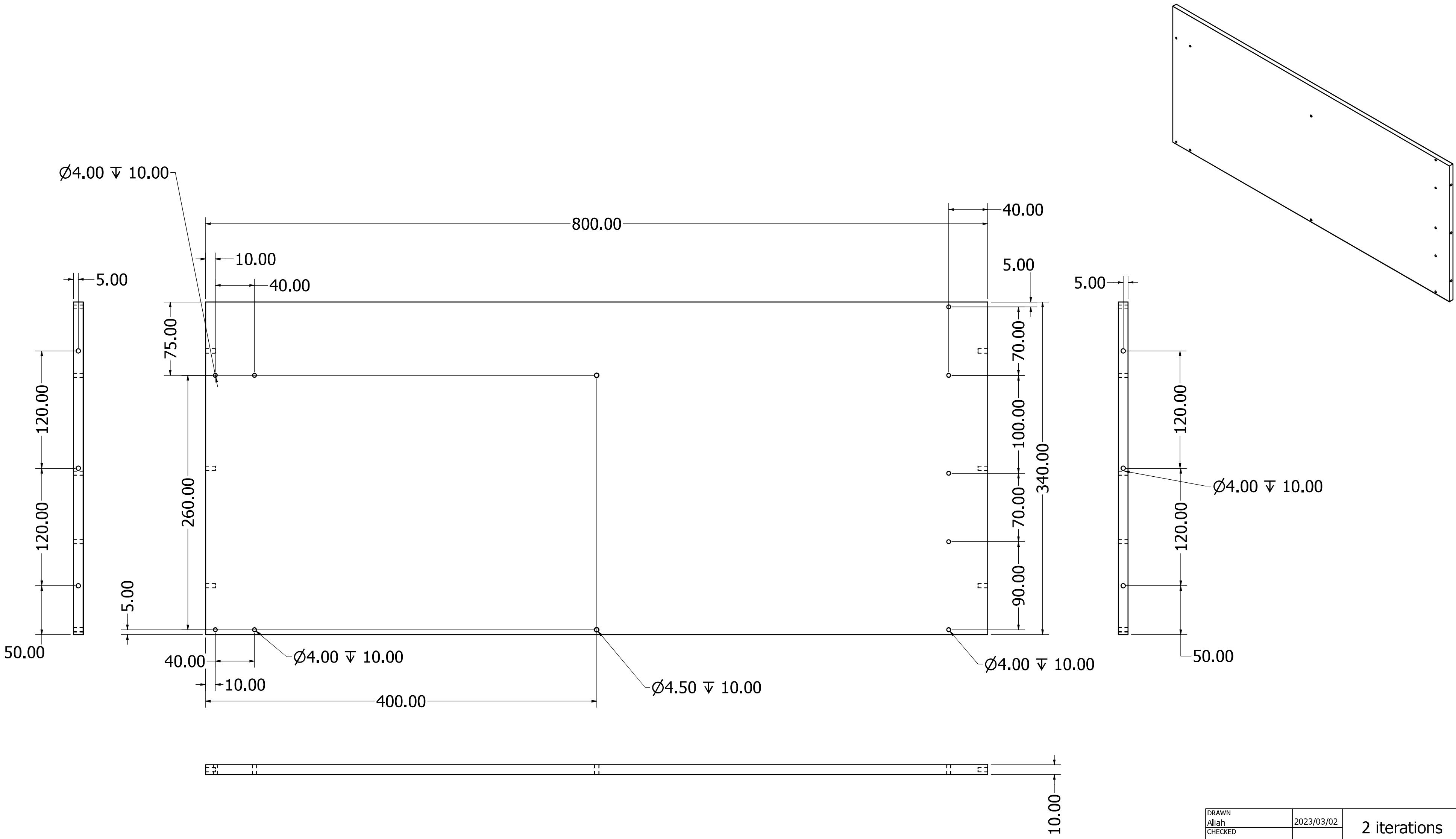

DRAWN Aliah 2023/03/02
CHECKED
QA
MFG
APPROVED

2 iterations

TITLE
Left and Right Walls

SIZE D
DWG NO Left_Wall
REV
SCALE 1 / 2
SHEET 1 OF 1

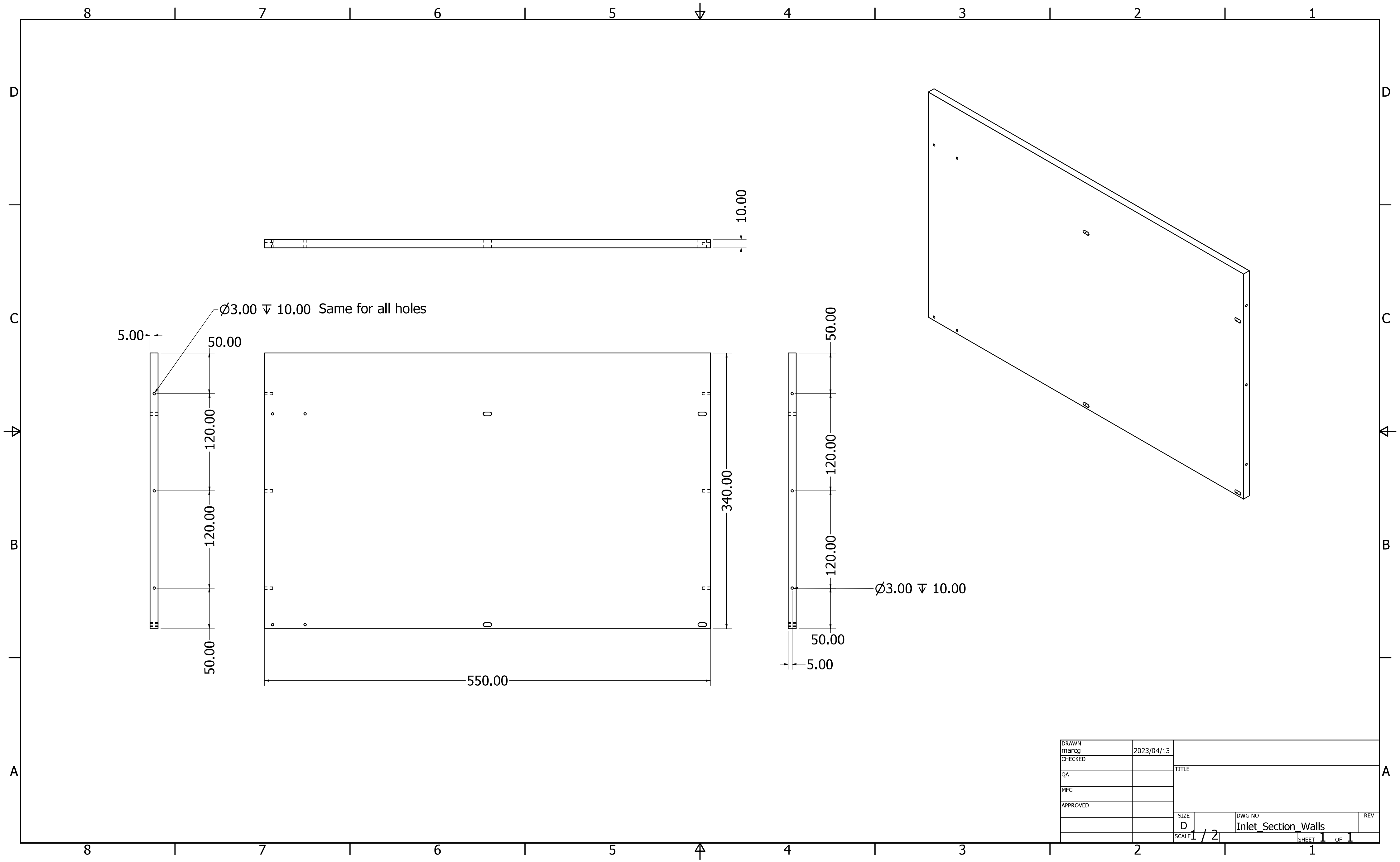

Ø3.00 ↧ 10.00 Same for all holes
5.00
50.00
120.00
120.00
50.00
550.00
340.00
10.00
50.00
120.00
120.00
Ø3.00 ↧ 10.00
50.00
5.00
DRAWN
marcg
2023/04/13
CHECKED
QA
MFG
APPROVED
TITLE
SIZE
D
DWG NO
Inlet_Section_Walls
REV
SCALE 1 / 2
SHEET 1 OF 1

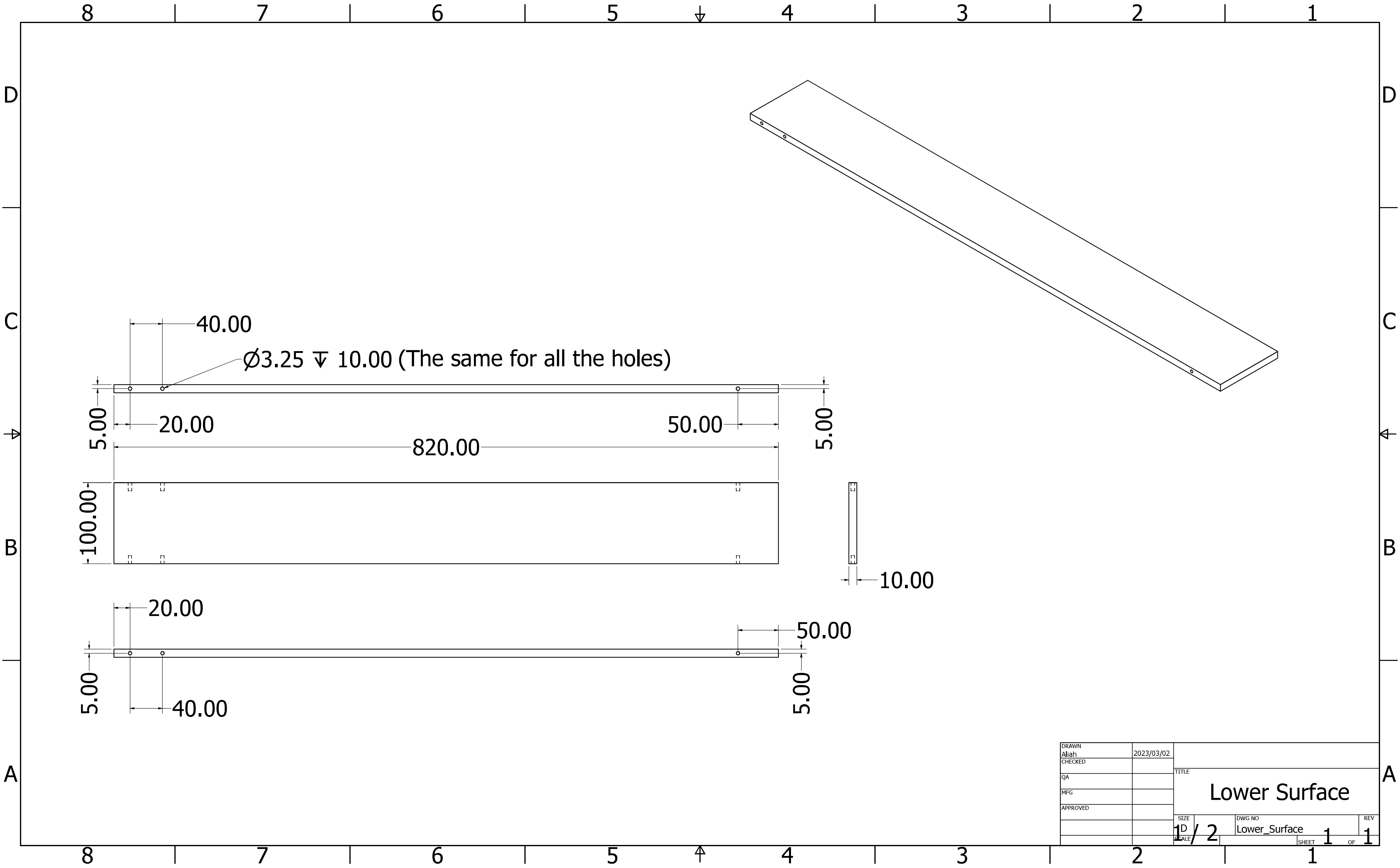
40.00
Ø3.25 ↧ 10.00 (The same for all the holes)
5.00
20.00
50.00
5.00
820.00
100.00
10.00
20.00
50.00
5.00
40.00
5.00
DRAWN
Aliah
2023/03/02
CHECKED
QA
MFG
APPROVED
TITLE
Lower Surface
SIZE
D
DWG NO
Lower_Surface
REV
SCALE
1 / 2
SHEET 1 OF 1

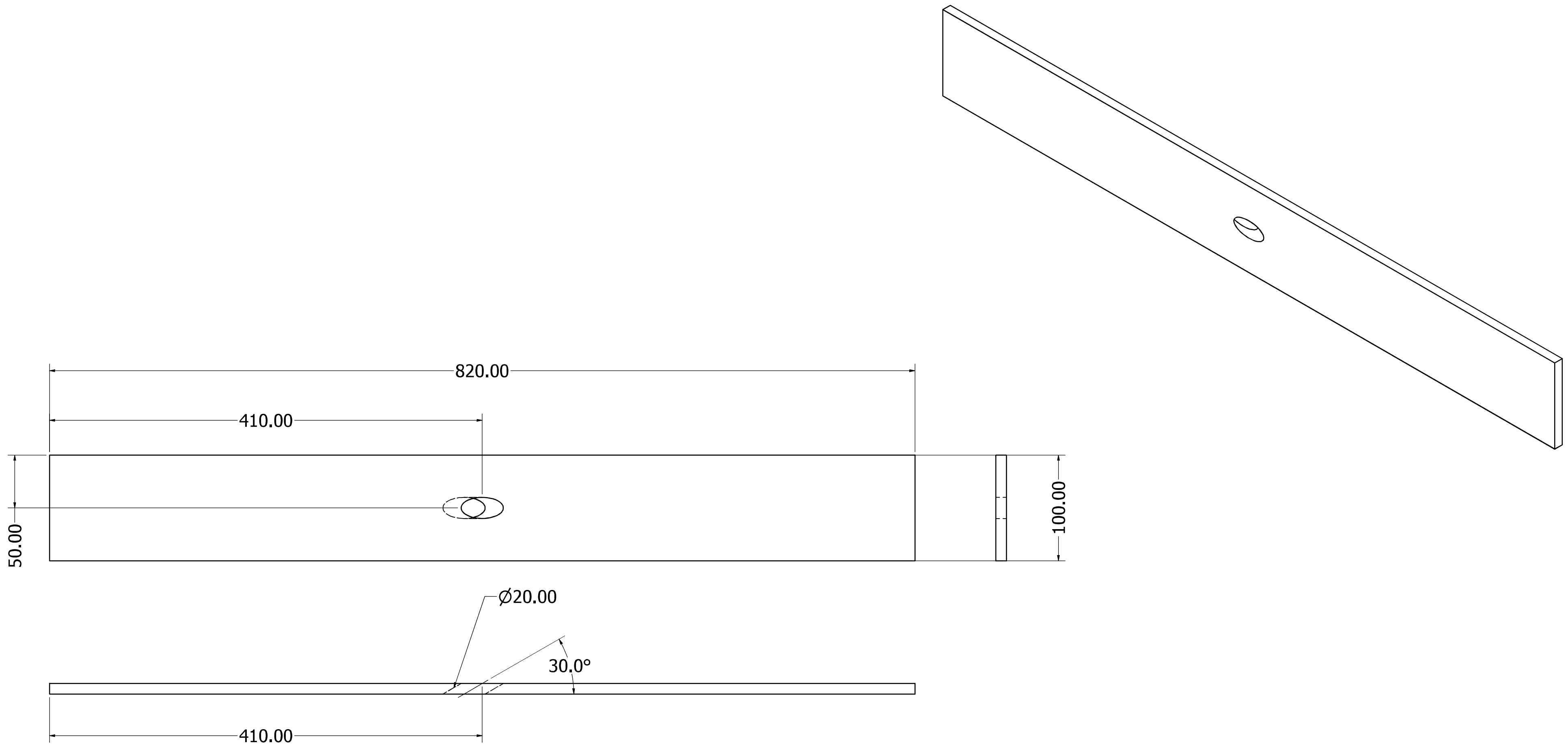

DRAWN marcg	2023/05/05			
CHECKED		TITLE		
QA				
MFG				
APPROVED		SIZE D	DWG NO Lower_Surface_Hole	REV
		SCALE 1 / 2	SHEET 1 OF 1	

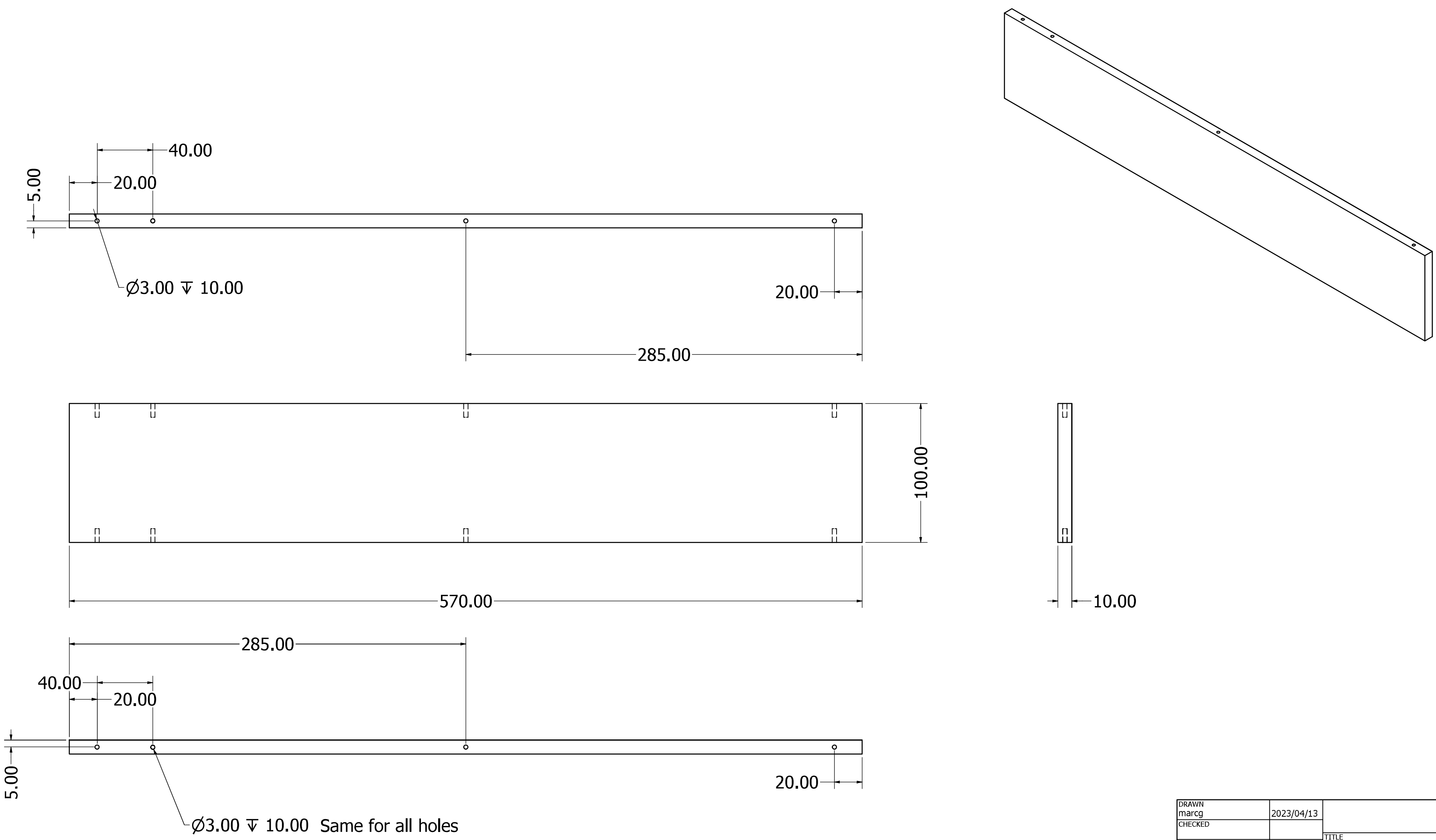

DRAWN marcg	2023/04/13	TITLE
CHECKED		
QA		
MFG		
APPROVED		

SIZE	DWG NO	REV
D	Lower_Surface_Inlet_Section	
SCALE 1 / 1.5	SHEET 1 OF 1	

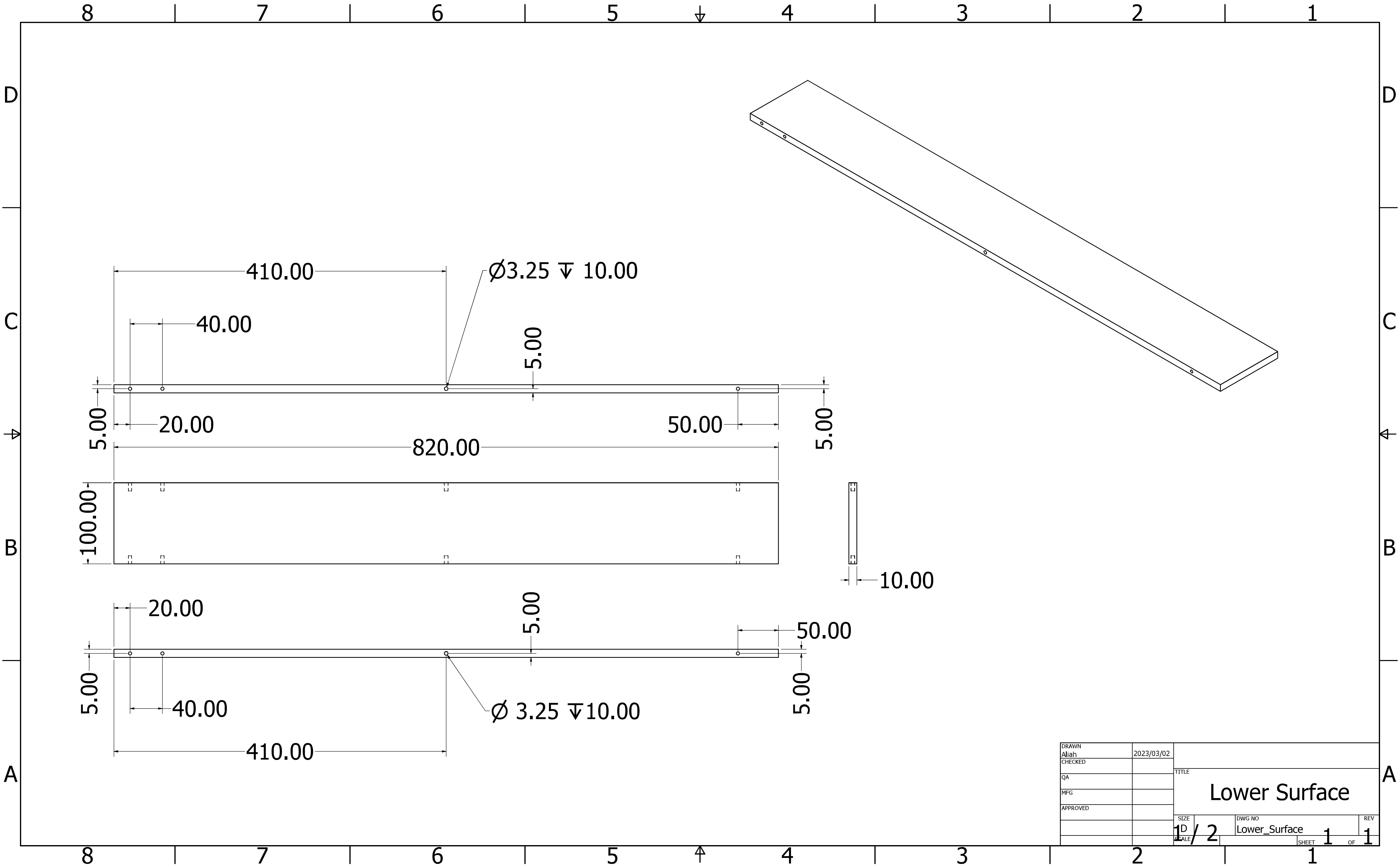

410.00
Ø3.25 ↧ 10.00
40.00
5.00
5.00
20.00
50.00
5.00
820.00
100.00
10.00
20.00
5.00
50.00
5.00
40.00
Ø 3.25 ↧10.00
5.00
410.00
DRAWN
Aliah
2023/03/02
CHECKED
QA
MFG
APPROVED
TITLE
Lower Surface
SIZE
D
SCALE
1 / 2
DWG NO
Lower_Surface
REV
1
SHEET
1
OF
1

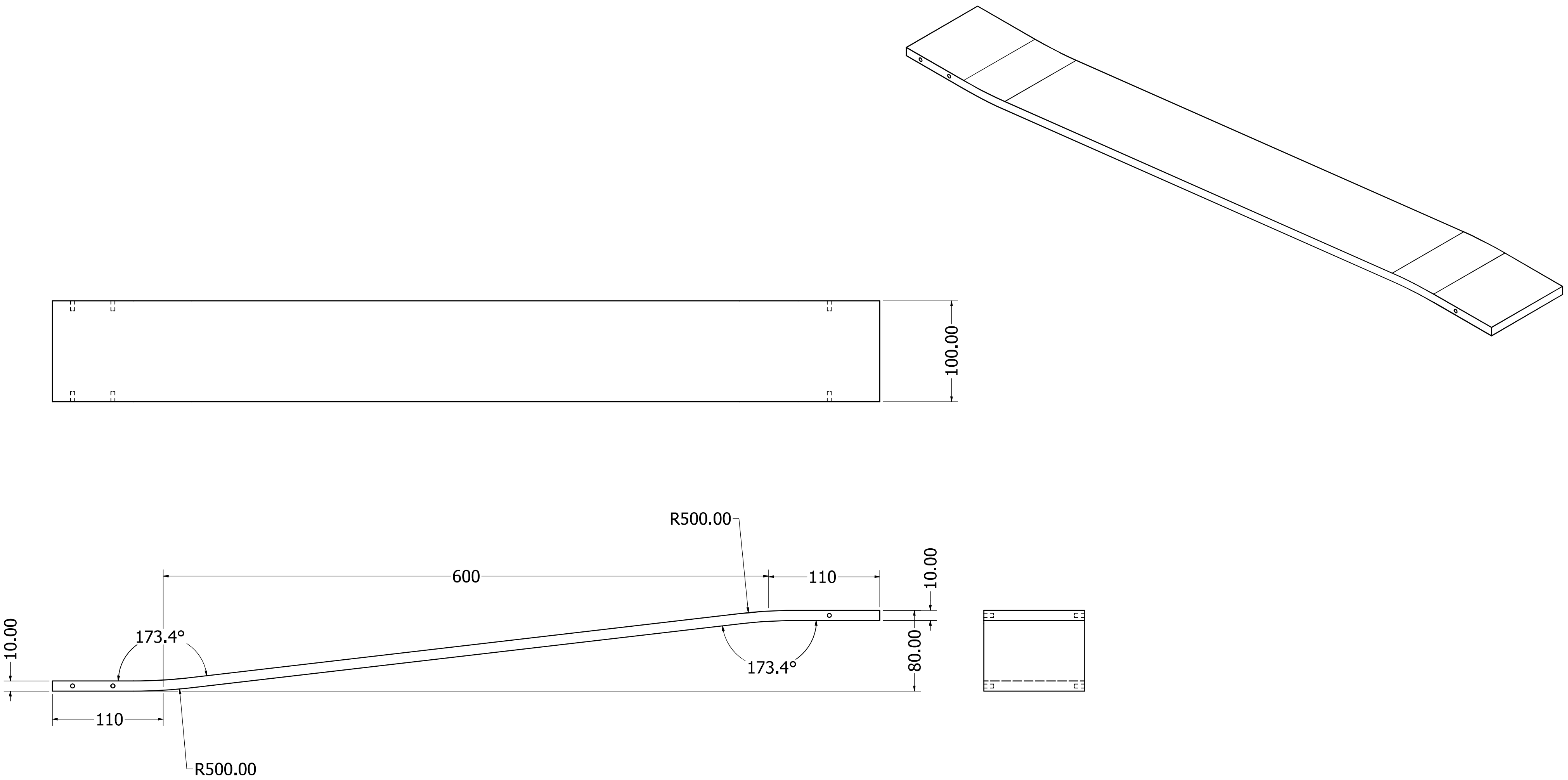

DRAWN Aliah	2023/03/16			
CHECKED		TITLE		
QA				
MFG				
APPROVED		SIZE D	DWG NO MAPG	REV
		SCALE 1 / 2	SHEET 1 OF 1	

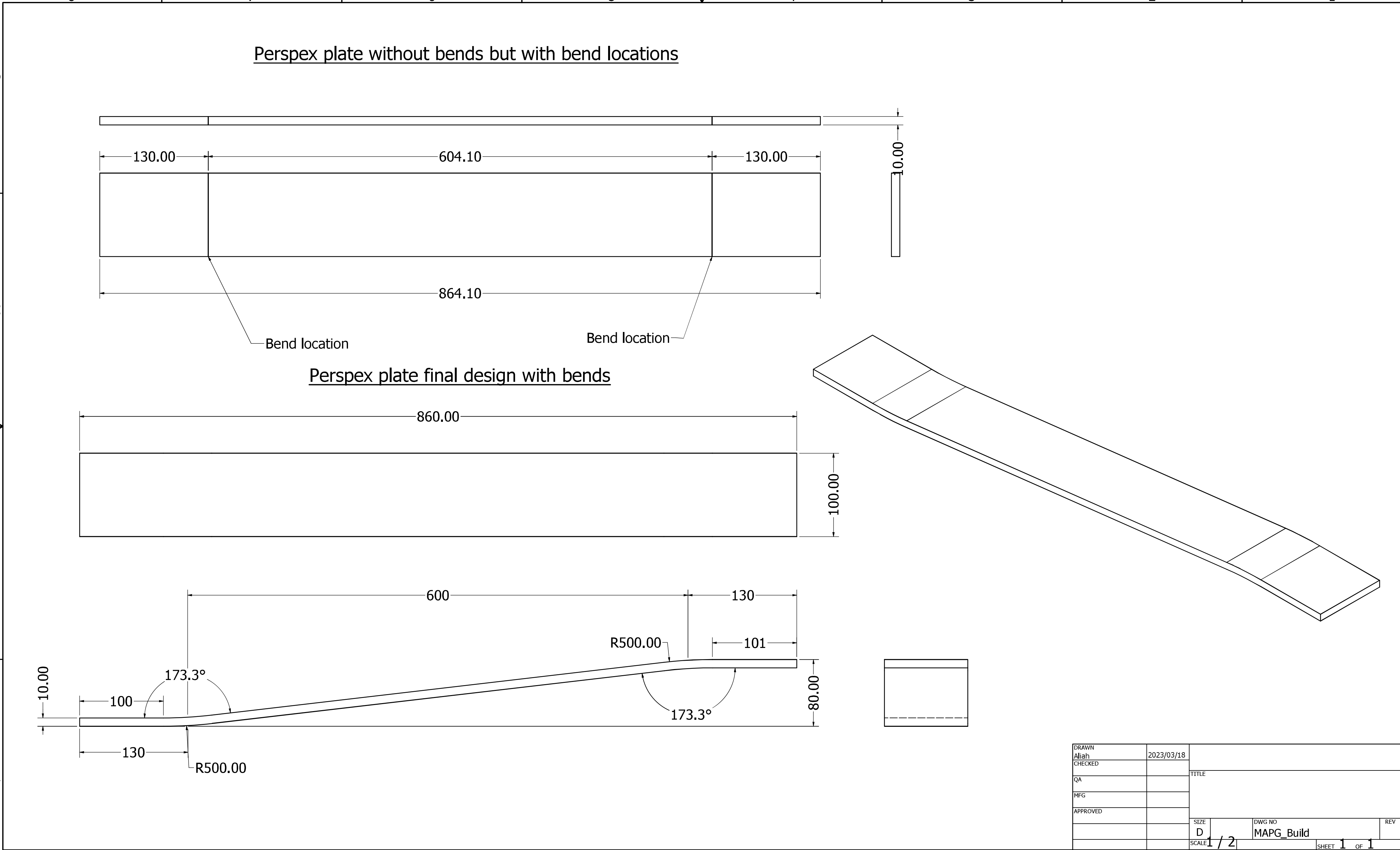
Perspex plate without bends but with bend locations
130.00
604.10
130.00
10.00
864.10
Bend location
Bend location
Perspex plate final design with bends
860.00
100.00
600
130
R500.00
101
10.00
173.3°
100
173.3°
80.00
130
R500.00
DRAWN
Aliah
2023/03/18
CHECKED
QA
MFG
APPROVED
TITLE
SIZE
D
DWG NO
MAPG_Build
REV
SCALE 1 / 2
SHEET 1 OF 1

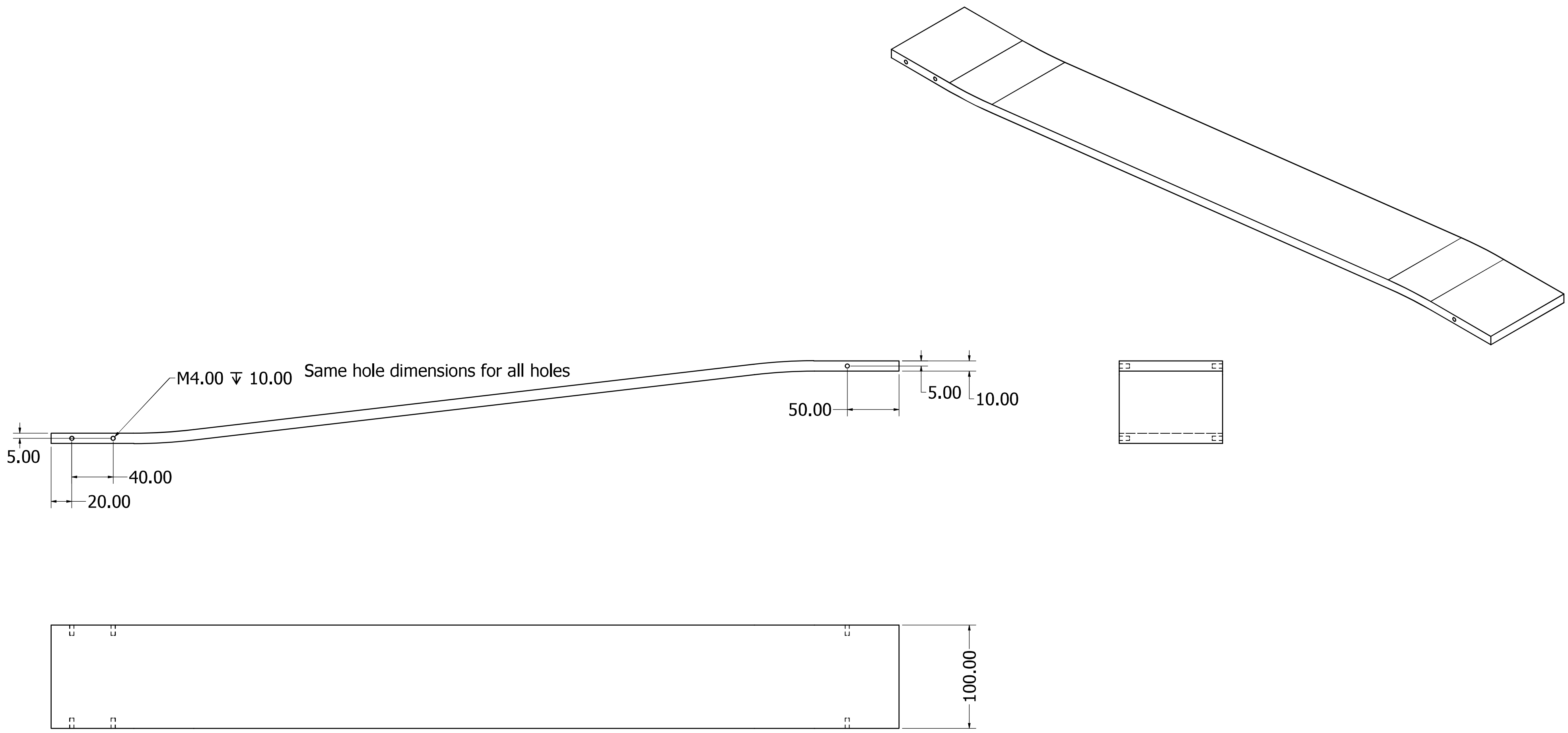

DRAWN marcg	2023/03/28	TITLE
CHECKED		
QA		
MFG		
APPROVED		SIZE D · DWG NO MAPG_Holes · REV
		SCALE 1 / 2 · SHEET 1 OF 1

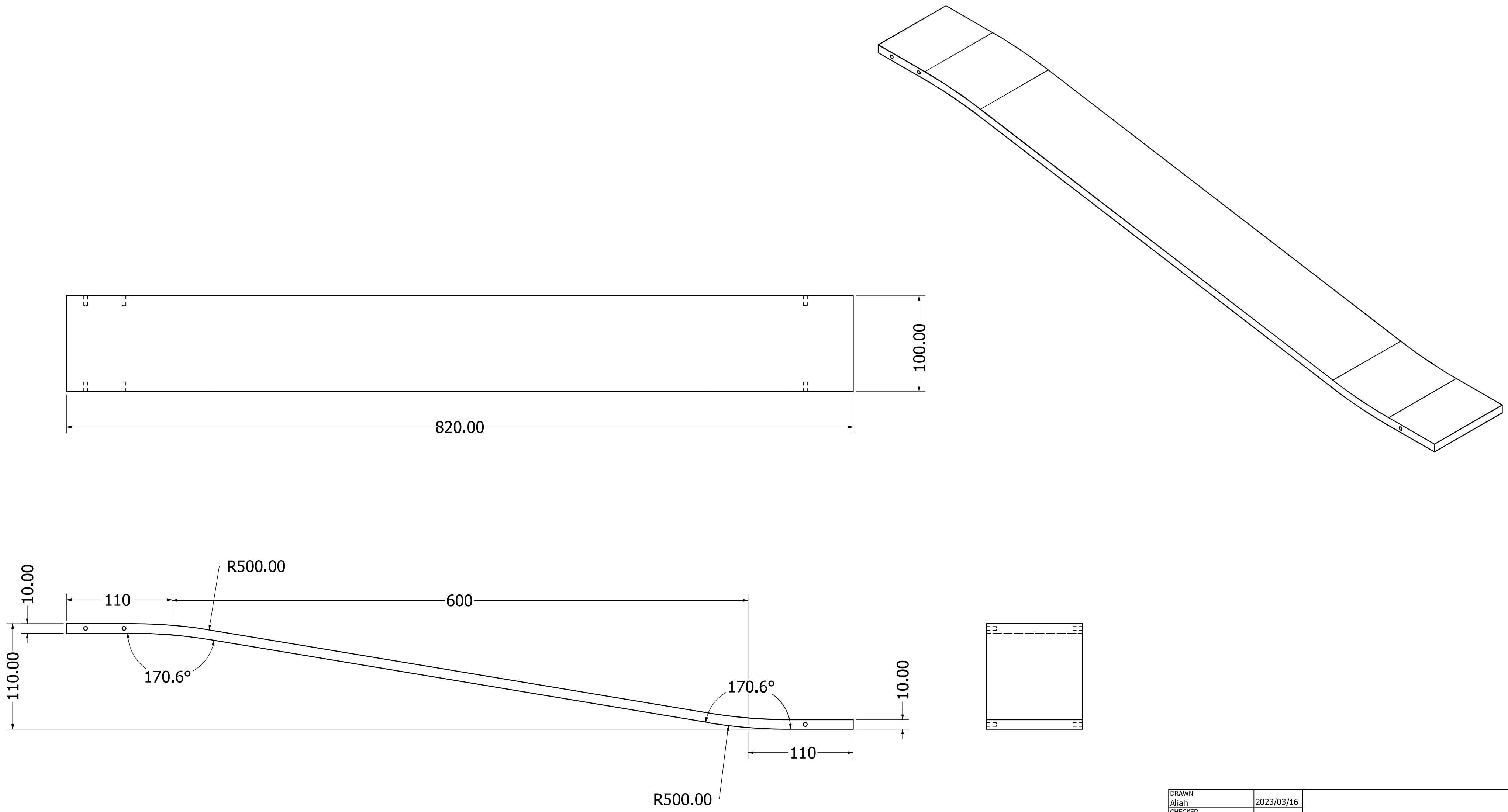

DRAWN Aliah	2023/03/16				
CHECKED		TITLE			
QA					
MFG					
APPROVED					
		SIZE D	DWG NO MFPG		REV
		SCALE 1 / 2		SHEET 1 OF 1	

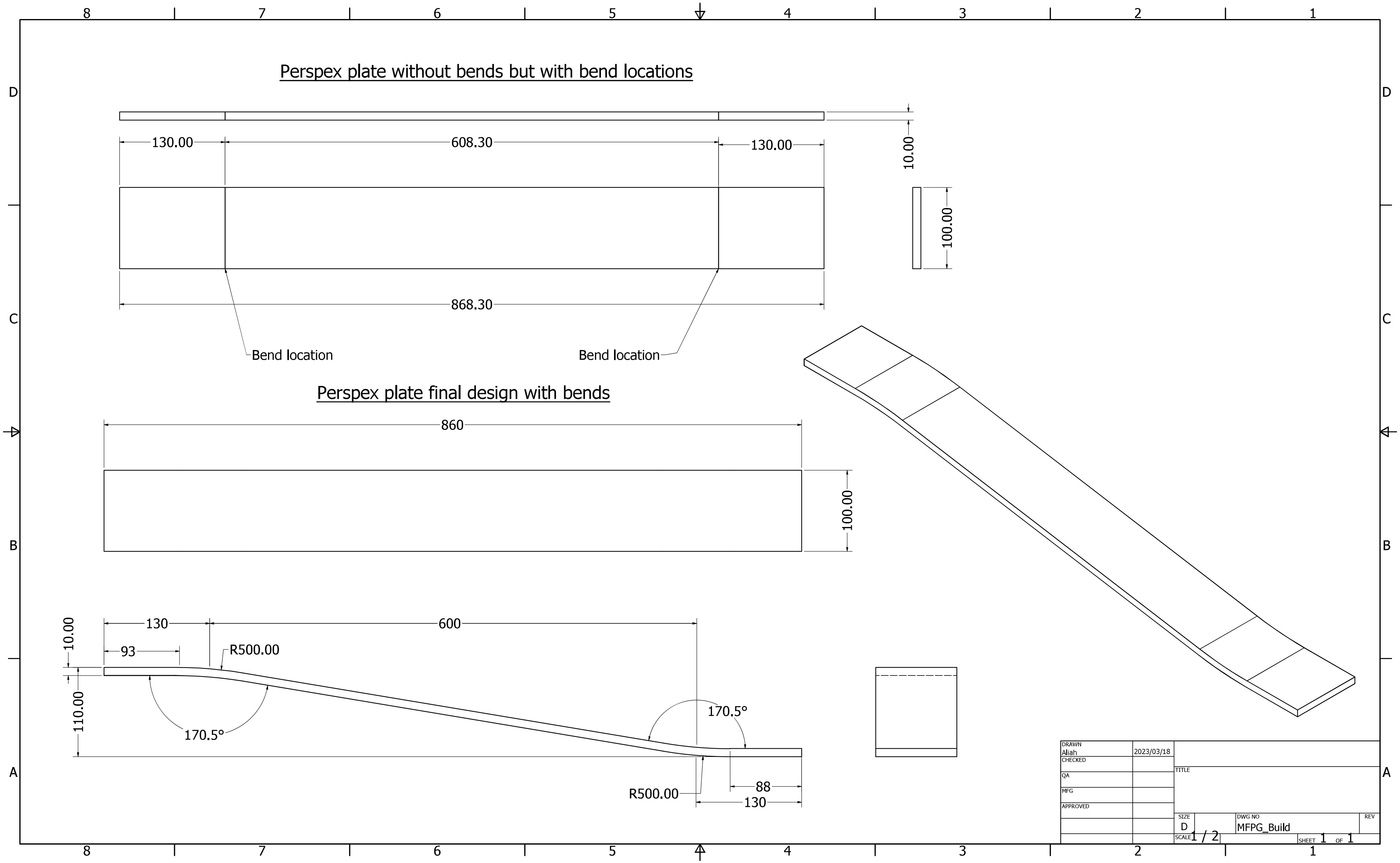
Perspex plate without bends but with bend locations
130.00
608.30
130.00
10.00
100.00
868.30
Bend location
Bend location
Perspex plate final design with bends
860
100.00
130
600
10.00
93
R500.00
110.00
170.5°
170.5°
R500.00
88
130
DRAWN
Aliah
2023/03/18
CHECKED
QA
MFG
APPROVED
TITLE
SIZE
D
SCALE 1 / 2
DWG NO
MFPG_Build
REV
SHEET 1 OF 1

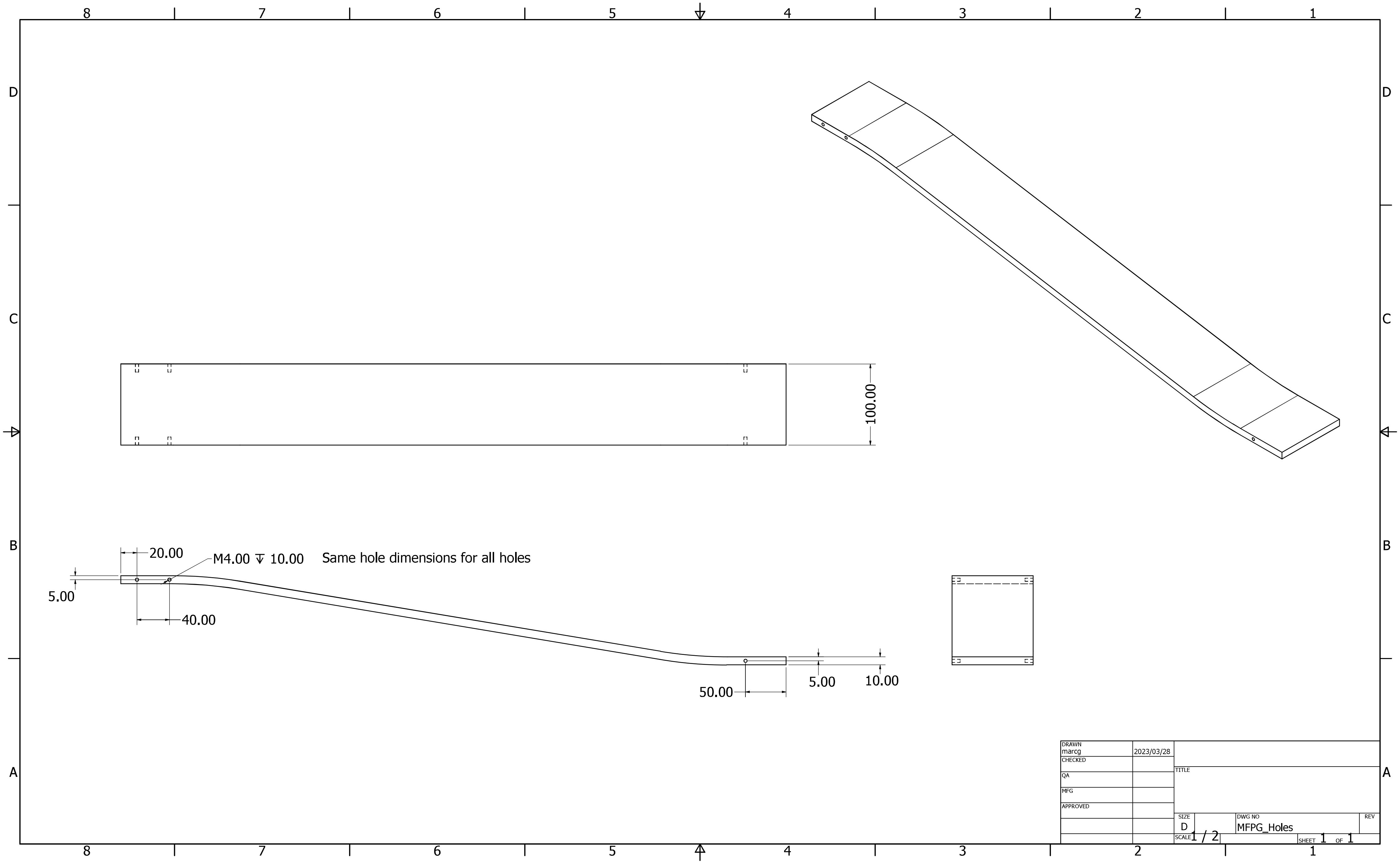
20.00
M4.00 ↧ 10.00
Same hole dimensions for all holes
5.00
40.00
100.00
50.00
5.00
10.00
DRAWN
marcg
2023/03/28
CHECKED
QA
MFG
APPROVED
TITLE
SIZE
D
DWG NO
MFPG_Holes
REV
SCALE 1 / 2
SHEET 1 OF 1

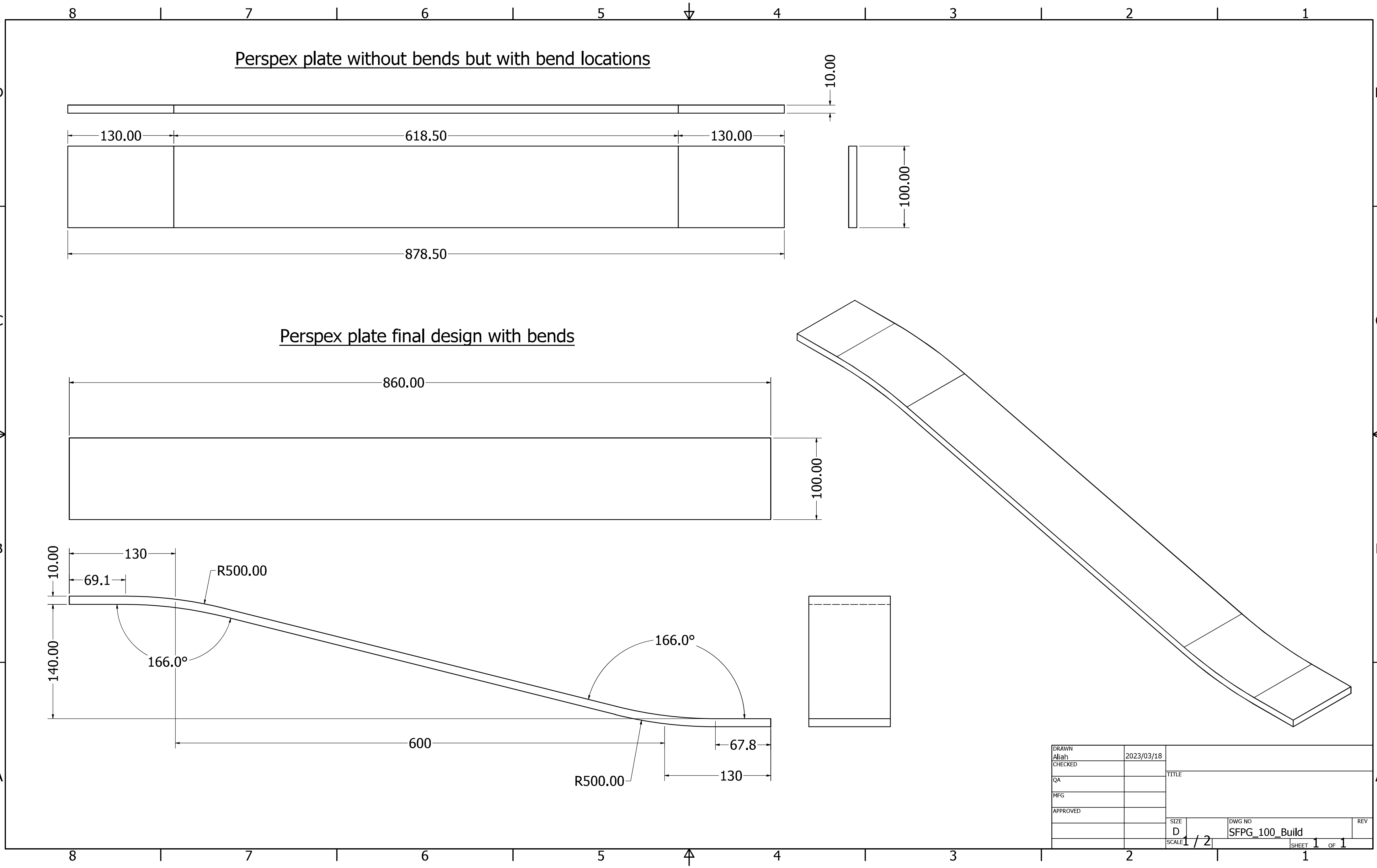
Perspex plate without bends but with bend locations
10.00
130.00
618.50
130.00
100.00
878.50
Perspex plate final design with bends
860.00
100.00
10.00
130
69.1
R500.00
140.00
166.0°
166.0°
600
R500.00
67.8
130
DRAWN
Aliah
2023/03/18
CHECKED
QA
MFG
APPROVED
TITLE
SIZE
D
DWG NO
SFPG_100_Build
REV
SCALE 1 / 2
SHEET 1 OF 1

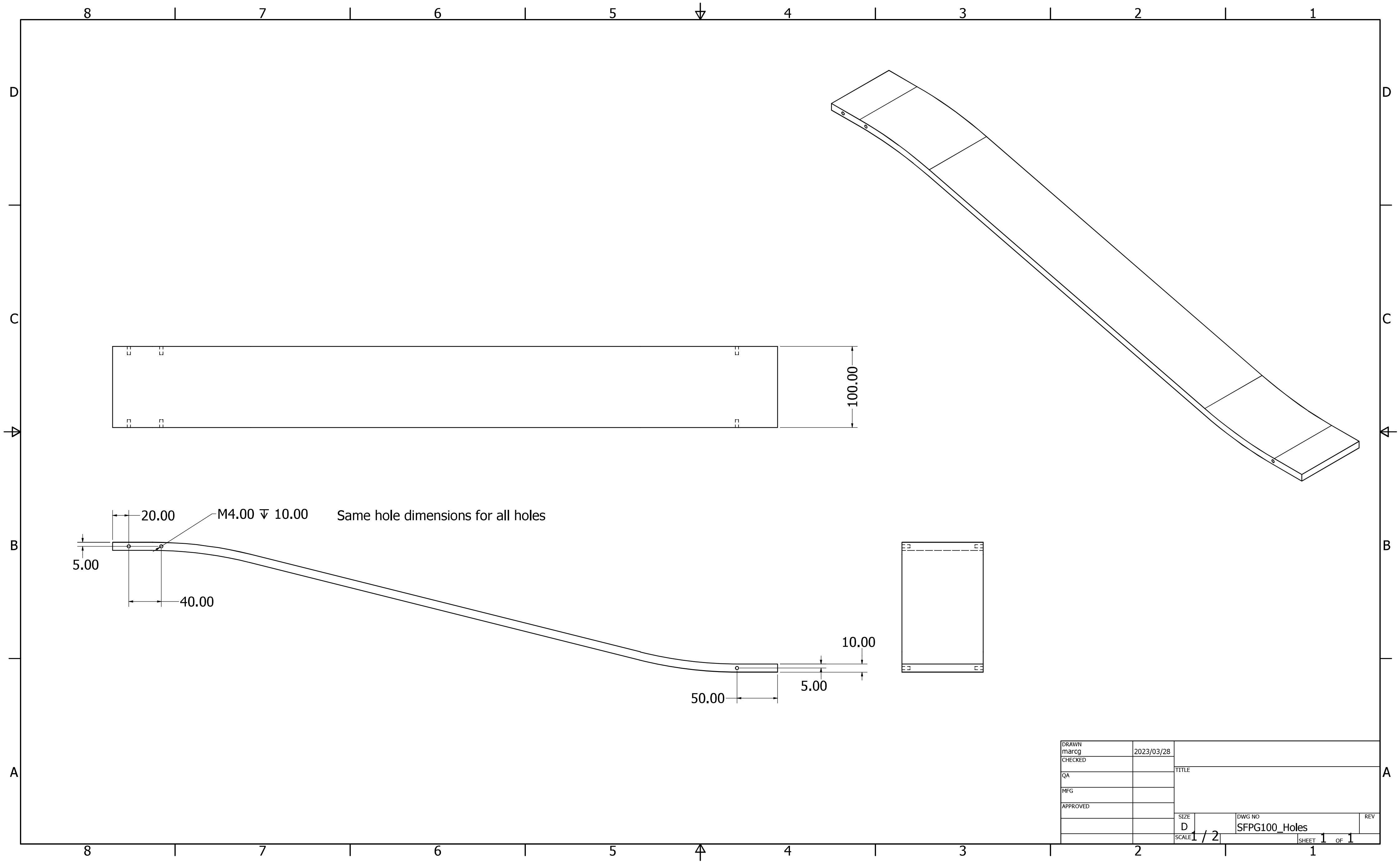

8
7
6
5
4
3
2
1
D
C
B
A
100.00
20.00
M4.00 ∇ 10.00
Same hole dimensions for all holes
5.00
40.00
10.00
5.00
50.00
DRAWN
marcg
2023/03/28
CHECKED
QA
MFG
APPROVED
TITLE
SIZE
D
DWG NO
SFPG100_Holes
REV
SCALE 1 / 2
SHEET 1 OF 1

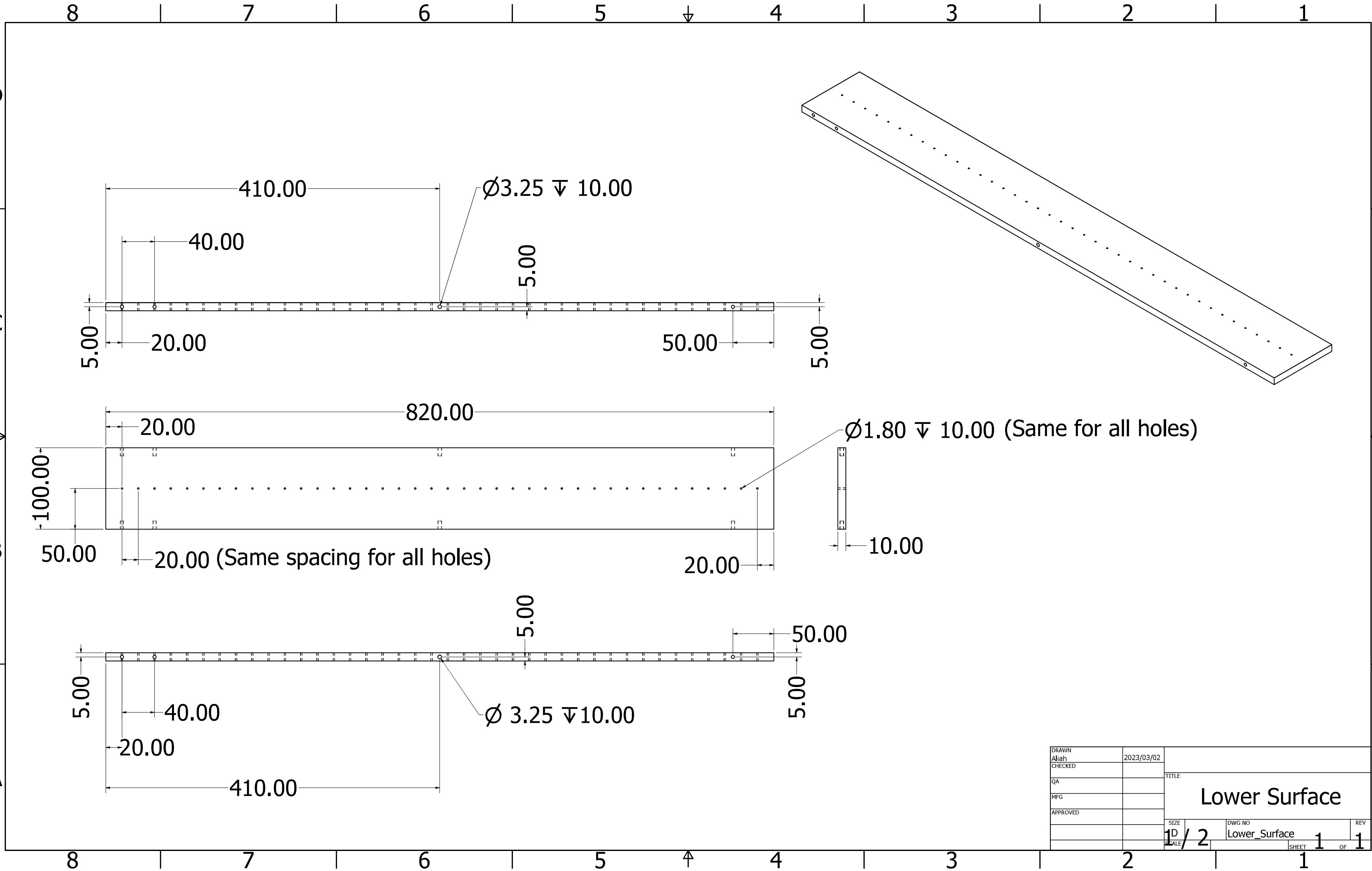
410.00
Ø3.25 ↧ 10.00
40.00
5.00
5.00
20.00
50.00
5.00
820.00
20.00
Ø1.80 ↧ 10.00 (Same for all holes)
100.00
50.00
20.00 (Same spacing for all holes)
20.00
10.00
5.00
50.00
5.00
40.00
Ø 3.25 ↧10.00
5.00
20.00
410.00
DRAWN
Aliah
2023/03/02
CHECKED
QA
MFG
APPROVED
TITLE
Lower Surface
SIZE
D
DWG NO
Lower_Surface
REV
SCALE
1 / 2
SHEET
1
OF
1

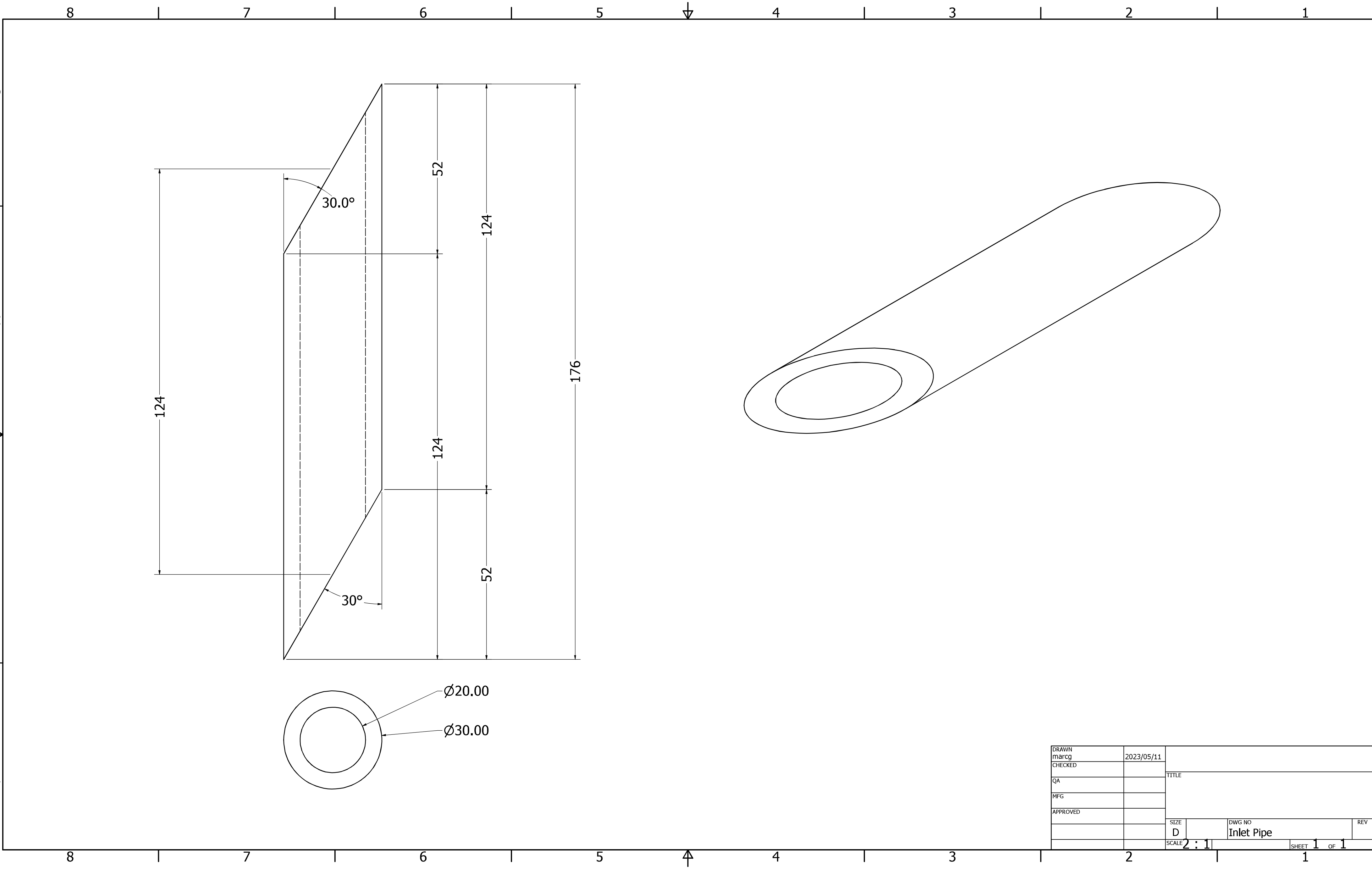
8
7
6
5
4
3
2
1
D
C
B
A
52
124
176
124
124
52
30.0°
30°
Ø20.00
Ø30.00
DRAWN
marcg
2023/05/11
CHECKED
QA
MFG
APPROVED
TITLE
SIZE
D
DWG NO
Inlet Pipe
REV
SCALE 2 : 1
SHEET 1 OF 1

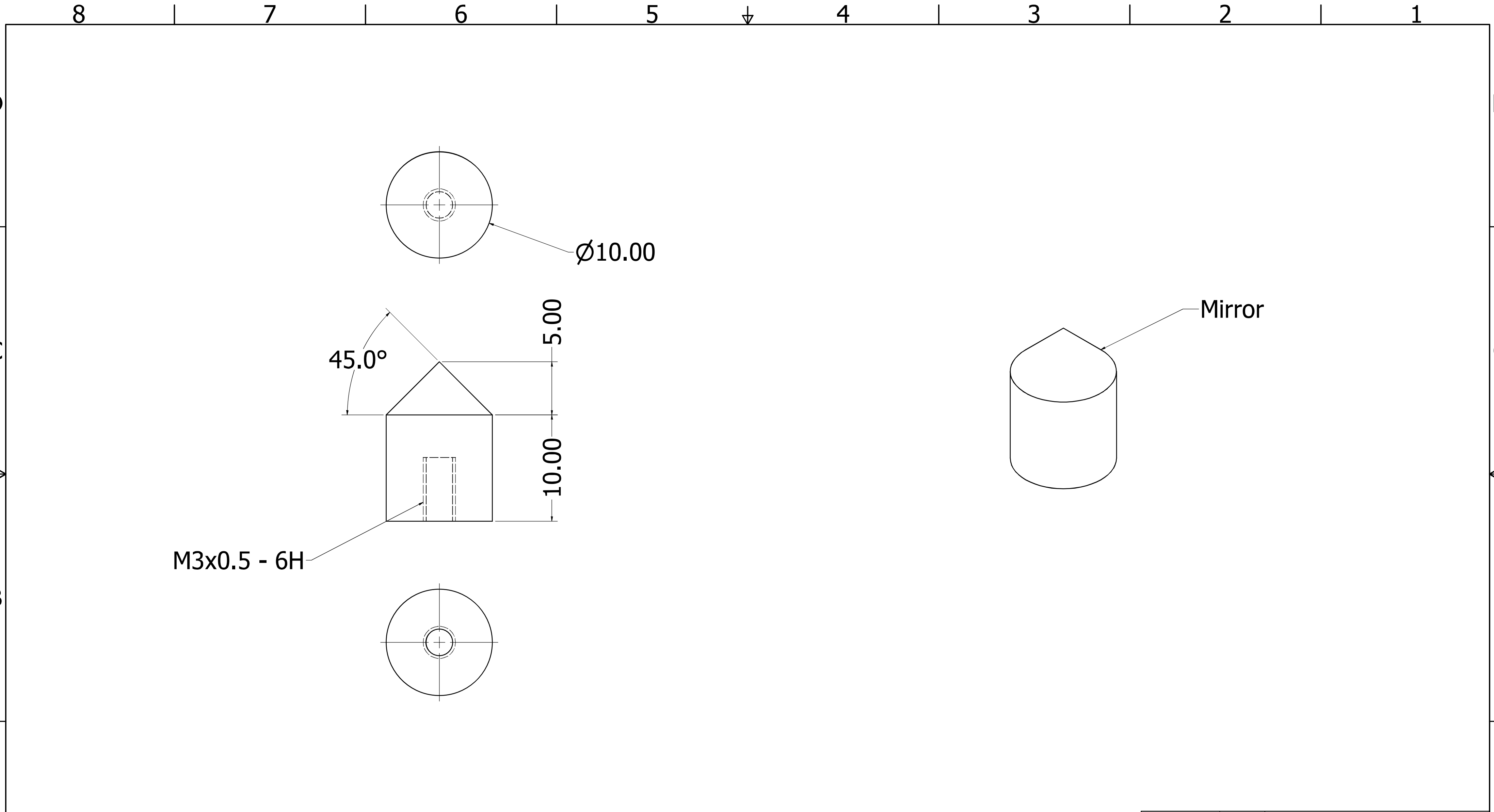

DRAWN marcg	2023/11/22	
CHECKED		TITLE
QA		
MFG		
APPROVED		
		SIZE D · DWG NO Cone Mirror With Cooling Fins · REV
		SCALE 6 : 1 · SHEET 1 OF 1

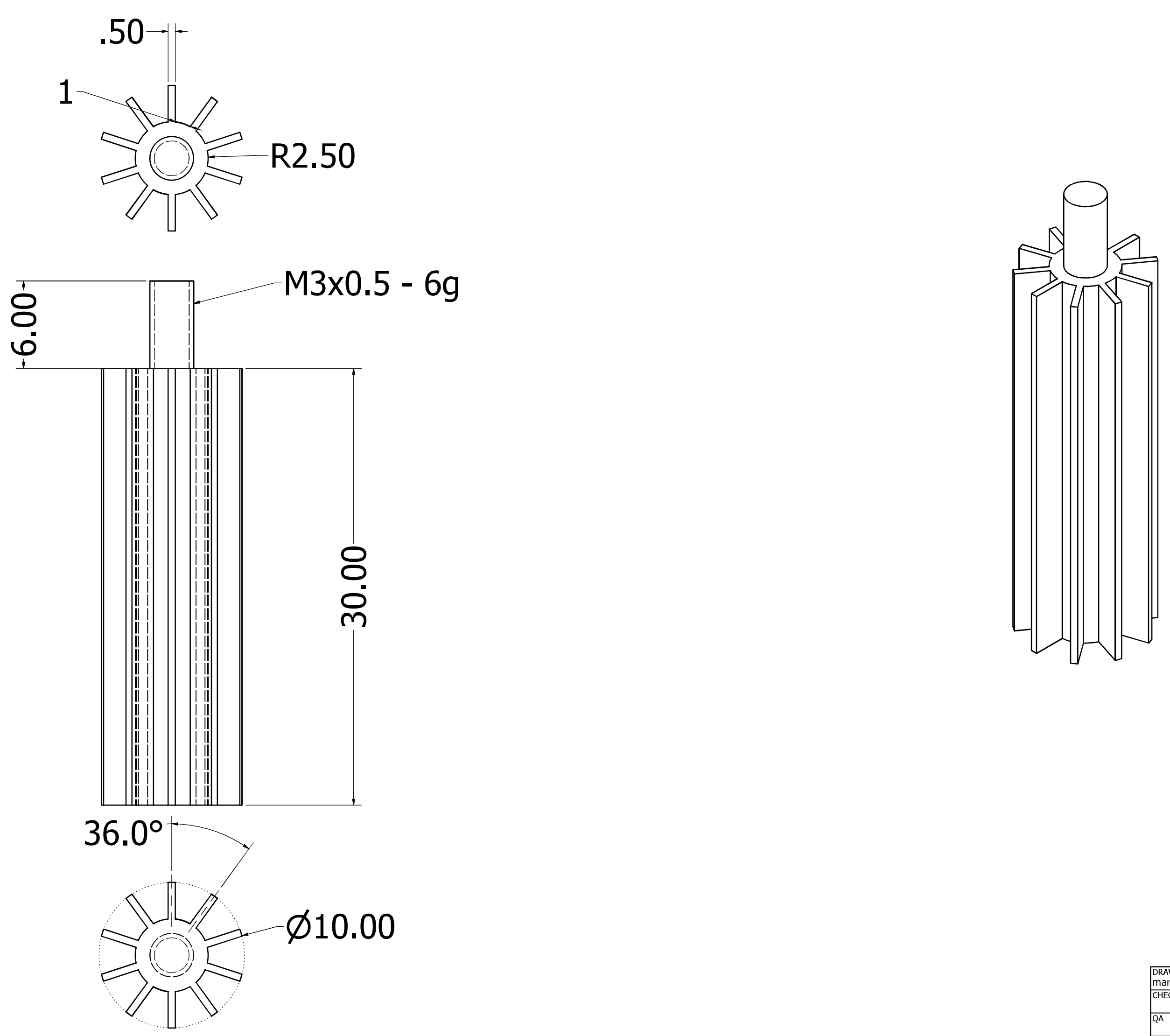

DRAWN marcg	2023/11/22	
CHECKED		TITLE
QA		
MFG		
APPROVED		
		SIZE D / DWG NO Heat Sink / REV 1
		SCALE 6 : 1 / SHEET 1 OF 1

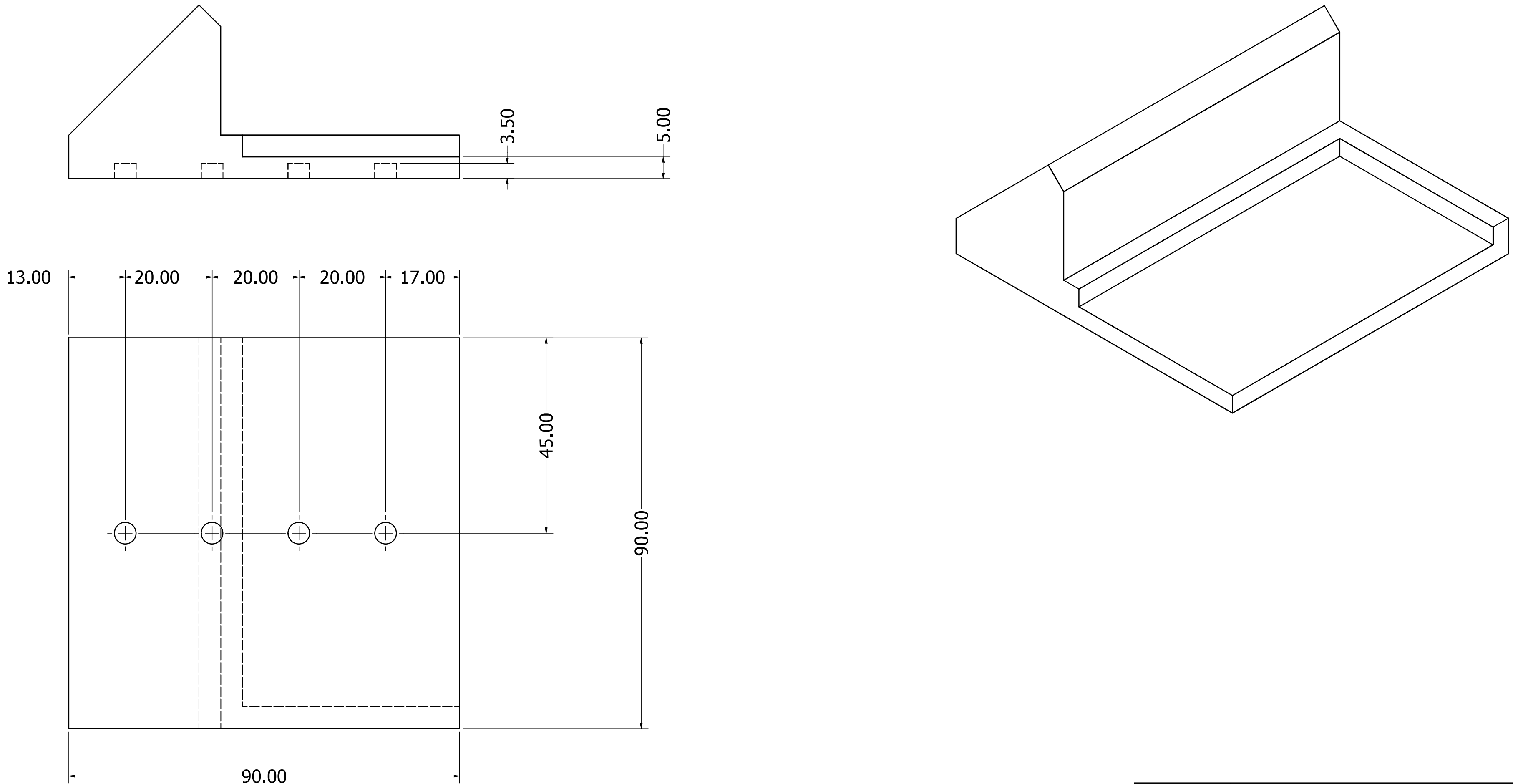

DRAWN marcg	2024/03/07			
CHECKED		TITLE		
QA				
MFG				
APPROVED		SIZE D	DWG NO 45 deg platform holder	REV
		SCALE 2 : 1		SHEET 1 OF 1

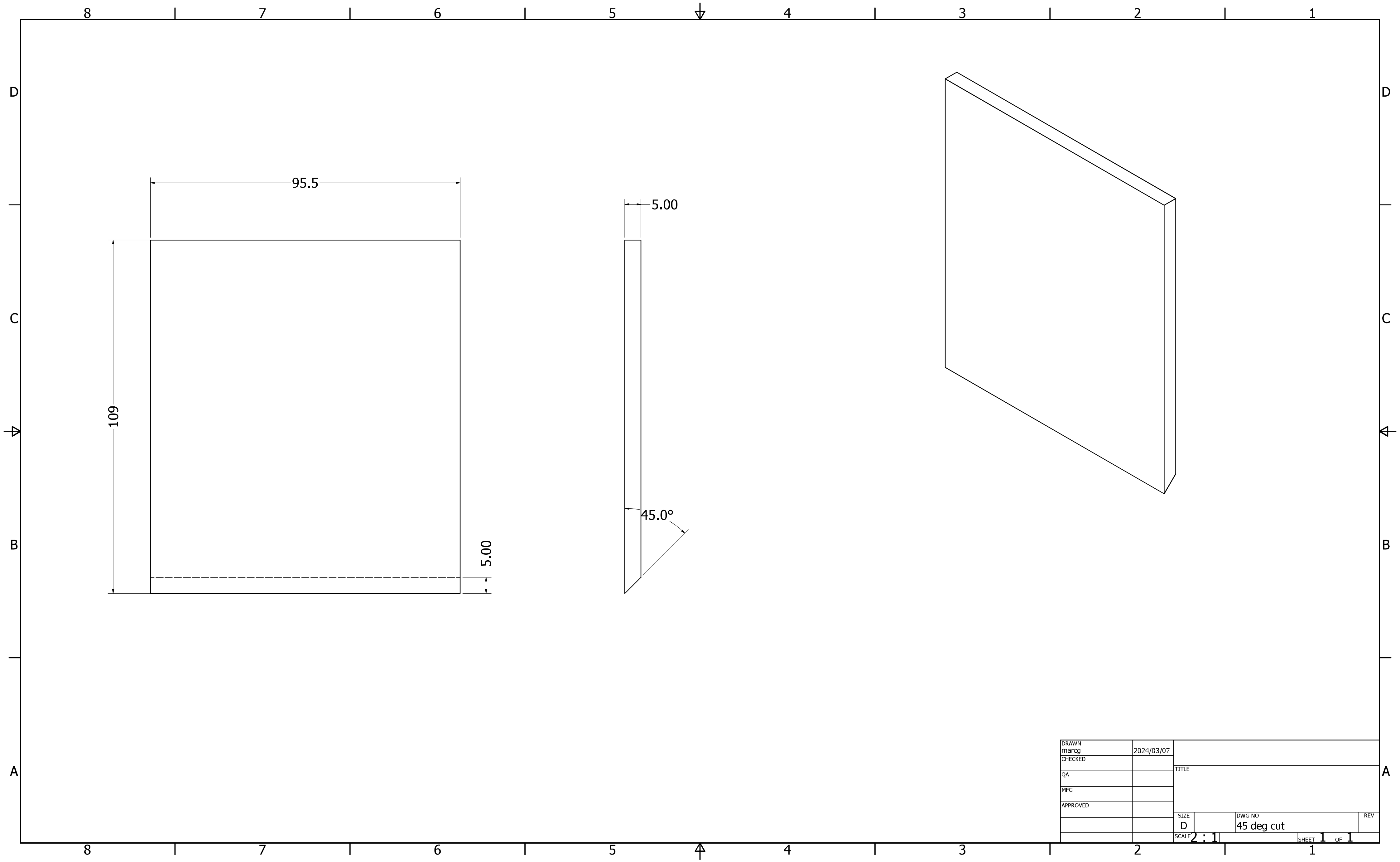

95.5
109
5.00
5.00
45.0°
DRAWN
marcg
2024/03/07
CHECKED
QA
MFG
APPROVED
TITLE
SIZE
D
DWG NO
45 deg cut
REV
SCALE 2 : 1
SHEET 1 OF 1

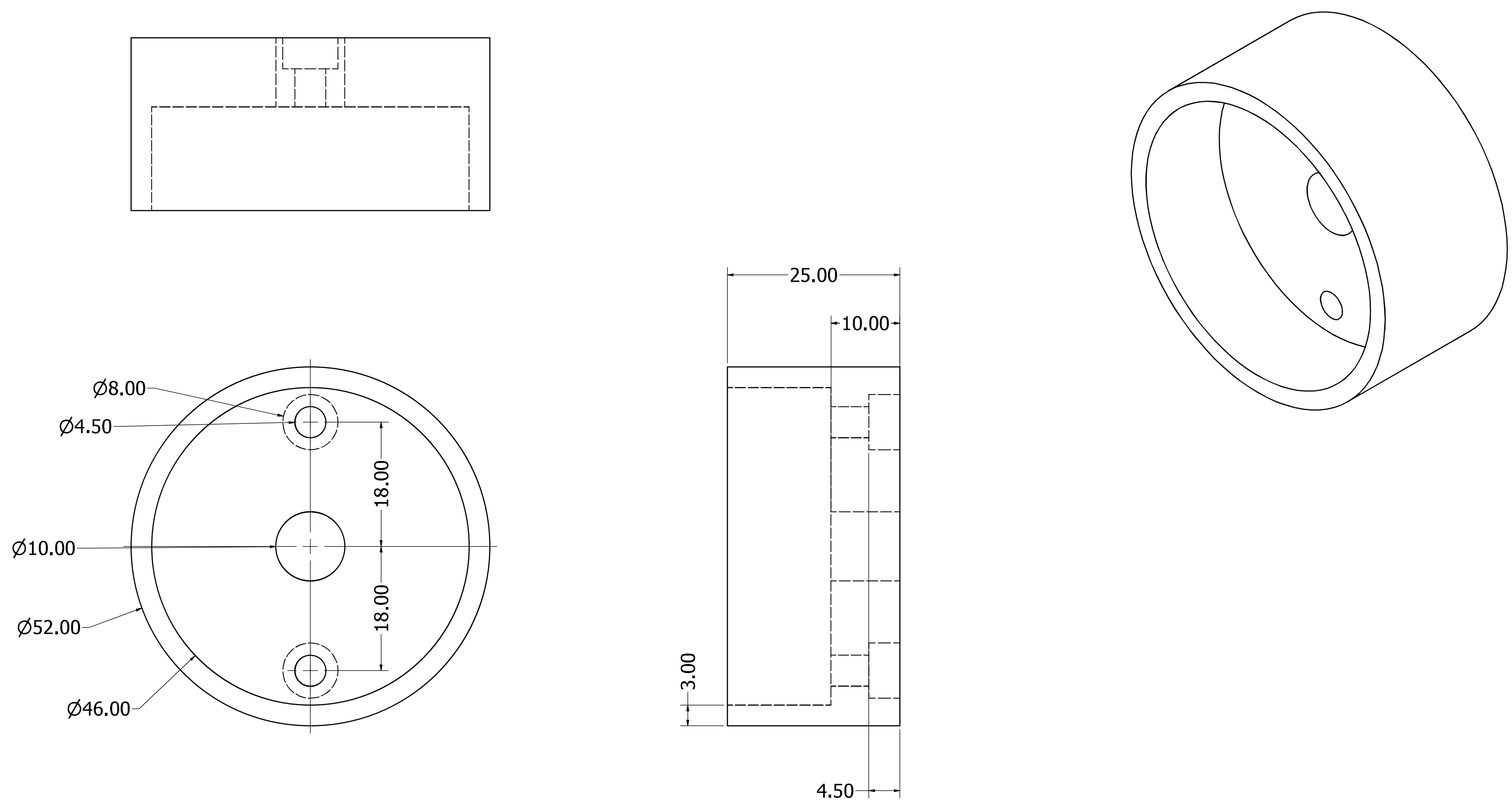

DRAWN marcg	2023/06/21				
CHECKED		TITLE			
QA					
MFG					
APPROVED		SIZE D	DWG NO Lase_Adapterr		REV
		SCALE 3 : 1		SHEET 1 OF 1	

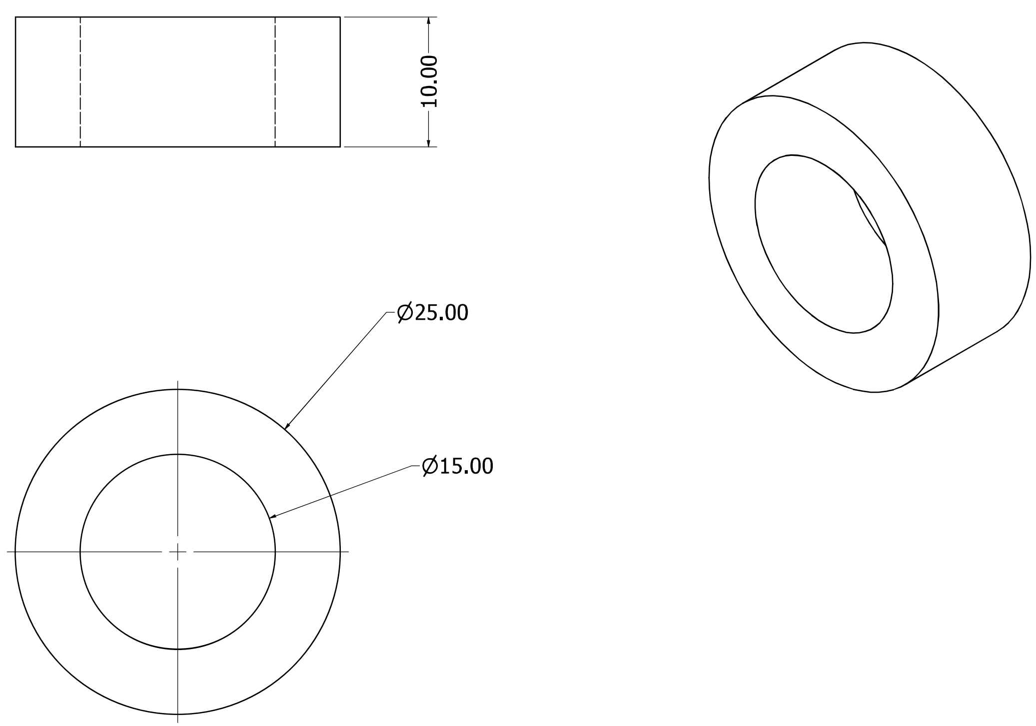

DRAWN marcg	2023/06/23	
CHECKED		TITLE
QA		
MFG		
APPROVED		SIZE D / DWG NO LaserConeBushSimple / REV
		SCALE 5 : 1 / SHEET 1 OF 1